Pontificia Universidad Católica del Perú

Escuela de Posgrado

Tesis de Maestría
Preparation and characterization of sputtered hydroxyapatite thin films

Para obtener el grado de:
Master of Science (M. Sc.)
en Ingeniería y Ciencia de los Materiales

Presentado por:	Jorge Alfonso Ugarte Díaz
Fecha y Lugar de Nacimiento:	02/09/1988 Lima, Perú

Tutor Responsable (TU Ilmenau):	Dr.-Ing. Rolf Grieseler
	apl. Prof. Dr.-Ing. habil. Lothar Spieß
Profesor Responsable (TU Ilmenau):	Univ.-Prof. Dr. rer. nat. habil. Peter Schaaf
Profesor Responsable (PUCP):	Prof. Dr. Francisco Rumiche Zapata

Fecha y Lugar: 30/09/2017, Lima

Preface

This thesis was performed in the framework of a double degree program with the Technische Universität Ilmenau (TUI) and the Pontificia Universidad Católica del Perú (PUCP). The research for this thesis has been carried out in the Laboratory at Zentrum für Mikro- und Nanotechnologien (TUI), in cooperation with the Laboratory of Material Science at the Department of Physics (PUCP).

A mis padres, por ser el pilar fundamental en todo lo que soy

y a mi hermano, por sus valiosos consejos de vida.

Contents

Abstract

In this work, hydroxyapatite (HAp) thin films were fabricated using two different sputtering techniques: Radio frequency magnetron sputtering and ion beam sputtering. In the first case, the films were grown on Ti-6Al-4V substrates using a high-purity commercial HAp target, obtaining a thickness ~200 nm. For the second method, the film were grown on pure titanium substrates using a self-produced HAp target. This target was fabricated with powders (Ca/P = 1.628, sintered and crushed). Here, the thickness of the fabricated film was ~300 nm. The sintering tests for the target fabrication were carried out using two different heating regimens at a maximum temperature of 1200 °C (holding time of 2h and 4h) using various additives. As additives, water (H_2O), polyvinyl alcohol (PVA) and polyethylene glycol (PEG) were used to improve the mechanical strength of the green discs. The as-deposited films were amorphous in both cases. Therefore, the films were annealed to increase the crystallinity. Annealing was performed in air for 2h at temperatures: 400, 600 and 800 °C for RF-magnetron sputter samples; 600 and 800 °C for ion beam sputter samples. The result of the films shows in both cases that the crystallinity of HAp was improved only for the annealed samples fabricated with ion beam sputtering at 800 °C. In both cases energy dispersive X-ray spectroscopy measurements show a decrease in Ca/P ratio with increasing the temperature. Hardness results revealed an increase in this with the increase in temperature possibly due to the formation of titanium oxide. The roughness for the fabricated films with the RF-magnetron sputtering increases till an annealing temperature of 600 °C and then decreases till 800 °C, while the roughness for the fabricated films with ion beam sputtering is higher in the as-deposited samples and then this is reduced by increasing the annealing temperature.

Kurzfassung

In dieser Arbeit, wurden Hydroxyapatit (HAp) Schichten unter Verwendung von zwei verschiedenen Sputtertechniken hergestellt: Radiofrequenz Magnetronsputtern und Ionenstrahlsputtern. Im erste Fall wurden die Schichten auf Ti-6Al-4V-Substraten unter Verwendung eines hochreinen kommerziellen HAp-Targets gewachsen, wobei eine Dicke von 200 nm erhalten wurde. Für die zweite Herstellungsmethode wurden die Schichten auf reinen Titansubstraten unter Verwendung eines selbst hergestellten HAp-Targets abgeschieden. Dieses wurde aus einem Pulver (Ca/P = 1,628, gesintert und zerkleinert) hergestellt. Die Schichtdicke war hier, nach dem Ionenstrahlsputtern 300 nm. Die Sinterversuche für die Targetherstellung wurde unter Verwendung von zwei verschiedenen Heizregimen bei einer maximalen Temperatur von 1200 °C (Haltezeit von 2h und 4h) unter Verwendung von verschiedenen Additiven durchgeführt. Als Additive kamen Wasser (H_2O), Polyvinylalkohol (PVA) und Polyethylenglykol (PEG) zum Einsatz, um dis mechanische Festigkeit der Grünkörper zu verbessern. Die erhaltenen Schichten war in beiden Fällen nach dem Sputtern amorph. Daher wurden auch die Schichten in einem Nachbehandlungsschritt erneut getempert, um die Kristallinität zu erhöhen. Das Tempern wurde in Luftatmosphäre für 2 Stunden bei verschiedenen Temperaturen durchgeführt: 400, 600 und 800 °C für RF-Magnetron-Sputterproben; 600 und 800 °C für Ionenstrahlsputternproben. Das Ergebnis für die Schichten zeigt in beiden Fällen, dass die Kristallinität von HAp nur für die mit Ionenstrahlsputtern hergestellten getemperten Proben bei 800 ºC verbessert wurde. In beiden Fällen zeigen die energiedispersiven Röntgenspektroskopie-Messungen eine Verringerung des Ca/P-Verhältnisses mit steigender Temperatur. Die Messung der Härte ergab eine Zunahme dieser mit dem Anstieg der Temperatur möglicherweise aufgrund der Bildung von Titanoxid. Die Rauheit für die mit dem RF-Magnetron-Sputtern hergestellten Schichten steigt bis 600 °C an und sinkt dann bis 800 °C, während die Rauheit für die mit Ionenstrahlsputtern hergestellten Schichten in den abgeschiedenen Proben höher ist und dann mit steigender Tempertemperatur abnimmt.

Resumen

En este trabajo se fabricaron películas delgadas de hidroxiapatita (HAp) utilizando dos técnicas diferentes: Pulverización con radiofrecuencia y magnetrón y pulverización por haz de iones. En el primer caso, las películas se fabricaron sobre sustratos de Ti-6Al-4V usando un blanco de HAp comercial de alta pureza, obteniéndose un espesor de ~200 nm. Para el segundo caso, las películas se fabricaron sobre sustratos de titanio puro usando un blanco de HAp fabricado con polvos (Ca/P = 1,628). En este caso, el espesor de la película fue ~300 nm. La fabricación del blanco se llevó a cabo usando dos regímenes de calentamiento a una temperatura máxima de 1200 °C (a 2h y 4h) usando diversos aditivos: Agua (H_2O), alcohol polivinílico (PVA) y polietilenglicol (PEG), para mejorar la resistencia mecánica de los discos. Las películas delgadas obtenidas resultaron amorfas. Por lo tanto, se realizó un recocido para aumentar la cristalinidad. El recocido se realizó en aire por 2h: 400, 600 y 800 °C para muestras de pulverización con radiofrecuencia y magnetrón; 600 y 800 °C para muestras de pulverización por haz de iones. La cristalinidad de HAp solo mejoró en las muestras fabricadas por pulverización por haz de iones, recocidas a 800 °C. En ambos casos, las mediciones con espectrometría de rayos x muestran una disminución en la relación Ca/P con el aumento de la temperatura. La dureza aumenta con la temperatura de recocido, debido a la formación de cristal de óxido de titanio. La rugosidad de las películas fabricadas con pulverización con radiofrecuencia y magnetrón aumenta hasta una temperatura de recocido de 600 °C y luego disminuye hasta 800 °C, mientras que la rugosidad de las películas fabricadas con pulverización por haz de iones es mayor en las muestras depositadas y luego esto se reduce al aumentar la temperatura de recocido.

1. Introduction

Calcium phosphate based ceramics (CPCs) have proved to be attractive materials for biological applications [1–5]. There are several families of CPCs which are identified by their Ca/P ratio, crystalline structure and degree of solubility in water [4, 5]. Among these bioceramics, particular attention has been given to hydroxyapatite (HAp), due to its bioactive nature which arises from its chemical similarity with the inorganic phase of natural bone [6–9].

HAp is commonly used in the form of dense sintered parts or powder [10]. Some works have been devoted to the sintering mechanisms of HAp parts [11, 12]. The understanding of sintering is of prime importance as this allows the identification of the influencing parameters and therefore the control of the grain growth and the microstructural design of the ceramics [13]. Other works refer to the preparation of coatings over different substrates (polymer or metal) and to their physico-chemical and biological characterizations as medical implants [14–16].

The bone is a highly hierarchical organic-inorganic material composed of hardened collagen fibers with HAp nanocrystals (thin plate-shaped, approximately 50 nm long, 25 nm wide, and 2 nm thick) [3]. Its basic composition is HAp (~60–70 wt%), collagen (~20–30 wt%) and water (up to 10 wt%) [6, 17]. Being HAp the largest constituent, it can be considered as best candidate to coat the implants.

In this context, in recent years, great efforts have been made to develop new technologies regarding the production of coatings, to improve the clinical response of implants in the bone regeneration processes.

Plasma spray deposition technique has been widely used for fabricating HAp on metallic implants due to its rapid deposition rate and relative low cost [18]. However, as this technique requires high temperature, films with high roughness [19], alterations in HAp structure [20, 21] and low adhesion between the coatings and metallic substrates [19] were reported.

Due to the know the problems arising from the plasma-spraying process, numerous experimental deposition process have been investigated, including thermal spraying [18–24], sputter coating [25–29], pulsed laser ablation [30, 31], sol–gel [32–34] and electrodeposition [35–39]. Among them, sputtering techniques have proven to be very attractive due to the uniform coating thickness produced on flat substrates, dense coating, Ca/P ratios well conformed to the theoretical HAp stoichiometry (1.667) and good stimulation of the cell growth *in vitro* [40].

The main objective of the present work is to obtain HAp thin films on titanium substrates with sputtering techniques. Titanium provides the required mechanical strength to simulate bone tissue in load applications (maximum load, flexure, and fatigue strength). HAp provides a bioactive interface between bone and implant, which stimulates the growth of the tissue. Both materials together provide the mechanical and biological properties that allow a firm connection with the bone. In order to reach this objective, sputter targets of HAp were fabricated using a pressureless sintering process. These targets were fabricated with the assistance of Yesenia Sauñi, who used the targets for her thesis "Synthesis of hydroxyapatite thin films on PMMA 3D printed substrates".

Two different sputter techniques were used: Ion beam sputtering (IBS) and radio frequency (RF) magnetron sputtering, analyzing the physical and chemical properties of the HAp films deposited by both techniques.

To characterize the powder, the sintered targets and the obtained films, a structural analysis with X-ray diffraction was carried out in order to determine the predominant crystalline phases. Scanning electron microscopy was used to characterize the morphology of the produced targets and films. In addition, the composition was measured with energy dispersive X-ray spectroscopy. Roughness measurements were performed in order to interpret the roughness effect on implant/bone adhesion and hardness measurements were determined in order to evaluate the resistance of the HAp films during load application.

2. Theoretical Background

Nowadays, CPCs with clinical applications constitute an interesting field of research and development in the production of biomedical implants, exhibiting excellent biocompatibility with the living body when replacing hard tissue.

CPCs have a varied Ca/P ratio, chemical composition and water solubility as shown in **Table 1**. Understanding the solubility allows to know the behavior of the CPCs in the body environment. In addition, CPCs can degrade and transform into even more soluble phases, due to their sensibility to high temperatures [6, 41].

Table 1: Existing CPCs showing their Ca/P ratio, chemical composition and water solubility [41].

Ca/P	Compound	Formula	Solubility at 25 °C (g/L)
0.5	Monocalcium phosphate monohydrate (MCPM)	$Ca(H_2PO_4)_2 \cdot H_2O$	~18
0.5	Monocalcium phosphate anhydrous (MCPA)	$Ca(H_2PO_4)_2$	~17
1.0	Dicalcium phosphate dihydrate (DCPD); brushite	$CaHPO_4 \cdot 2H_2O$	~0.088
1.0	Dicalcium phosphate anhydrous (DCPA); monetite	$CaHPO_4$	~0.048
1.33	Octacalcium phosphate (OCP)	$Ca_8(HPO_4)_2(PO_4)_4 \cdot 5H_2O$	~0.0081
1.5	α-Tricalcium phosphate (α-TCP)	$\alpha\text{-}Ca_3(PO_4)_2$	~0.0025
1.5	β-Tricalcium phosphate (β-TCP)	$\beta\text{-}Ca_3(PO_4)_2$	~0.0005
1.2–2.2	Amorphous calcium phosphates (ACP)	$Ca_xH_y(PO_4)_z \cdot nH_2O$ $n = 3 - 4.5; 15 - 20\%\ H_2O$	------
1.5–1.67	Calcium-deficient hydroxyapatite (CDHA)	$Ca_{10-x}(HPO_4)_x(PO_4)_{6-x}(OH)_{2-x}$ $(0 < x < 1)$	~0.0094
1.67	Hydroxyapatite (HAp)	$Ca_{10}(PO_4)_6(OH)_2$	~0.0003
1.67	Fluorapatite (FAp)	$Ca_{10}(PO_4)_6F_2$	~0.0002
1.67	Oxyapatite (OAp)	$Ca_{10}(PO_4)_6O$	~0.087
2.0	Tetracalcium phosphate (TTCP), hilgenstockite	$Ca_4(PO_4)_2O$	~0.0007

The atomic arrangement of CPCs is based on a network of orthophosphate (PO_4) groups, which gives stability to the entire structure [6, 42]. A phase diagram $CaO–P_2O_5$ at temperatures between 200 and 2200 °C is shown in **Figure 1**. The majority of CPCs are slightly soluble in water; however, all of them are easily soluble in acids but insoluble in alkaline solutions [6, 42].

Given these properties, the CPCs are used for various applications: For example, brushite (DCPD) and monetite (DCPA) are commonly used in the preparation of cements in biological applications due to the high dissolution in the physiological environment, being very useful for repairing of the bone and stimulating its growth [43–45]. On the other hand, tricalcium phosphate (TCP) and hydroxyapatite (HAp) used as coatings due to their low dissolution rate and good chemical stability, which allow the cells growth and promote the osseointegration when interacting with human hard tissue [22–39, 46–48].
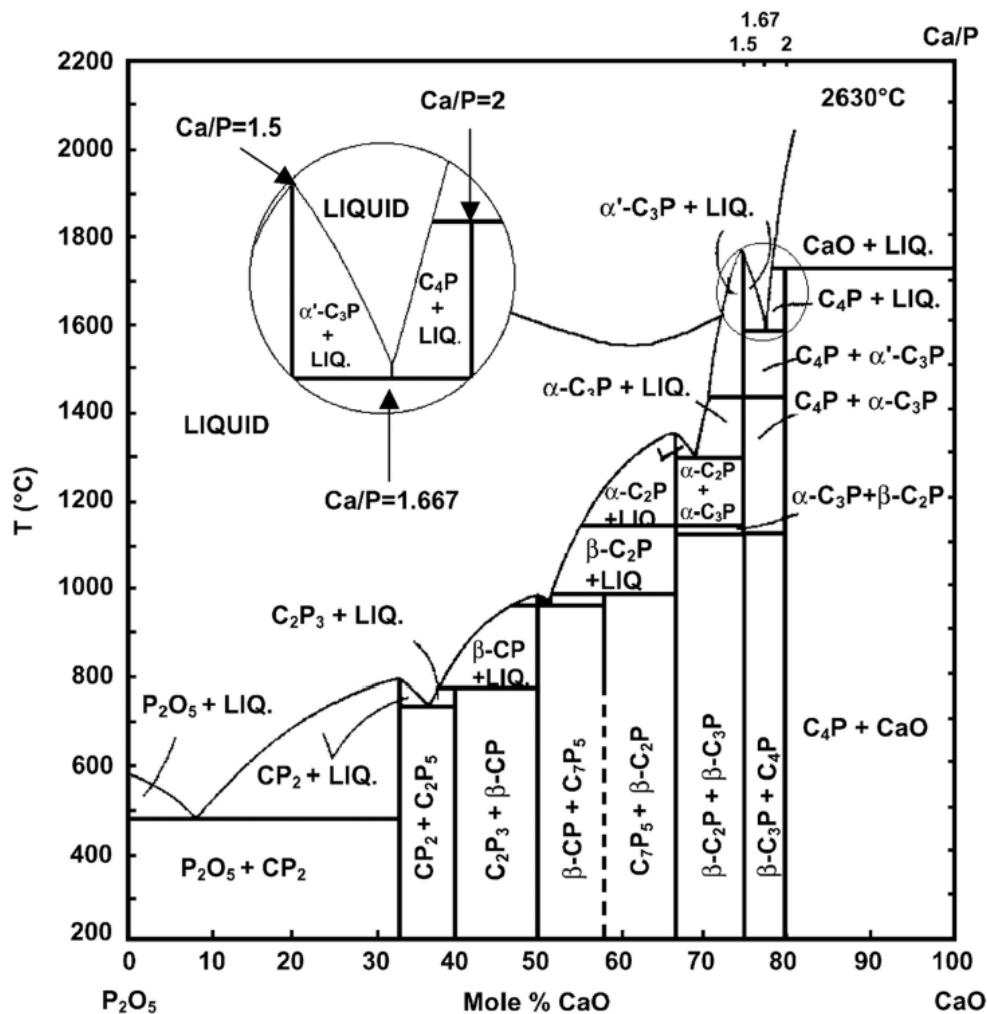
Figure 1: Phase diagram of the system $CaO–P_2O_5$ (C = CaO, P = P_2O_5). Here: C_2P_3 means $2CaO.3P_2O_5$; the same way for other abbreviations [6].

2.1 Hydroxyapatite

Hydroxyapatite (HAp), with the chemical formula $Ca_{10}(PO_4)_6(OH)_2$ and a Ca/P molar ratio of 1.67 [49–51], is widely accepted as a biocompatible material similar to the mineral component of the bones and teeth. Nevertheless, this is only an oversimplification of the bone mineral [52]. Actually, it is considered as a complex substance, also doped with cations (Na, K, Mg, Zn, Fe, etc.) and carbonate ions [52, 53]. The generic chemical formula suggested by Hench, L.L. [10] for this crystalline phase is:

$$Ca_{8.3}(PO_4)_{4.3}(HPO_4, CO_3)_{1.7}(OH, CO_3)_{0.3}$$
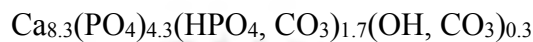
HAp crystallizes in two systems: the hexagonal system ($a_0 = 0.943$ nm, $c_0 = 0.689$ nm at 300 °K, space group $P6_3/m$) and the monoclinic system ($a_0 = 0.984$ nm, $b_0 = 2a_0$, $c_0 = 0.688$ nm at 300 °K, space group $P2_1/b$) [54–57]. It was experimentally proven that the first is less stable but it is the most representative phase in bones and teeth [8]. The hexagonal HAp is usually formed by precipitation from supersaturated solutions at 25–100 °C, while the monoclinic HAp is primarily formed by heating the hexagonal form at 850 °C in air and subsequent cooling to room temperature [9]. The crystalline structure of both systems are shown in **Figure 2**.
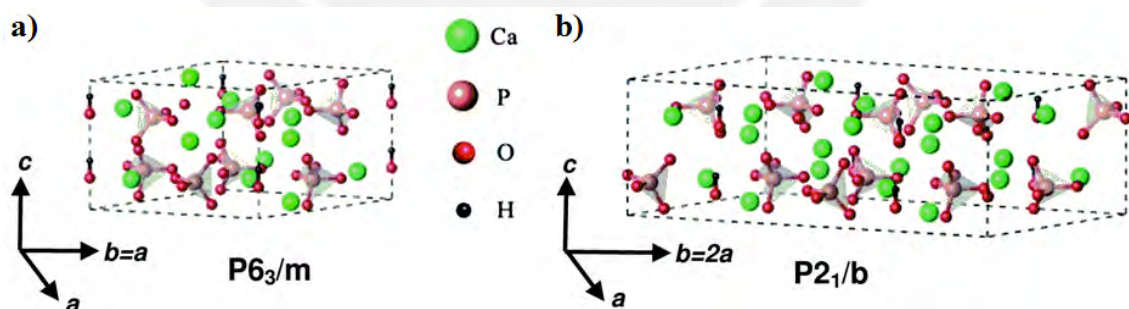
Figure 2: Crystalline structure of HAp: a) Hexagonal ($P6_3/m$) and b) monoclinic P21/b [58].

According to Champion, E. [59], the PO_4 tetrahedra are hold together by Ca ions interspersed among them. In the $P6_3/m$ form, the unit cells of HAp are arranged along the c-axis. Therefore, a preferred orientation along the c-axis and a needle-like morphology is common. Regarding the structural aspect, the difference between the monoclinic and hexagonal HAp is the orientations of hydroxyl groups (OH^-) [59]. In monoclinic HAp, all of OHs in a given column are oriented in the same direction, and the direction reverses in

the next column, while in hexagonal HAp the adjacent OHs point in opposite directions [59].

It is generally considered that $Ca_9(PO_4)_6$ clusters, the so-called Posner's clusters, are the growth unit of HAp crystals [60–62], since the atomic configurations of Ca^{2+} and $(PO_4)^{3-}$ is very close to the HAp structure. A representation of the Posner's cluster is shown in **Figure 3**. This arrangement is analogous to that existing in several other crystalline phosphates, such as apatites and β-Tricalcium phosphate (β-TCP) [63].

Another relative specie is the calcium deficient hydroxyapatite (CDHA), with a Ca/P ratio between 1.67 and 1.5 [1, 6, 42]. It is referred to a hydroxyapatite structure with cation vacancies (Ca^{2+}) and anion (OH^-) vacancies. The sites occupied solely by phosphate anions in stoichiometric hydroxyapatite, are occupied by phosphate or hydrogen phosphate (HPO_4^{2-}) anions [1, 6, 42].
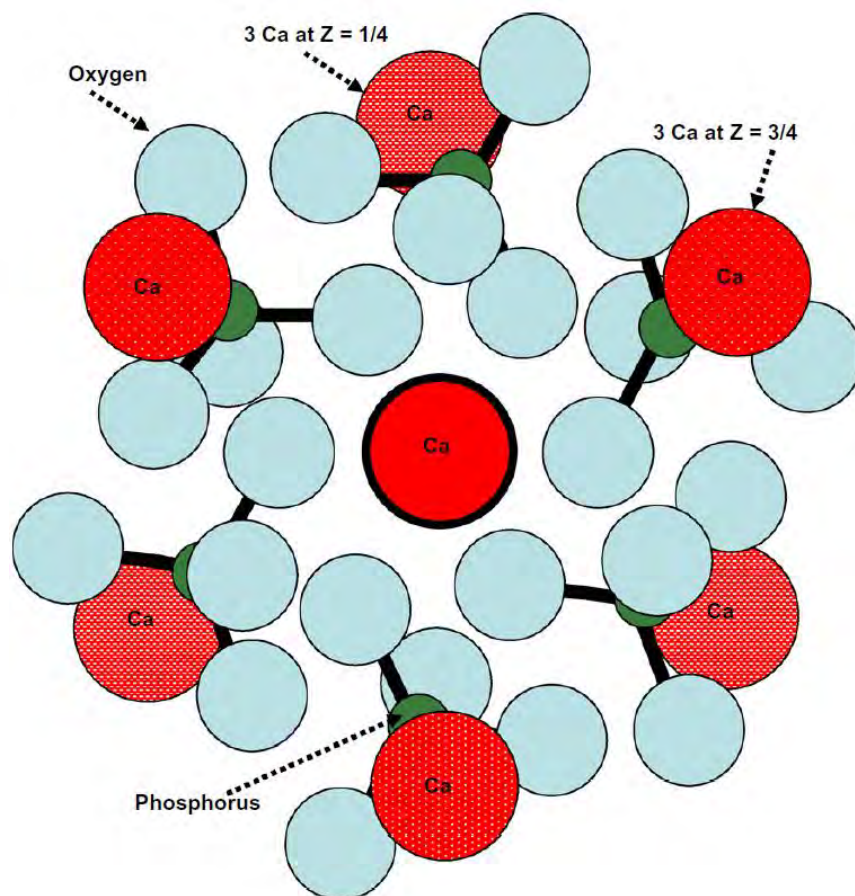
Figure 3: Representation of Posner's cluster [63], which is also the core of the actual structural model of amorphous calcium phosphate [62].

2.2 Biomedical applications

The bones have the ability of self-repairing due to a process of continuous remodeling, formation and resorption (Wolff's Law) [64, 65], but this ability is limited as it depends on how severe the suffered damage is. Severe damage from accidents and degenerative diseases (e.g. osteoporosis) affects millions of persons every year, who need a long-term solution to improve their life quality.

Implants are used in case of a severe injury, where the replacement of a damaged bone is required. The implants can be made of certain metals, ceramics, polymers or composites. This group of materials used to replace a part or a function of the human body are called biomaterials [66].

A biomaterial is defined by Williams, D.F [67] as a substance that has been engineered to take a form which, alone or as part of a complex system, is used to direct the course of any therapeutic or diagnostic procedure, in human or veterinary medicine, by the control of interactions with components of living systems.

In addition, as referred by Sykaras, N. [68], biomaterials can be classified based on the type of biologic response they show when implanted and the long-term interaction that they develops with the host tissue. Three major types of biodynamic activity have been reported: *(1)* biotolerant, *(2)* bioinert, and *(3)* bioactive [68]. The different levels of biocompatibility emphasize the fact that no material is completely accepted by the biologic environment [68].

Metals for implants have been selected based on a number of factors: their biomechanical properties; previous experience with processing, treating, machining, and finishing; and suitability for common sterilization procedures [68]. Among them, it is an undeniable fact that titanium and its alloys have gained a significant place among the most used metal as bone and dental implants due to the excellent balance between their mechanical, physicochemical and biofunctional properties [69].

This material has an excellent corrosion resistance as the surface of the titanium is rapidly oxidized inside of the body, generating a finely and thermodynamically stable oxide layers [70]. These oxides are characterized by being impermeable (therefore protective) and inert, which gives them excellent biocompatibility [70].

Mechanically, titanium based implants have properties closer to those for bones, compared to those for implants made of stainless steels and cobalt alloys. Its Young modulus is 110 GPa [71], compared to 200 GPa [72] and 220 GPa [73] for stainless steels and cobalt alloys, respectively. Being the maximum elastic modulus of the bone 13.8 GPa [6], it is clear that the titanium is more compatible with the natural tissue.

The ASTM Designation: F67 – 13 classifies titanium into four grades, defined by the content of further elements, as shown in **Table 2**.

Table 2: Chemical Requirements of titanium implants [74].

Element	Composition (%)			
	Grade 1	**Grade 2**	**Grade 3**	**Grade 4**
Nitrogen, max	0.030	0.030	0.050	0.050
Carbon, max	0.080	0.080	0.080	0.080
Hydrogen, max	0.015	0.015	0.015	0.015
Iron, max	0.200	0.300	0.300	0.500
Oxygen, max	0.180	0.250	0.350	0.400
Titanium	balance	balance	balance	balance

In the titanium alloys group, the most commonly used is the Ti–6Al–4V [29, 39, 69] due to its enhanced biocompatibility, acceptable elastic modulus (110 GPa), and superior strain-controlled and notch fatigue resistance (290 MPa) [69].

However, despite their excellent performance, these materials present important limitations:
  ➢ Low osteoconductivity, which results in the encapsulation of the implant with fibrous tissue (osteoblasts cells activity) and delays the healing time [75].

- ➢ Stress shielding, or the reduction in bone density as a result of removal of typical stress from the bone by an implant [76–78]. The load transfer at the implant/bone interface is strongly affected by the differences in modulus of elasticity and mechanical strength [76–78].
- ➢ The mechanical misalignment produces bone resorption (osteoclasts cells activity) due to the reduction of stress on the bone tissue [76–78]. This phenomenon may result in loosening of the implant, as well as fracture of bone and/or titanium.

To control these limitations, the surface is coated with HAp, as it resembles the properties of bone and teeth. The HAp coating would reduce the release of metallic ions by acting as a barrier [75], enhance the bone bioactivity by virtue of its chemical constituents [3, 9, 75], and promotes the adhesion and proliferation of cell [79, 80], allowing the bone to grow.

Recently, there has been an increasing interest in hydroxyapatite nanoparticles for its similarity to crystal bone phase and enhanced biomedical properties [75]. There are studies [81, 82] that support the significant improvement in mechanical properties and cellular interactions through the synthesis of nano-crystals of hydroxyapatite (nHAp).

Balassundaram G. et al [83] evaluated the biological response in synthesizing micro- and nanocrystalline HAp surfaces. They found a large difference between the surface area (8 m^2/g for mHAp and 160 m^2/g for nHAp) which results in a higher interaction with the surrounding cells.

The main limitation of the HAp is that it is brittle and weak, so its applications are limited as orthopedic and dental implants [75]. The most attractive approaches to solve this problem is the incorporation of certain inorganic materials to improve the cellular interaction of osteoblasts with the implant, as well as to increase the resistance [84]. Several metal elements, such as strontium (Sr), magnesium (Mg), zinc (Zn), sodium (Na), silicon (Si), silver (Ag), and yttrium (Y) play an important role in bone formation and also affect the mineral characteristics as well as mechanical properties [84].

2.3 Sintering

Sintering is a heat treatment process in which a powder or porous material, already formed into a specific shape, is converted to a useful solid [85]. Variables such as temperature, particle size, applied pressure, particle packing, composition and sintering atmosphere influence the microstructure that is produced.

As stated by Champion, E. [59], sintering of a ceramic powder requires suitable thermodynamic and kinetic conditions. He summarized its fundamentals and physico-chemistry as follow [59]:

➢ Sintering will occur only when the driving force is sufficiently high. It is possible if the total Gibbs free energy (G) of the system is minimized (dG < 0) by decreasing the solid–gas surface area A_{sg}(-dA_{sg} < 0) of high energy (γ_{sg}), which is replaced by a solid–solid surface area A_{ss} (dA_{ss} > 0) of lower energy (γ_{ss}) [59]:

$$dG = dA_{ss}\gamma_{ss} + dA_{sg}\gamma_{sg}$$

Equation 1

➢ A reduction in surface energy due to a reduction in the internal surface of the system provide the driving force for sintering [59]. Diffusion is thermally activated, and the effective pathway depends on the chemical and physical properties of the material, and composition of the gaseous atmosphere [59].

➢ For solid-state pressureless sintering, the phenomena is generally divided in three sequential stages [59]:
  a) First, the inter-particle neck forms and grows. In this stage, a relative density of ~65% of the theoretical density can be obtain [59], as shown in **Figure 4a.**
  b) Second, the densification occurs, due to the shrinking of the pores [59]. Pores remain open and constitute a continuous phase. This stage covers the major part of sintering and corresponds to an increase in relative density to ~90% [59], as shown in **Figure 4b**.

c) The isolated pores may disappear altogether, leaving a nearly fully dense ceramic. Then, during cooling to room temperature, the sample retracts in accordance with the expansion coefficient of the sintered ceramic [59], as shown in **Figure 4c**.
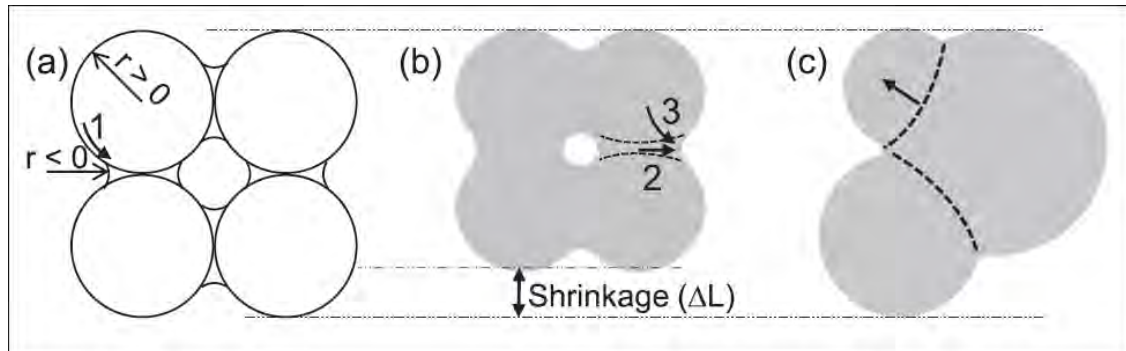
Figure 4: Spherical particles model: a) formation of necks between grains; b) densification and pores shrinkage; c) coalescence and grain growth [59].

➤ For liquid-state sintering, the intervention of a liquid phase assists the densification and prevents the grain growth [59]. In general, this process follows a sequence: Melting of the additives and redistribution, rearrangement of the majority solid phases and densification of the solid phase [59].
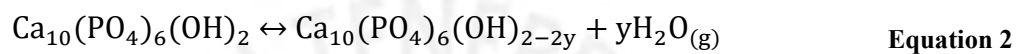
2.3.1 Sintering of HAp

Different studies were carried out with the aim of improving the mechanical properties of HAp by applying appropriate sintering additives or heat treatment to sinter dense samples [85–88]. Among them, pressureless sintering of HAp in the solid-state regime under surface or volume diffusion control is considered the most efficient process, due to its very high levels of purity and uniformity in starting materials, good control of grain size during the input stages and easy handling of equipment [1, 6, 85].

Pressureless sintering is the sintering of a powder to obtain a compact material without applying pressure. Depending on the material, this process can reach a maximum temperature between 0.5 and 0.9 of its melting point [89]. This avoids density variations in the final composition, which might occur using more traditional hot pressing methods [90].

Physical and chemical stability plays an important role during sintering. As summarized by Champion, E. [59], pressureless sintering of HAp is generally performed in the temperature range of 1100–1250 °C. In this domain, densification occurs without the formation of any liquid phase.

Investigations focused on structure have confirmed that no secondary phases, neither crystalline nor amorphous, are formed [59]. Indeed, HAp remains stable up to ~1350–1450 °C in ambient air [59]. Only partial dehydration of HAp into oxyhydroxyapatite may occur according to a reversible reaction [59]:

$$\text{Ca}_{10}(\text{PO}_4)_6(\text{OH})_2 \leftrightarrow \text{Ca}_{10}(\text{PO}_4)_6(\text{OH})_{2-2y} + y\text{H}_2\text{O}_{(g)} \qquad \textbf{Equation 2}$$

At the microscopic scale, solid-state diffusion in crystalline solids requires the presence of point defects within the crystal structure [59]. The matter transfer may proceed through several different diffusion pathways involving superficial, volume or grain boundary diffusion.

It is important to mention that during sintering numerous phenomena occur [85, 91]:

a) Increasing the temperature produces irreversible physico-chemical transformations that modify the chemical and crystalline structure.
b) The pieces also undergo temporary modifications, among which the expansion due to the heating is the most important. If the variations do not occur regularly during the sintering, the pieces will exhibit a lack of uniformity and residual stresses.
c) The surface heats faster than the interior. This temperature gradient results in a faster external contraction, causing cracks in the product.

The sintering curve should be set in accordance to the characteristics of the HAp. Therefore, it is necessary to control the heating rate since a rapid shrinkage can lead to stresses and breakage. The sintering curve is called heating regime. The heating regime can be simple, as in isothermal sintering, or have a complex temperature-time relationship, as in rate-controlled sintering [89].

2.3.2 Heating regime

A general heating regime for ceramics powders is shown in **Figure 5**. De Jonghe, L.C. & Rahaman, M.N [89] summarized its general scheme, which includes the conversion and burnout of additives and removal of volatiles such water as follows:

- ➢ Stage 1 is a few hundred degrees centigrade. The heat-up rate should be carefully controlled, because the rapid heating causes boiling and evaporation of organic additives, leading to specimen bloating or even shattering. The absorbed water is burned.
- ➢ Stage 2 can be included to promote chemical homogenization, reaction of powder components or burning of additives, if that is the case.
- ➢ Stage 3 represents the heating up to the isothermal sintering stage 4, during which the majority of the densification and microstructure development takes place. Stage 4 is then followed by a cool-down.
- ➢ An additional hold stage 5, prior to the final cool-down of stage 6, may also be included to relieve internal stresses or to allow precipitation or other phases.
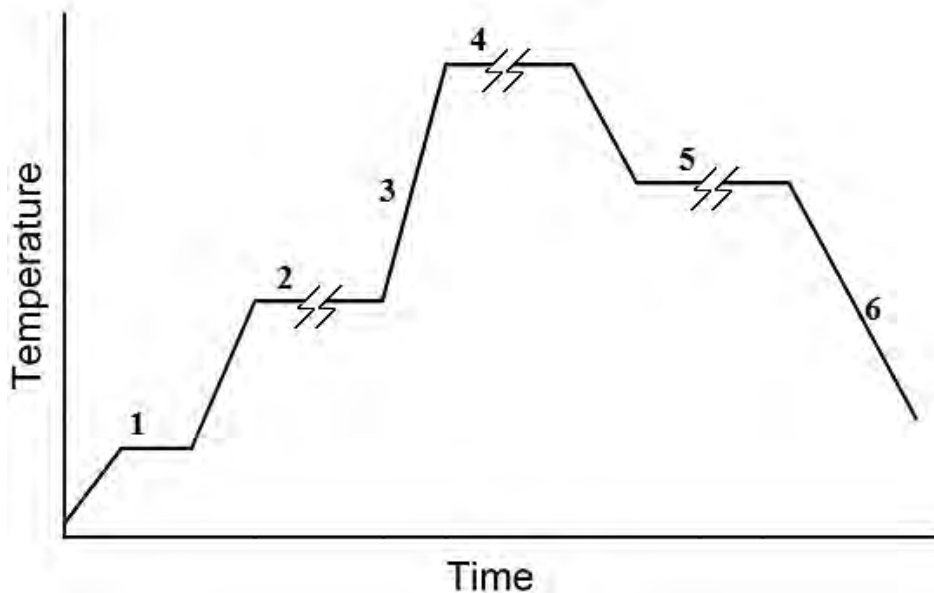

Figure 5: Generalized heating regime for ceramics powders (adapted from [89]).

According to the thermo-gravimetric analysis (TGA) realized by Ashok, M. et al. [92], shown in **Figure 6**, HAp platy-shaped crystals presents a two-stage weight loss at the temperature range of 30–140 and 250–410 °C. In the first stage, a sharp 5% weight loss is observed, indicating the evaporation of adsorbed water [92].

The second stage presents a 2% weight losses due to the adsorbed and lattice water [92]. No further weight loss is observed on heating the material up to 1200 °C, indicating the high thermal stability of the HAp [92].

Polymer materials used as additives, such as polyvinyl alcohol (PVA) and polyethylene glycol (PEG), have boiling points < 250 °C (228 and 238 °C respectively). Depending on the amount added, the hold time for stage 2, which is usually between 300 and 400 °C, should be increased [93].
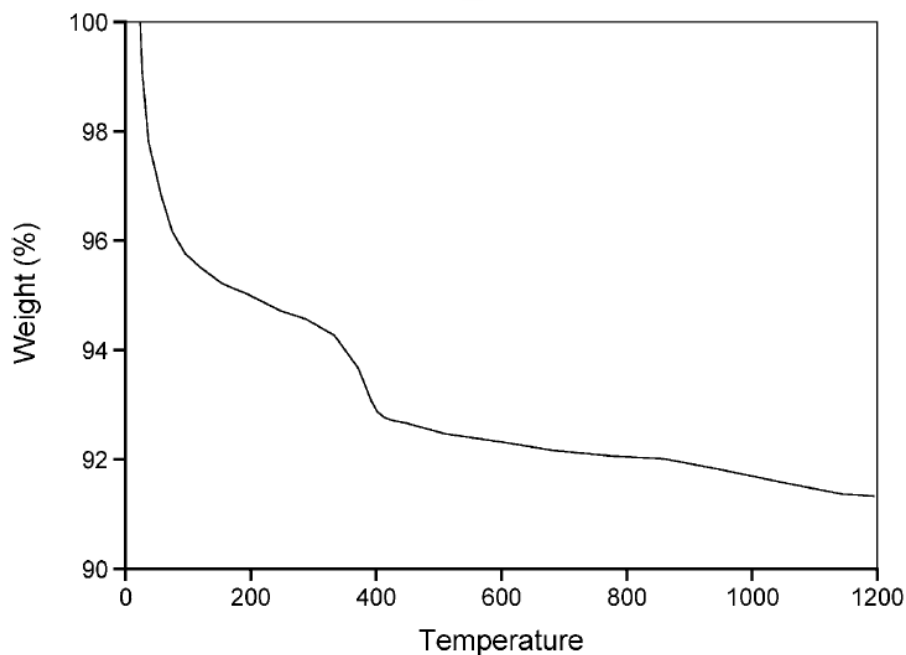
Figure 6: TGA graph of platy crystals of hydroxyapatite (27x2 μm) [92].

The control of the sintering atmosphere is also important. The precise control of the gas partial pressure as a function of temperature may be beneficial [59]. Insoluble gases trapped in closed pores may obstruct final stages of densification, in these cases, a change of the sintering atmosphere or vacuum sintering is indicated [89]. Most commonly, the sintering might take place in vacuum [94], inert gas (N_2, Ar) [95, 96] or moist air [96]. Generally, moisture was introduced in the sintering atmosphere to prevent dehydroxylation [59], as shown in **Equation 2**.

Dehydroxylation is delayed by increasing the partial pressure of water vapor [59]. Therefore, moisture may also affect the grain growth by promoting grain coalescence at low temperatures, e.g. 400 ˚C, when superficial diffusion is active [59].

2.4 Film deposition techniques applied to the biomedical field

Nowadays, several deposition techniques have been used to fabricate crystalline thin films of HAp, well adherent to the substrate and with a controlled morphology for biomedical application. However, due to the large CPCs family and the structural complexity of the HAp, the production of thin films with these characteristics is still a challenge. Some of the techniques include:

- Dry deposition techniques: (plasma spraying, sputter coating, pulsed laser deposition).
- Wet deposition techniques (sol–gel deposition).
- Electro-mechanic techniques (electrospray deposition).

Among them, those of the first group have wider distribution as they provide higher deposition rates as well as the possibility of covering large areas [48]. **Table 3** summarizes the characteristics of different of coating techniques, including their advantages and limitations.

**Table 3:** Different techniques to deposit HAp coatings [48].

Technique	Thickness	Advantages	Disadvantages
Plasma spraying	30-200 µm	High deposition rates; low cost	Line of sight technique; high temperatures induce decomposition; rapid cooling produces amorphous coatings
Sputter coating	0.5-3 µm	Uniform coating thickness on flat substrates; dense coating	Line of sight technique; expensive time consuming; produces amorphous coatings
Pulsed laser deposition	0.05-5 µm	Coating with crystalline and amorphous; materials as well as dense and porous	Line of sight technique
Sol-gel	< 1 µm	Can coat complex shapes; low processing temperatures; relatively cheap as coatings are very thin	Some processes require controlled atmosphere processing; expensive raw materials
Electro deposition	0.1-2 mm	Uniform coating thickness; high deposition rates; can coat complex substrates	Difficult to produce crack-free coatings; requires high sintering temperatures

2.4.1 Plasma spray technique

Plasma spraying is nowadays the main commercial technique for the deposition of CPCs, it is used to cover titanium implants due to its high deposition rates and practicality [18].

The technique consists in creating a high temperature plasma jet generated by an electric arc or discharge at high frequency [97]. The plasma usually contains a primary heavy gas (Ar or N_2) for the mass flow and a secondary gas (H_2, He) to improve the heat transfer [97, 98]. The main temperatures obtained are in the range of 5000-8000 K for diatomic gases, and 10000-20000 K for monatomic gases (Ar, He) [98]. Such higher temperatures are significantly above the melting point of any known material, as it is necessary to compensate the energy loss of the hot particles (mainly radiative loss to the surroundings). Another reason is the short exposure time of the particle in the hot jet (milliseconds) for reaching their melting temperature. Further details can be found in reference [99]. Once the plasma has been created, the powder material that is to be melted and deposited on a surface of interest is injected [98].

The common properties of the obtained HAp films have: high thermal stability, chemical stability, high hardness, low fracture strength, low adhesion to the substrates, low heat conduction and high porosity [48, 97]. HAp coatings produced by plasma spraying at high temperatures usually have secondary crystalline phases such as TCP and CaO [17, 24]. The **Figure 7** shows a schematic of plasma spray deposition technique.
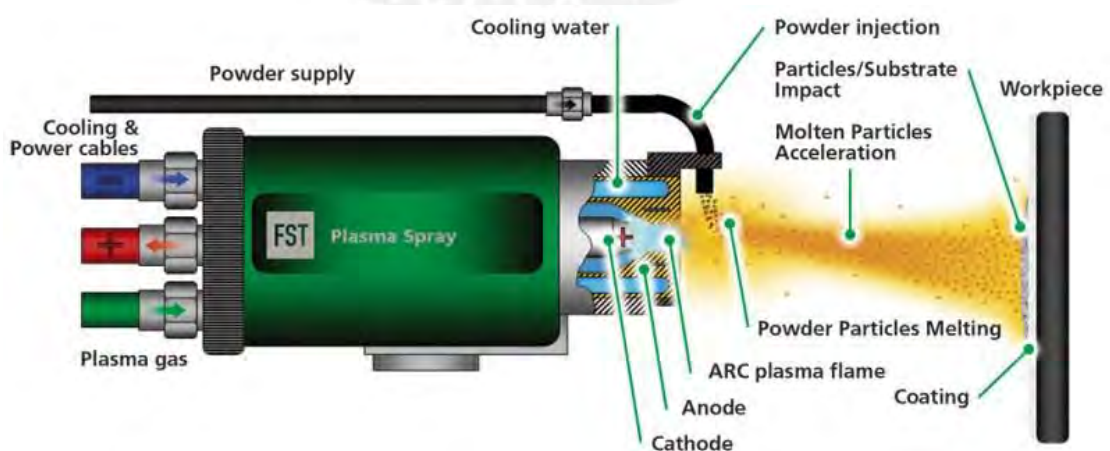

Figure 7: Scheme of plasma spray deposition [100].

2.4.2 Sol–gel technique

Ceramic syntheses by sol–gel have been widely used in recent years for the purpose of depositing CPCs on metal substrates due to their practicality and stoichiometric control [32–34, 101]. The technique of sol–gel consists in the polymerization of an organometallic precursor in an alcohol or water based solution (sol) with an acidic or basic solvent (gel) in order to produce the ceramic. As shown in **Figure 8**, for the fabrication of HAp coatings, Ca and P precursors are transformed into a solution and then deposited on a substrate, after a fast evaporation of the solvent and subsequent condensation reaction, a gel-shaped film is formed. The solid material is obtained after drying and calcination [102].

As stated by Liu, D.-M. et al. [103], this technique offers a molecular-level mixing of the calcium and phosphorus precursors, improving the chemical homogeneity of the resulting HAp to a significant extent, in comparison to conventional methods such as solid state reactions or wet precipitation. But it is known that, generally, this technique leave thick, cracked and porous coatings with low adhesion between the substrate and the coating, all of which are amorphous at room temperature [32–34, 101–103].
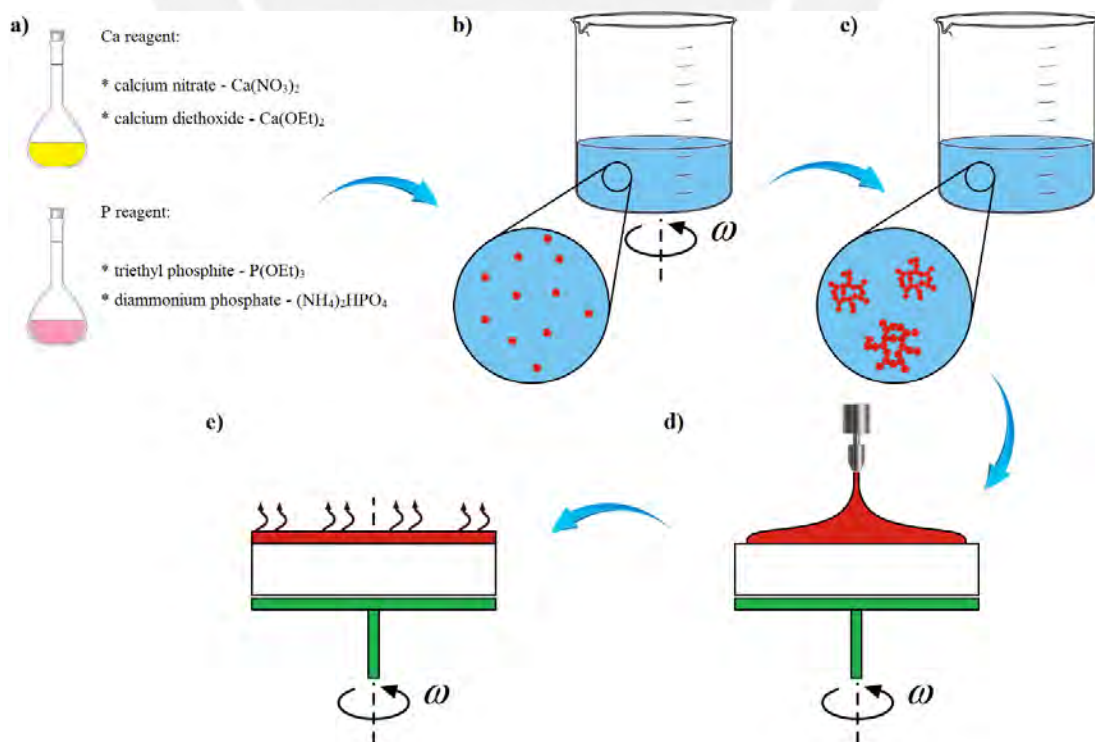

Figure 8: Scheme of sol–gel deposition: a) common reactants are added; b) reactants are mixed with H_2O or $H_2O/EtOH$ solution; c) solution is aged (gelation); d) spin coated; e) dried and annealed.

2.4.3 Electrodeposition technique

Electrodeposition is the process that allows the preparation of solid deposits on the surface of conductive materials [104].

This technique is commonly used to apply thin films of material to the surface of an object to change its external properties such as to increase corrosion protection, increase abrasion resistance, improve decorative quality, or simply to deposit a layer which is part of a more complicated device [104–106]. Due to the use of an electric field, electrodeposition is particularly suited for the formation of uniform films on substrates of complicated shape, impregnation of porous substrates, and deposition on selected areas of the substrates [104, 105].

Two electrodeposition processes have been developed for CPCs films: electrolytic deposition (ELD, from a saline solution) and electrophoretic deposition (EPD, from a solution of CPCs particles in suspension), as shown in **Figure 9**. As summarized by Zhitomirsky, I. [107], the features of both processes are shown in **Table 4**.
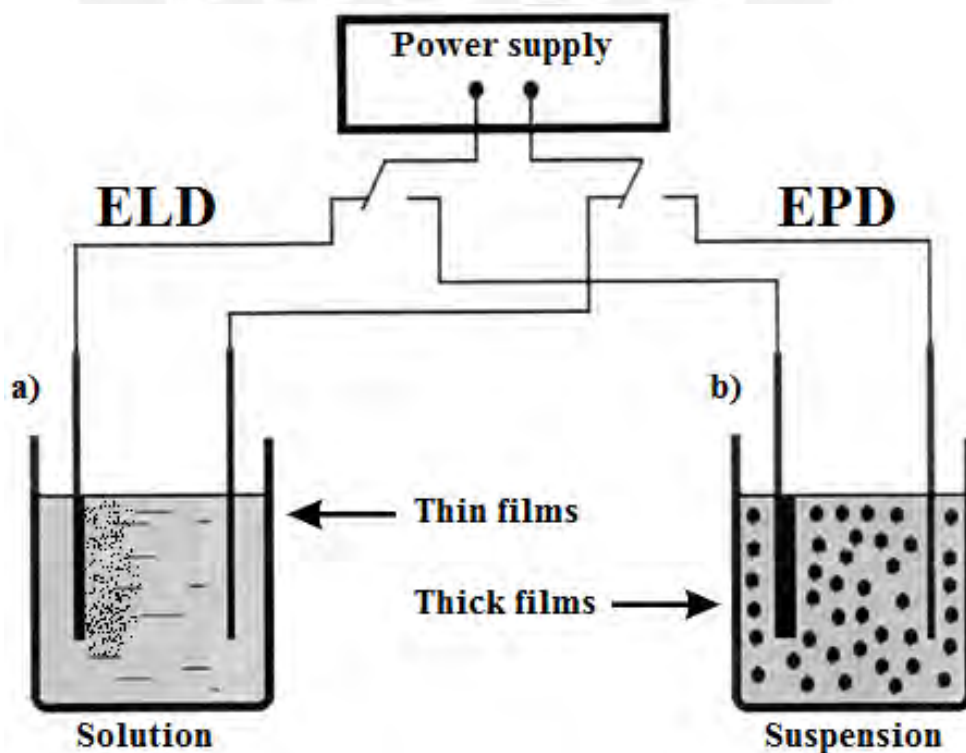
Figure 9: Scheme of electrodeposition by (a) electrolyte and (b) electrophoresis (adapted from [107]).

Table 4: Main features of electrophoretic and electrolytic deposition for ceramics [107].

| Characteristic	Electrophoretic Deposition	Electrolytic Deposition
Medium	Suspension	Solution
Moving species	Particles	Ions or complexes
Electrode reactions	None	Electrogeneration of OH^- and neutralization of cationic species
Preferred liquid	Organic solvent	Mixed solvent (water-organic)
Required conductivity of liquid	Low	High
Deposition rate	$1\text{-}10^3$ mm/min	$10^{-3}\text{-}1$ mm/min
Deposit thickness	$1\text{-}10^3$ mm	$10^{-3}\text{-}10$ mm
Deposit uniformity	Limited by size of particles	On nm scale
Deposit stoichiometry	Controlled by stoichiometry of powders used for deposition	Can be controlled by use of precursors

One important characteristic of these HAp coatings is low processing temperature, covering a range from ambient temperature [108, 109] to below 100 °C [109, 110]. Other characteristics include: Rigid control of the thickness (micrometric coatings > 100 μm) and good microstructure control [35–39]. On the other hand, the formation of cracks and pores, as well as non-stoichiometric and amorphous films were reported [48, 104].

2.4.4 Sputtering coating technique

The sputtering technique has been extensively developed for the production of high quality HAp films for biomedical applications [48, 111].

In this technique, ions formed in a plasma (ionized state of matter) are accelerated applying an electric field towards the material to be deposited (target), located at the cathode. The plasma usually is ionized gas (from Ar, N_2 or O_2). The voltage between the cathode and the anode causes the plasma ions to strike the target surface with high energy and transfer some of its energy to the target atoms (collision cascade) [48, 111].

The multiple collisions induced by the energetic particles of the plasma excites some of the atoms in the material with sufficient energy to leave the surface, reach the substrate and adhere to it. Most of the energy provided by the incident ions is converted into heat, which is dissipated by a cooling circuit which prevents overheating of the cathode [48, 111]. **Figure 10** illustrates the basic components of a sputtering chamber.
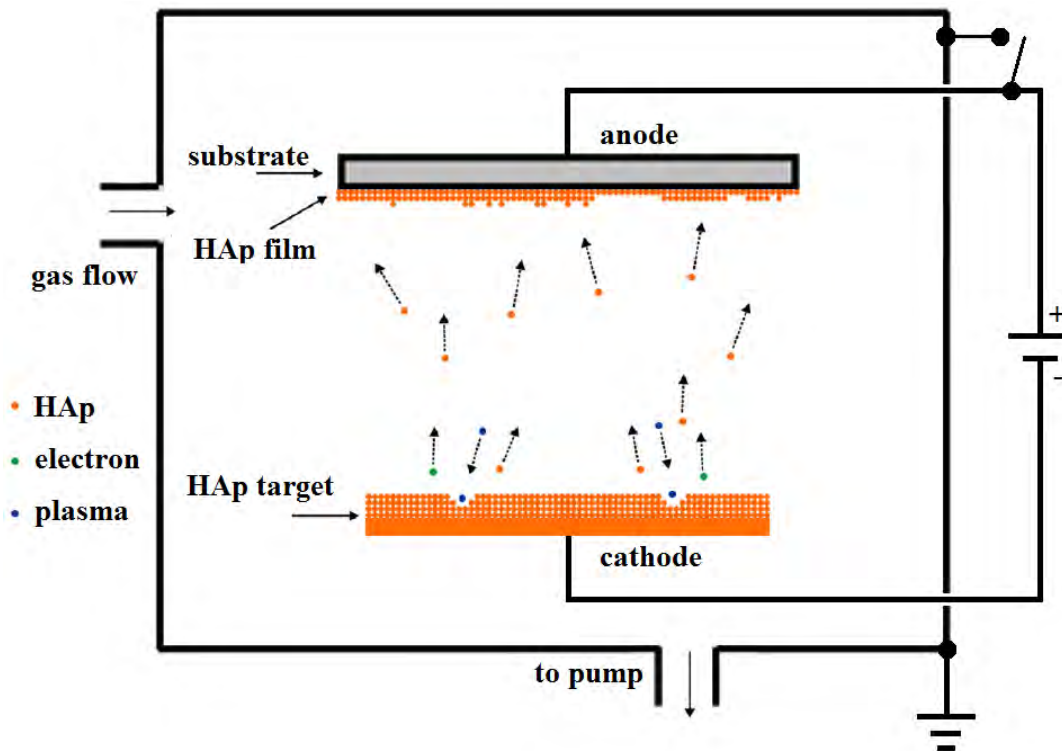
Figure 10: Schematic diagram of the sputtering mechanism (adapted from [111]).

This technique allows to coat large areas on flat substrates more uniformly than any of the other techniques mentioned before. Dense coating can be produced, without high temperature. But, like the HAp coatings produced using the plasma spraying technique, alteration in coating properties have been observed with the sputtering process [112–114].

Another important disadvantage of this technique is the low deposition rate. To increase the deposition rate, an increase of the ionization rate of the process gas is necessary [48, 111]. This is achieved by the application of magnetic fields perpendicular to the electric field. In this way, the secondary electrons generated during the bombardment are confined in a region close to the surface of the cathode [48, 111, 115]. This modification is referred to the magnetron sputtering technique, as shown in **Figure 11**.
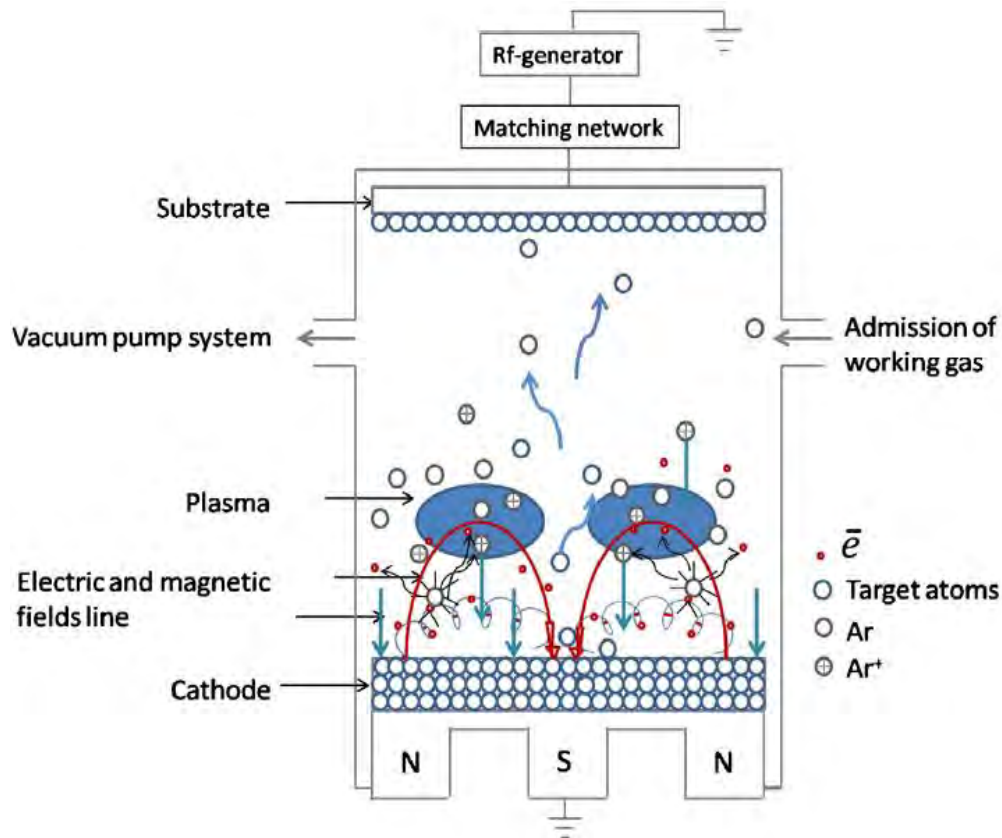
Figure 11: Schematic diagram of the typical RF magnetron sputtering facility with Ar$^+$ plasma [115].

The addition of the magnetic field significantly increases the ion density near to the target, therefore the amount of process gas can be reduced [48]. As a result, this allows sputtering at lower pressures (10^{-3} mbar commonly, compared to 10^{-2} mbar) and voltages (commonly 500 V, compared to $2 - 3$ kV) [48]. This bombardment does not cause damage to the thin films formed on the substrate and maintains the stoichiometry and thickness uniformity of the deposited thin film [115].

The fabricated HAp films offer good adhesion to the substrate [115, 116]. It is important to note that the thickness of the film depends on the discharge power and the deposition time. As the discharge power increases, the energy of the ions in the plasma increases, promoting a higher erosive effect on the target as well as a deposition in less time [117, 118].

Despite its excellent performance, this process also has disadvantages:
a) The process is more difficult to combine with a lithography process (e.g. lift-off for structuring the film) as the diffuse transport, which is characteristic for

sputtering, makes a full shadow impossible. Thus, one cannot fully restrict where the atoms go, which can lead to contamination problems [116].

b) The magnetic field erodes the target non-uniformly, wasting much of the material as the sputtering is more intense where the lines of magnetic field are parallel to the surface of the cathode. The erosion profile of the target takes a particular V-shape, as shown in **Figure 12** [118].
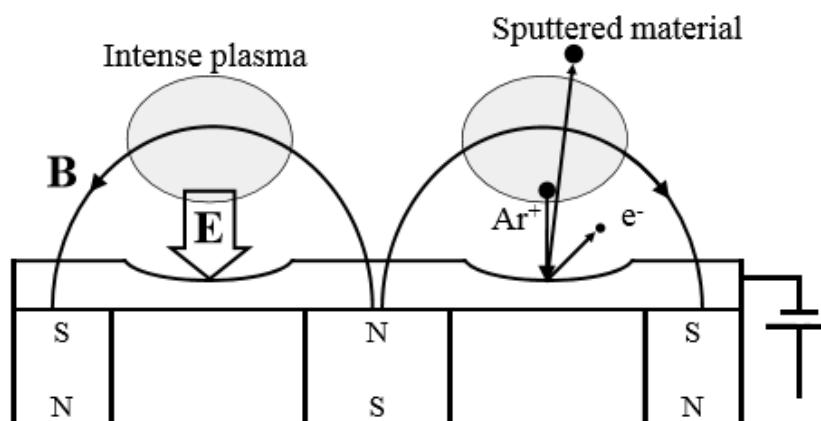
Figure 12: Wear zones in the target. Where the electrons are trapped, gas will be ionized and sputter target material. Below this intense plasma, the target erosion will be prominent [118].

2.4.5 Ion beam sputter technique

The fabrication of CPCs thin films by ion beam sputtering (IBS) has gained wide acceptance due to the homogeneous structure and high phase stability [119].

In this technique, the coatings are produced in a vacuum chamber. IBS utilizes an ion source to generate a relatively focused ion beam directed at the target to be sputtered [120]. The ion source consists of a cathode and anode with a common central axis [120]. Applying a high voltage field (2-10 kV) to the anode creates an electrostatic field inside the ion source, confining electrons around a saddle point in the center of the source [120].

When gas (usually Ar) is injected into the ion source, the high electric field causes the gas to ionize, creating a plasma inside the source region [120]. The ions are then accelerated from the anode region to the exit aperture (cathode) creating a collimated ion beam [120]. The resulting ion beam impinges upon a target material and, via momentum

transfer between the ion and the target, sputters this material onto the substrate [120]. A schematics of the IBS process is shown in **Figure 13**.

The as–deposited HAp films are characterized by having a high bond strength (~38 MPa) in comparison to those produced by plasma spray (~6 MPa) [122], which results in a better adhesion.

Other characteristics include: low deposition rate, which allows a better control in the uniformity and density of the film, being more stable and mechanically durable. In addition, as a sputter technic, the films obtained are completely amorphous [121, 122].
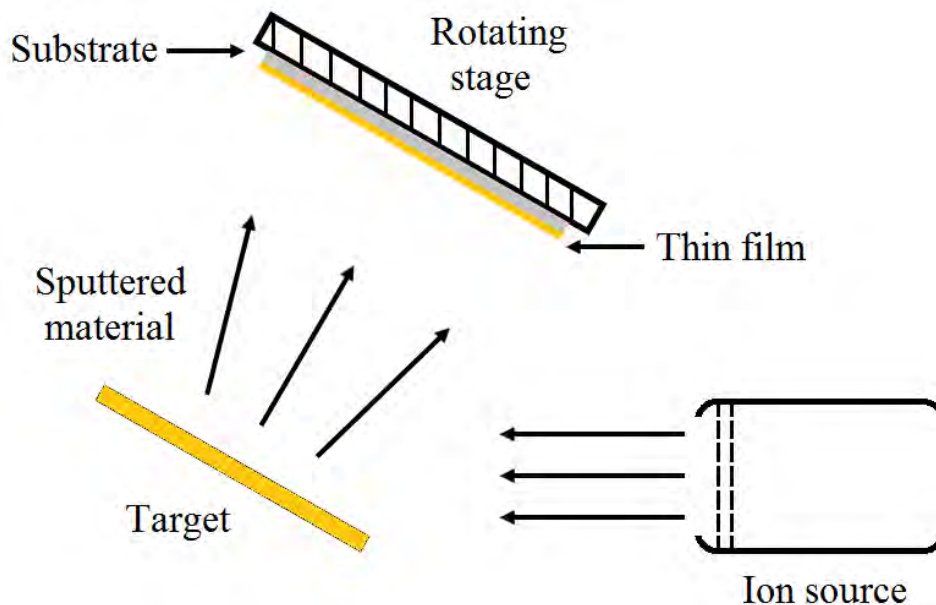
Figure 13: Schematic representation of ion beam sputter deposition (adapted from [121]).

2.4.6 Annealing of HAp films fabricated by sputter techniques

The success or failure of an implant also depends on the crystallinity of the HAp film. In general, amorphous HAp films exhibit high dissolution rates [122], resorb too rapidly to provide *in vivo* implant–bone bonding [123] and show a higher inflammatory cell response compared to crystalline HAp [124]. Sputtering coating using multi-component ceramic targets such as HAp and other CPCs materials would produce coatings whose chemistry was different upon deposition than the bulk target Ca/P ratio from 1.6 to 2.6 [112–114].

As stated by Ong, J.L. & Lucas, L.C [112], the difference in the Ca/P ratio between the HAp target and the sputtered coatings has been attributed to the preferential deposition of Ca ions and a possible significant loss of P ions, which may be pumped away before reaching the substrate. Other investigations suggest the loss of phosphorus ions, due to a weaker bonding of P ions to the growing film; they are thus more readily sputtered away by incoming ions or electrons [113].

According to different works [29, 112–114, 125, 126], the as–sputtered coatings were confirmed to be amorphous by X-ray diffraction analysis.

As suggested by Van Dijk et al. [126], a heat treatment (annealing) after sputtering is a good alternative to convert the amorphous HAp films into a crystalline form. Generally, for thin films, annealing is supposed to occur in two steps: recrystallization and grain growth. In the recrystallization process time and temperature are related [126]. The effect of increasing the temperature reduces the time needed to finish recrystallization [123].

An increase in coating crystallinity after annealing was reported in the range of 400 °C to 800 °C [128, 129]. In addition, the annealing time varies between 30 min and 4h [122, 125] and the heating rates ranges from 5 °C/min to 12 °C/min [127, 129]. Annealing involves many complex phenomena, such as formation of specific structural phases, nucleation and crystal growth, which modifies stress/strain generated during fabrication of thin film and affects the bonding between the film and the substrate [112–114, 121–129].

3. Experimental Methods

This chapter includes a description of the HAp target and the HAp thin films fabricated. Only the target used in Ilmenau was fabricated with HAp powders. The target used in Lima was a commercially bought one. The characterization techniques used to investigate the structure, densification and linear shrinkage, morphology, composition, hardness and roughness of the samples are described in each case.

3.1 Powders compressing and sintering

HAp powders (MEDICOAT, sintered and crushed powders, particle size between 45 and 130 μm) were initially compressed in a cylindrical die (φ = 40 mm) using a manual uniaxial molding press (Weber-Pressen) at room temperature. Once the pressure for the different experiments was reached, as shown in **Table 5**, eight minutes were added as maintenance time at this pressure.

Table 5: Sintered conditions for the green discs. The compressing pressures were applied before sintering.

| Regime	HAp weight (g)	Additives	Pressure (MPa)
2h, 1200 °C, air (first test)	15.0	H_2O (3 %wt)	24
	5.0	H_2O (3 %wt)	24
	3.5	H_2O (3 %wt)	24
4h, 1200 °C, air (second test)	2.3	H_2O (3 %wt)	40
	2.3	H_2O (3 %wt)	56
	2.3	H_2O (3 %wt)	72
	2.3	H_2O (3 %wt)	80
2h, 1200 °C, air (third test)	2.3	H_2O (3 %wt)	72
	2.3	PEG (2 %wt) + PVA (1 %wt)	72
4h, 1200 °C, air (third test)	2.3	H_2O (3 %wt)	72
	2.3	PEG (2 %wt) + PVA (1 %wt)	72

The precision etching and coating system (PECS) equipment requires a target with the follow dimensions: Diameter of 19 mm and thickness between 0.9 and 1.1 mm. Therefore, 3 tests were performed in order to obtain a suitable thickness:

- The first test was performed varying the weights of HAp, as shown in **Table 5**, using 24 MPa and H_2O as a binder. The thickness after sintering of discs with 15, 5 and 3.5 g was 7.65 mm, 2.45 mm and 1.78 mm respectively. For the next test, the weight was reduced to 2.3 g, the sintering time and the pressure was increased.

- The second test was performed with 2.3 g and 4h at different pressures, as shown in **Table 5**, observing the behavior. The values of thickness can be found in chapter 4, **Table 10**. The thickness of the sintered discs were in the suitable range. The disc sintering at 72 MPa was selected due to a better distribution of the material (good surface finishing and no cracks).

- The third test was conducted with 2.3 g at 72 MPa, using a sintering time of 2h and 4h, using H_2O as a binder and a mixture of additives in order to improve the mechanical strength of the green discs, as polyvinyl alcohol (PVA 13000, 50wt% in aqueous solution) as binders and polyethylene glycol (PEG 600, 30wt% in aqueous solution) as a plasticizer. The amount added are shown in **Table 5**. The values of thickness can be found in chapter 4, **Table 11**. The thickness of the sintered discs were in the suitable range. The fabricated discs were selected for obtaining the HAp targets.

The green produced discs were measured (thickness and diameter) before and after sintering to calculate linear shrinkage. In addition, the final weight was also measured to calculate the densification. The values can be found in chapter 4, **Table 8, Table 9, Table 10** and **Table 11**.

After the compression of powders, the HAp discs were sintered at 1200°C in air atmosphere with 5 °C/min using an oven Nabertherm with manual controller for programing the thermal cycle. As mentioned before, pressureless sintering of HAp is generally performed in the temperature range 1100–1250 °C [59], due to its high thermal stability [92].

Two different heating regimes (HR) were programed in the oven, as shown in **Figure 14**. The difference between them was the maintaining time at 1200 °C.
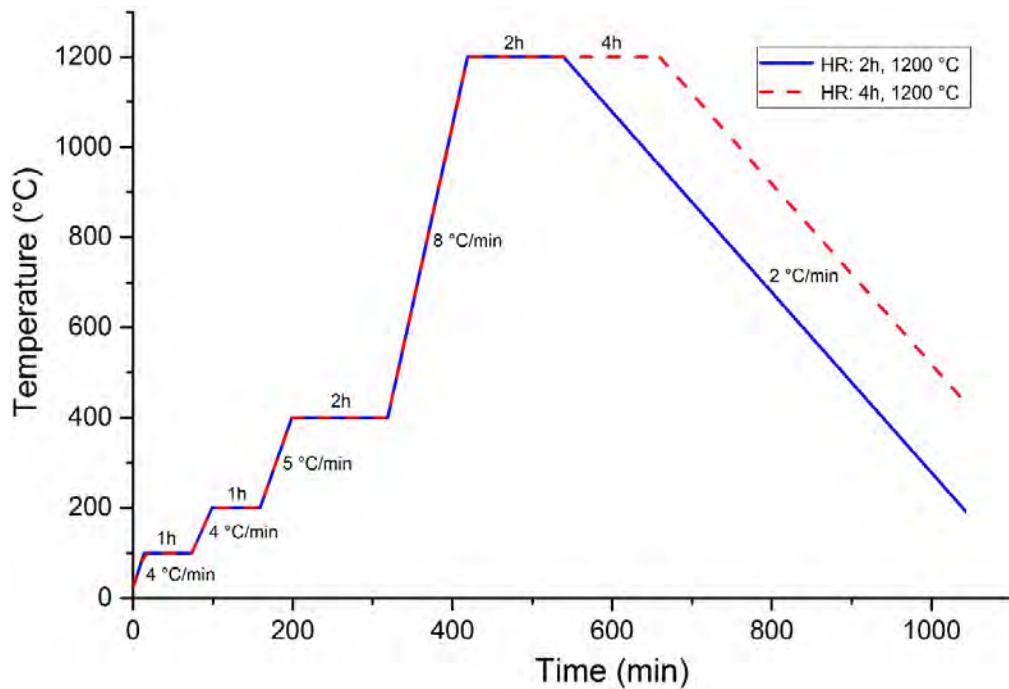
Figure 14: Heating regime (HR) programs used in the sintering of HAp powders.

In order to obtain a suitable diameter, the discs fabricated with 2.3 g at 72 MPa and 1200 °C (2h, 4h / PEG+PVA, H$_2$O) were cut with 3D-Micromac's microSTRUCT C laser, using a PicoBlade (Lumentum) laser source. The power used was 5 W with a wavelength of 355 nm in a pulse length of less than 10 picoseconds. The final product wa the HAp target, with a diameter of 19 mm.

3.2 Sputtering coating

HAp thin films were grown using two different sputtering process, in order to compare the properties of the fabricated HAp films: Radio frequency (RF) magnetron sputtering and ion beam sputtering. The coating process in each case is described as follows:

3.2.1 RF-magnetron sputtering

The films were grown using a sputtering chamber "home-made" at PUCP in Lima. Rectangular shaped (4 mm x 3 mm) titanium alloy pieces (Ti–6Al–4V; ASTM F1108 grade 5 specification) were used as substrates. A HAp sputtering target (2 in. x 3 mm,

99.9% pure; Stanford Advanced Materials) was fixed on the chamber with a face-down mode.

The substrates were etched with HCl-30% at 80 °C for 20 minutes, in order to clean the surface and thus remove the titanium oxide (pickling). The base pressure was 1×10^{-5} mbar and the working atmosphere was a mixture of Ar (20 sccm) and O_2 (5 sccm). The gas mixture contained oxygen in order to compensate the oxygen pumped away during the sputtering process, as referred by Van Dijk, K. et al. [26]. The working pressure was around 6.7×10^{-3} mbar. The magnetron power was 100 W and the sputter time was 5h. The film obtained had a thickness of ~200 nm. A schematic of the RF-magnetron sputtering used in Lima is shown in **Figure 15**.
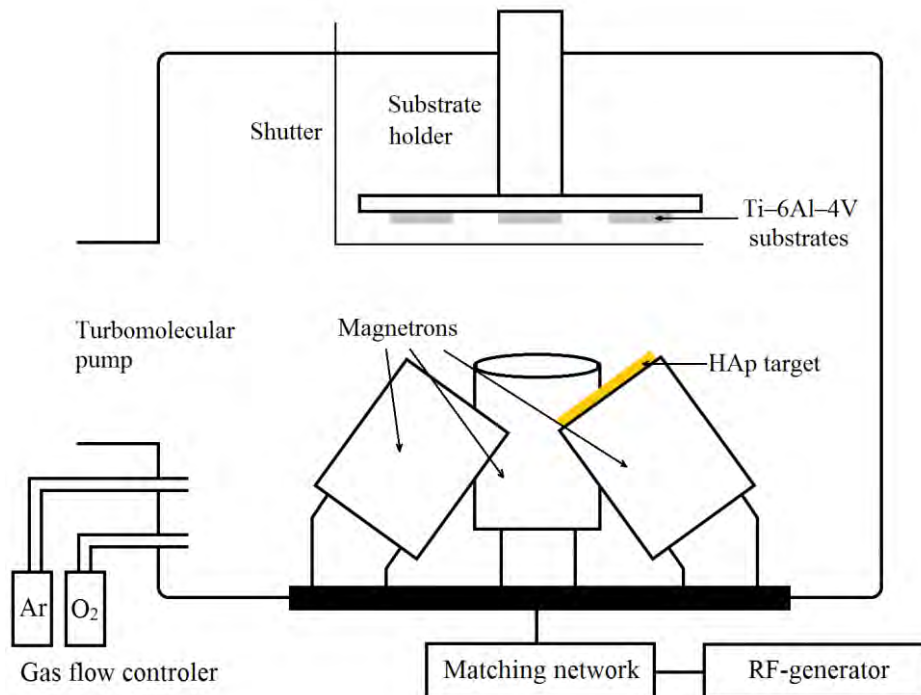
Figure 15: Side view of the RF-magnetron sputtering. The HAp target was fixed in one of the three magnetrons.

3.2.2 Ion beam sputtering

HAp thin films were grown from the HAp target fabricated with 72 MPa at 1200 °C (4h / PEG+PVA) on titanium disks (1 in. x 0.02 in.; ASTM-B-265/ASME-SB-265 grade 2 specification) substrates by ion beam sputtering (IBS) process using a Gatan Model 682 Precision etching and coating system (PECS).

A different substrate was used to see if there is an influence on the topography of the fabricated films. The substrates were etched with HCl-30% at 80 °C for 20 minutes, in order to clean the surface and thus remove the titanium oxide (pickling). The ion production was carried out using argon flow at 6.5 bar with two Penning ion guns (PIG) at 300 µA and energy beam of 4.5 keV. The substrate was rotated at 30 rpm, in order to produce a uniform film. The work pressure was 8×10^{-3} Pa. For the film production, a total of 10 cycles were taken, each cycle of 30 minutes (20 minutes of deposition and 10 minutes of cooling) resulting in a total time of 5 hours per sample. The deposition rate was 1.5 nm/min, therefore, the final thickness was ~300 nm. A schematic of the IBS process used in Ilmenau is shown in **Figure 16**.
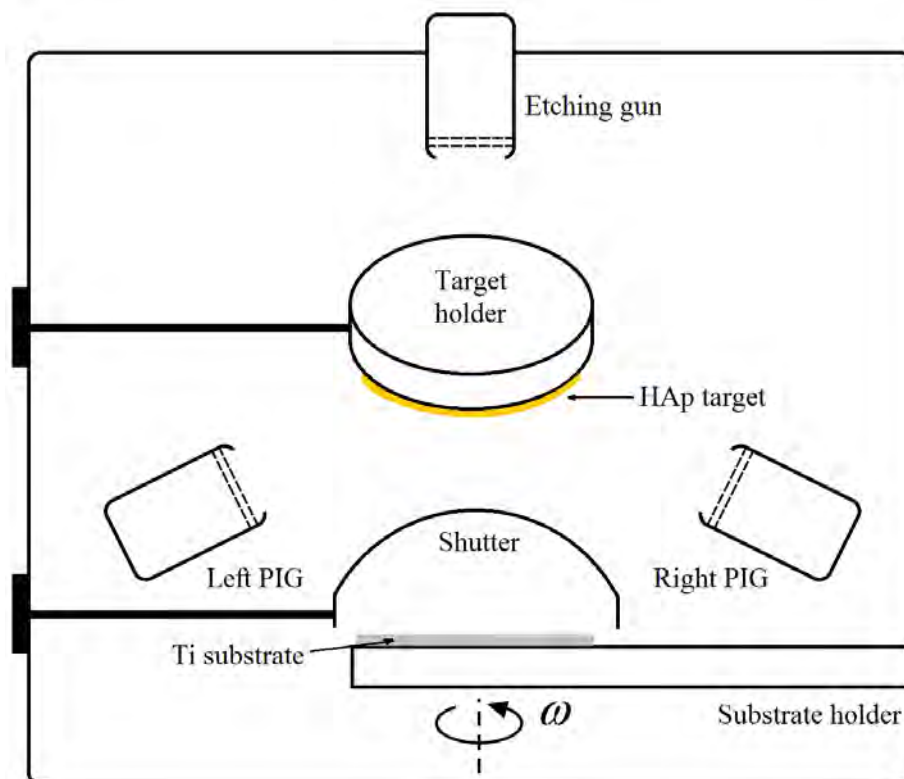
Figure 16: Schematic of the PECS system. Both Penning ion guns (PIG) were used at 300 µA, increasing the rate deposition. The etching gun was not used during the process. The inlet of the vacuum system is located on the back wall of the chamber.

After the deposition, both groups of samples were annealed in order to increase de crystallinity. Minimal crystallinity required for proper performance of HAp films is 62% [48]. The annealing was carried out in air atmosphere for 2h using a Carbolite CWF 11/13 laboratory chamber furnace with 4 °C/min at different temperatures: 400, 600 and 800°C for RF-magnetron sputtering samples; 600 and 800 °C for IBS samples.

3.3 Characterization techniques

3.3.1 X-ray diffraction characterization

The X-ray diffraction experiments were performed using Bruker D5000 Theta-Theta X-ray diffractometer, equipped with a Cu Kα (λ= 0.15418 nm) radiation source used at 40 kV and 40 mA and a Goebel mirror, which converts the X-ray beam coming from the X-ray tube into a parallel or focused beam and additionally monochromatizes it. Two configurations were performed depending on the sample analyzed:

a) Bragg-Brentano diffraction was performed to measure the diffraction intensity of the sintered disks. X-ray experiments were carried out using a time per step of 2 s, a step-size of 0.03°/step and a diffraction angle (2θ) covering the range from 5 to 70°.

b) Grazing incidence diffraction at an incident angle of 3° was performed to measure the diffraction intensity of the films deposited and annealed. X-ray experiments were carried out using a time per step of 2 s, a step-size of 0.03°/step and a diffraction angle (2θ) covering the range from 5 to 70°.

The peaks in an X-ray diffraction pattern are also directly related to the crystal size and crystallinity (fraction of crystalline phase) in the samples. The crystal size (τ) is calculated according to the Scherrer equation [130]:

$$\tau = \frac{K \cdot \lambda}{\beta_{hkl} \, cos\theta} \qquad \textbf{Equation 3}$$

Where K is the Scherrer constant and its actual value depends on at least three things: the width of the diffraction maximum measured at a height half-way between background and peak, the crystallite shape and the crystallite-size distribution; normally defined as 0.9 [130]; λ represents the X-ray wavelength used for the measurement, β_{hkl} is the line width of full width half maximum (FWHM) in radians and θ is the Bragg angle. As a rough measure of β, half the difference between the two extreme angles at which the intensity is zero, can be taken [130].

The crystallinity refers to the degree of structural order in a solid (arrangement of atoms or molecules). Therefore, it has a big influence on material properties such as diffusion, hardness or density. It can be determined from the XRD with the following equation [131]:

$$X_C = \left(\frac{0.24}{\beta_{hkl}}\right)^3 \qquad \textbf{Equation 4}$$

Where X_C is the crystallinity and β_{hkl} is the FWHM of selected reflection peaks, respectively. As suggested by Ilinsky, A.G. et al. [132] this parameter is determined by the height of the first maximum of the structure factor which is linearly dependent on a volume part of crystalline phase. Based on studies carried out by Landi, E. et al. [133], this FWHM correspond to the (002) reflection for HAp.

3.3.2 Densification and linear shrinkage

Densification is by far the most widely used measurement to characterize the sintering of a compacted particles based solid [85]. The progress of sintering is often determined from the density or the linear shrinkage of the compacted powder as a function of time or temperature during the heat treatment [85]. The bulk density is defined as the mass divided by the external volume of the body. A better parameter is the relative density (ρ), defined as the bulk density divided by the theoretical density of the solid [85], in the case of HAp, the theoretical density value is 3.156 g/cm^3 [9]. The following equation relates the relative density and porosity (P) [85]:

$$\rho = 1 - P \qquad \textbf{Equation 5}$$

The linear shrinkage is defined as [85]:

$$Linear\ shrinkage = \left(\frac{L_0 - L}{L_0}\right) \qquad \textbf{Equation 6}$$

Were L_0 is the original length and L is the length at a given time or temperature [85].

3.3.3 Scanning electron microscopy and energy dispersive X-ray spectroscopy

Scanning electron microscopy (SEM) coupled with energy dispersive X-ray spectroscopy (EDX) using a FIB-SEM Crossbeam AURIGA (ZEISS) was used to observe the morphology and chemical composition of samples.

For imaging, an acceleration voltage (EHT) of 5keV was used. For EDX analysis, the EHT is generally set to about 2.5–4.0 times the energy of the edge analyzed. Considering the Kα edge of calcium (~3.7 keV), the voltage set was 10 keV.

The working distance was 8.5 mm in all the cases. Carbon conductive tape, double sided coated, was used to make disks conductive for the SEM-EDX investigations.

3.3.4 Hardness measurements

The microhardness test was performed according to ISO 14577-1 [134]. The experiments were carried out using the Fischer Picodentor HM 500. The indentation tests were performed using 0.2 mN as maximum load and 20 s of maximum load application time.

The ratio between the indentation depth and film thickness was in the range of 1/10−1/20, in order to eliminate the influence of the substrate and guarantee its accuracy [135]. The maximum indentation depth was 0.02 μm for RF-magnetron sputtering samples and 0.03 μm for IBS samples.

Martens hardness (HM) is calculated commonly using the Oliver and Pharr method [136]. In this method, the hardness is given by:

$$HM = \frac{P_{max}}{A_C}$$
<div align="right">**Equation 7**</div>

Where P_{max} and A_C are denoted as the maximum indentation load and the projected contact area, respectively.

3.3.5 Roughness measurements

Surface roughness of the HAp films was measured by profilometry using a UBM Microfocus type 1080 profilometer with a source illuminator Cold Light Source Schott KL 1500 electronic. Each sample was measured to obtain the arithmetical mean roughness value (R_a), which is defined as the arithmetic mean of the values of the roughness profile within the individual measuring distance (l_r). It represents the average deviation of the profile from the middle line, as shown in **Figure 17** and is represented by:

$$R_a = \frac{1}{l_r} \int_0^{l_r} |z(x)|\, dx \qquad \qquad \textbf{Equation 8}$$
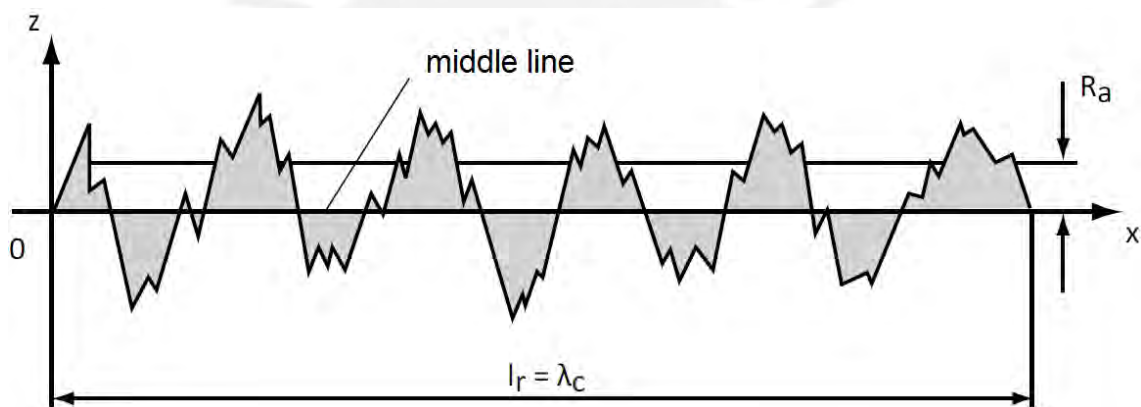
Figure 17: Schematic representation of the arithmetical mean roughness value (R_a) [137].

The value of R_a is calculated within the evaluation length (l_n), which generally consists of five sampling lengths (l_r). In addition, the stylus travel (l_t) is defined as the evaluation length plus start and finish lengths. These setups for roughness measurement are defined by DIN EN ISO 4287 and summarized in **Table 6**:

Table 6: Measurement conditions for roughness measurements [138].

Sampling lengths (mm)	Evaluation length (mm)	Stylus travel (mm)
0.08	0.40	0.48
0.25	1.25	1.50
0.80	4.00	4.80
2.50	12.50	15.00
8.00	40.00	48.00

This standard defines other roughness parameters, which are represented in **Figure 18**.

- The average roughness depth (R_z) is the sum of the height of the largest profile peak and the depth of the deepest profile valley within a single measurement section (l_r). Usually, R_z results from averaging the results of 5 l_r.
- The maximum individual depth (R_{max}) is the largest individual depth (R_z).
- The roughness depth (R_t) is the vertical difference of the deepest valley and the highest peak within the total measuring distance.
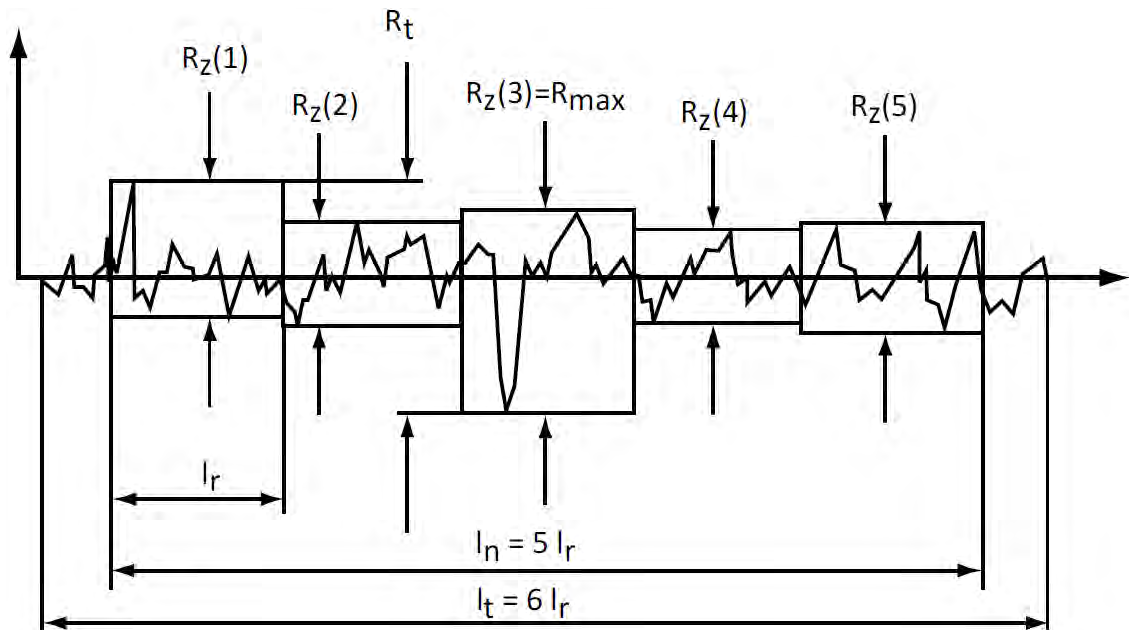
Figure 18: Schematic representation of roughness parameters [137].

Three individual measurements were made for each sample. The evaluation length was 3 mm and 10 mm for the samples fabricated with RF-magnetron sputtering and IBS respectively. The measurement speed was 0.13 mm/s and the frequency was 130 points/s.

4. Results and discussion

This chapter is divided in three main sections. The first section shows the results of the HAp powders and HAp discs used for IBS deposition. The second and third sections show the results of HAp thin films produced by RF-magnetron sputtering and IBS respectively.

4.1 Sintered HAp discs and targets

4.1.1 X-ray diffraction

The XRD pattern of the HAp powders and discs showed a structure very similar to the monoclinic hydroxyapatite given by standard ICDD PDF #89-4405, with lattice dimensions of $a_0 = 0.943$ nm, $b_0 = 1.886$ nm, $c_0 = 0.687$ nm. No impurity was observed in the XRD pattern, indicating that the achieved inorganic phase is crystalline HAp. The patterns are shown in **Figure 19**, **Figure 20** and **Figure 21** for the first, second and third test, respectively (**Table 5**).
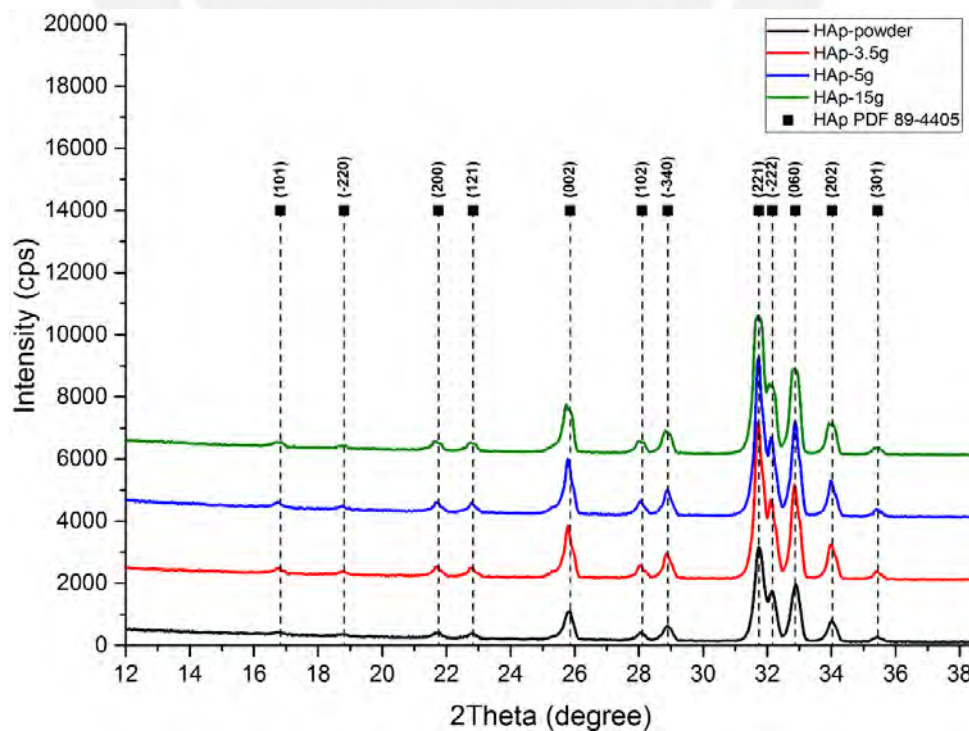
Figure 19: XRD of HAp powders and discs with 3.5g, 5g and 15g and 24 MPa at 1200 °C (4h / H_2O). The weight were measured before sintering. The pressures were applied before sintering. It can be observed that decreasing the weight does not affect the crystalline HAp pattern.
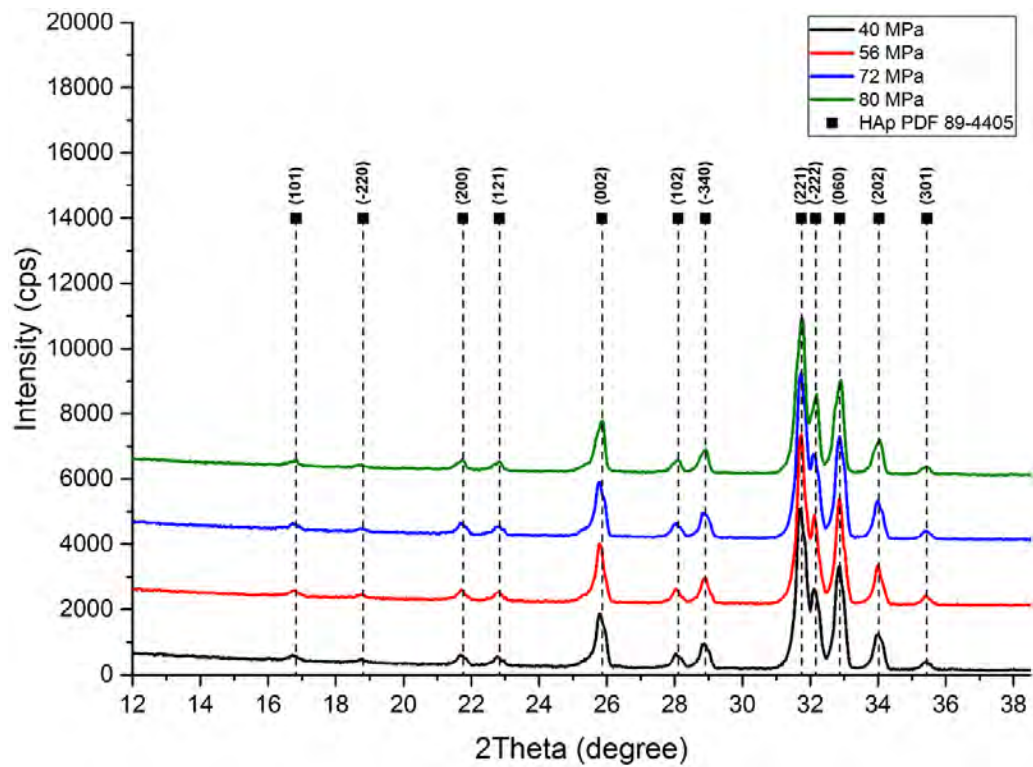
Figure 20: XRD of HAp discs fabricated with 40, 56, 72 and 80 MPa at 1200 °C (4h / H_2O). The pressures were applied before sintering.
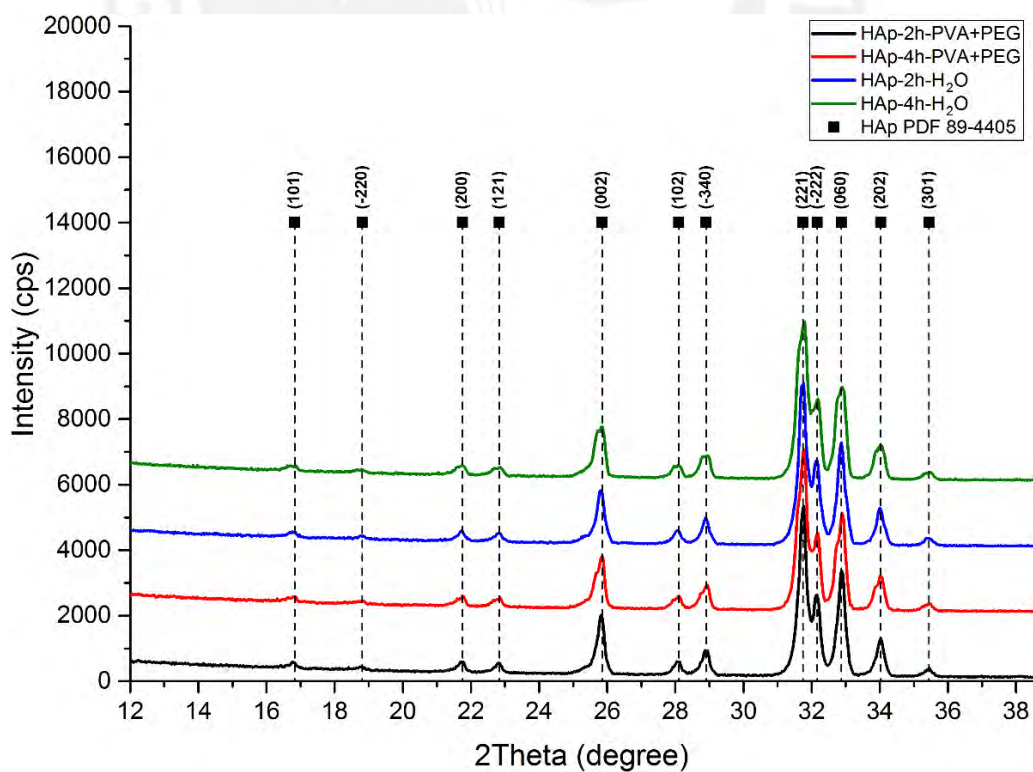

Figure 21: XRD of HAp discs fabricated with 72 MPa at 1200 °C (2h, 4h / PEG+PVA, H_2O). The pressure was applied before sintering.

At this point it can be said that the heating regime used for the sintering of the HAp is suitable for producing HAp sintered discs. The crystalline structure is preserved in all cases. It can be seen in the **Figure 22** that the pattern is maintained after laser cut, so this process does not alter the structure of the targets.
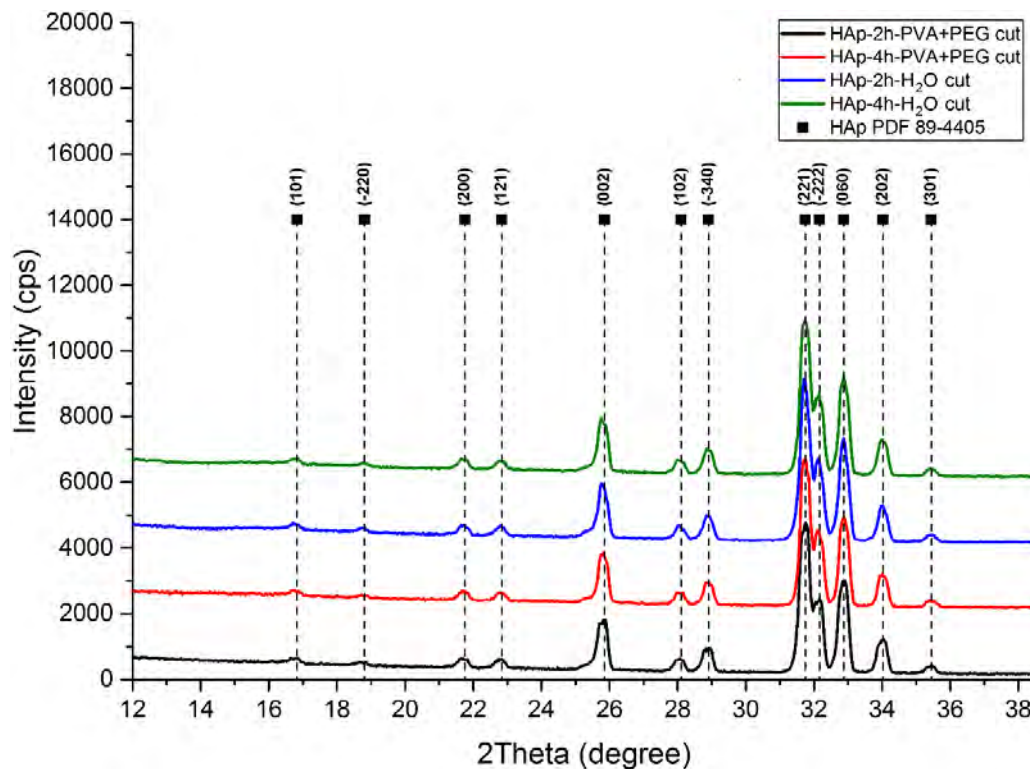
Figure 22: XRD of HAp cut targets with 72 MPa at 1200 °C (2h, 4h / PEG+PVA, H_2O). The pressure was applied before sintering.

The HAp discs fabricated with 2.3 g at 40, 56, 72 and 80 MPa and 1200 °C (4h / H_2O) and the HAp targets fabricated at 72 MPa and 1200 °C (2h, 4h / H_2O, PEG+PVA) after laser cut were taken in order to evaluate: Crystal size, to know what mechanism (densification or grain growth) predominates during sintering [89]; and crystallinity, to identify how this varies in the target and the films.

For calculating the crystal size, the first maximum peak (intensity) was taken, to avoid the effect of the noise. For calculating the crystallinity, the peak suggested by Landi, E. et al. [4] was taken. In both cases, the chosen peak corresponds to the plane (002). Using **Equation 3** and **Equation 4**, a plot was constructed and shown in **Figure 23**. In the case of the powders, the crystal size is 257.9 Å and $X_C = 39\%$. Here, the particle size refers to

the size of the micro powders, while the crystal size refers to the size of the crystal contained in the micro powder particles. Therefore, a HAp particle can contain several crystals. It can be seen in all cases that the crystal size in the sintered discs is higher than the powder, due to the sintering temperature in the last stage. There is no clear trend between the variation of crystal size and crystallinity with the pressure used.
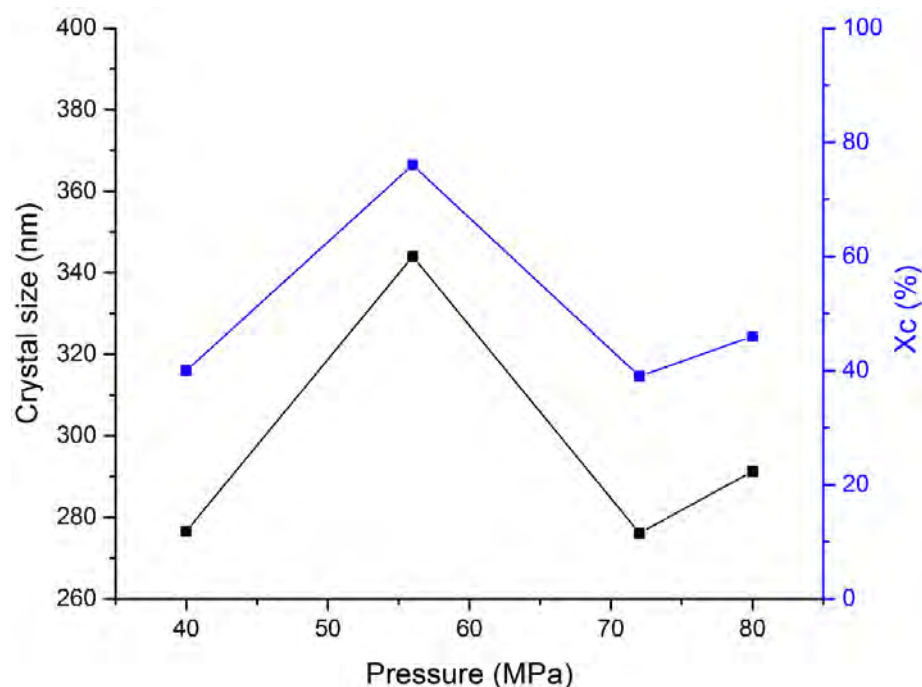
Figure 23: Variation of crystal size (black curve) and crystallinity (blue curve) vs. compaction pressure for the sintering discs with 40, 56, 72 and 80 MPa at 1200 °C (4h / H_2O).

The **Table 7** shows the crystal size of the target obtained after cutting. In all the cases the crystal size is higher than the same of the powders, while the crystallinity is the practically same. Increasing the time from 2h to 4h in the last holding stage (1200 °C), an increase in the crystal size and crystallinity is observed. This results confirm the influence of the holding time at high temperature on the crystal grown. Therefore, the addition of H_2O is more favorable for the crystal growth than the addition of PEG+PVA.

Table 7: Variation of crystal size and crystallinity of the HAp targets with 72 MPa at 1200 °C (2h, 4h / H_2O, PEG+PVA).

Target	Crystal size (Å)	Crystallinity (%)
2h, PVA+PEG	264.1	39
4h, PVA+PEG	276.4	40
2h, H_2O	265.5	40
4h, H_2O	281.1	41

4.1.2 Densification and linear shrinkage

As shown in **Table 8**, for HAp discs fabricated with 40, 56, 72 and 80 MPa at 1200 °C (4h / H_2O), increasing the pressure produces an increment in green density. A comparison between both the green and sintered density shows an increment of 28% ± 1% in all the cases. As shown in **Figure 24**, the density depends linearly on the compression pressure.

Table 8: Density behavior for HAp discs fabricated with 40, 56, 72 and 80 MPa at 1200 °C (4h / H_2O).

Pressure (MPa)	Green density (g/cm³)	Sintered density (g/cm³)	Variation (%)	ρ (%)
40	1.29	1.64	27	52
56	1.31	1.68	28	53
72	1.33	1.69	27	54
80	1.34	1.73	29	55
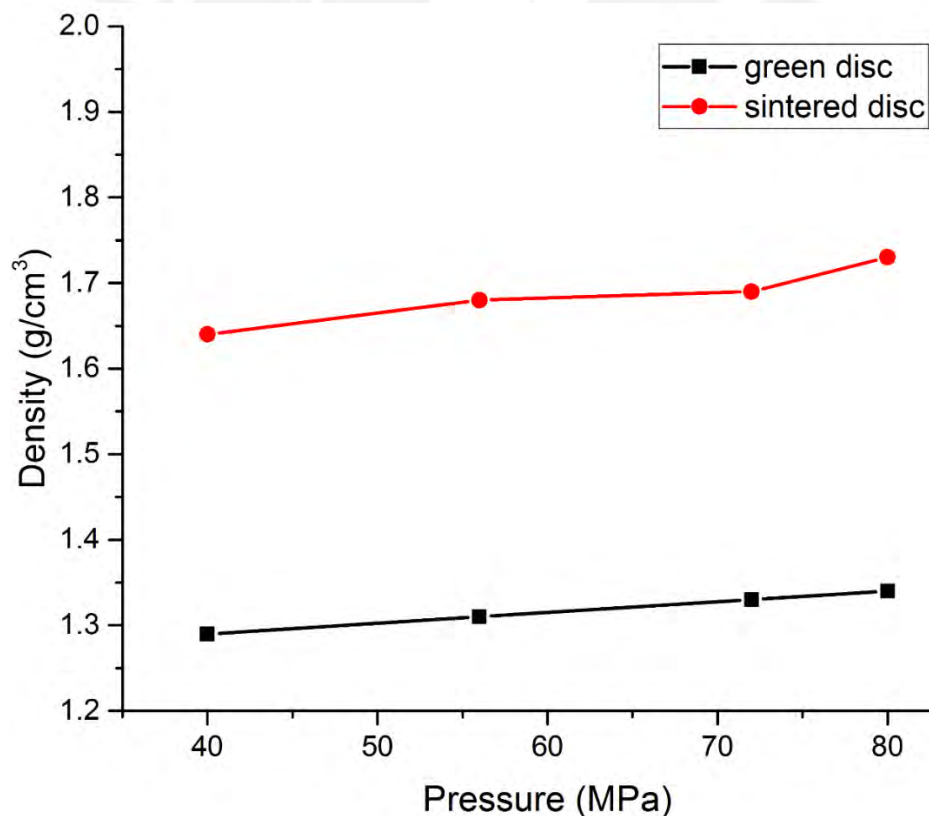
Figure 24: Variation of green density and sintered density vs. compaction pressure for HAp discs fabricated with 40, 56, 72 and 80 MPa at 1200 °C (4h / H_2O).

In the case of the HAp discs targets with 72 MPa at 1200 °C (2h, 4h / PEG+PVA, H_2O), the variation in density is shown in **Table 9**. Increasing the time from 2h to 4h in the last holding stage (1200 °C), an increase in the sintered density is observed. The higher values are obtained with the targets fabricated using PVA and PEG, especially with 4h.

Table 9: Density behavior for HAp discs fabricated with 72 MPa at 1200 °C (2h, 4h / H_2O, PEG+PVA).

Pressure (MPa)	Green density (g/cm³)	Sintered density (g/cm³)	Variation (%)	ρ (%)
2h, PEG+PVA	1.34	1.70	27	54
4h, PEG+PVA	1.34	1.78	33	56
2h, H_2O	1.33	1.61	21	51
4h, H_2O	1.33	1.69	27	54

It can be noticed that the sintered density is much lower than the theoretical density of HAp (3.156 g/cm³) with values of relative density (ρ) a little bit higher than 50%. This can be explained by the characteristics of the powders sintered. In general, powder obtained by sintering and crushing are less dense than those obtained from hydrothermal or sol–gel process due to its high porosity [139, 140].

The porosity has a high impact on densification. As referred by De Jonghe, L.C. & Rahaman, M.N [89], sintering involves a competition between coarsening and densification. For example, the vapor transport and surface diffusion compete with the densifying mechanism [89]. They lead to coarsening of the microstructure and a reduction of the driving force for sintering. Therefore, a significant reduction in the densification rate can result [89]. High porosity means more routes for the vapor to flow, which keeps the pore open and hinders the densification.

In other words, the production of ceramics with high density would require choosing sintering conditions so that the non-densifying mechanisms are inactive, for example the application of pressure, the adequate sintering atmosphere or the suitable heating regime [89]. When coarsening mechanisms dominate, the production of a highly porous solids is favored [89].

The **Table 10** shows the linear shrinkage for the discs with 40, 56, 72 and 80 MPa at 1200 °C (4h / H_2O). No significant trend with increasing the load was observed. It can be suggested that it is possible to further increase the pressure.

Table 10: Linear shrinkage variation for targets with 40, 56, 72 and 80 MPa at 1200 °C (4h / H_2O).

Pressure (MPa)	Green thickness (mm)	Sintered thickness (mm)	Variation (%)
40	1.42	1.12	21
56	1.40	1.10	21
72	1.38	1.10	20
80	1.37	1.09	20

The **Table 11** shows the linear shrinkage for the discs with 72 MPa at 1200 °C (2h, 4h / H_2O, PEG+PVA). Increasing the time from 2h to 4h in the last holding stage (1200 °C), produces an increase in the linear shrinkage.

Table 11: Linear shrinkage variation for targets with 72 MPa at 1200 °C (2h, 4h / H_2O, PEG+PVA).

Pressure (MPa)	Green thickness (mm)	Sintered thickness (mm)	Variation (%)
2h, PEG+PVA	1.37	1.08	21
4h, PEG+PVA	1.37	1.04	24
2h, H_2O	1.38	1.15	17
4h, H_2O	1.38	1.10	20

4.1.3 Scanning electron microscopy and energy dispersive X-ray spectroscopy

The morphology and particle size of HAp powders are shown in **Figure 25**. The size of the powder particles is 85 ± 25 μm. Particles exhibit an angular morphology, which is common on powders fabricated by sintering and crushing.
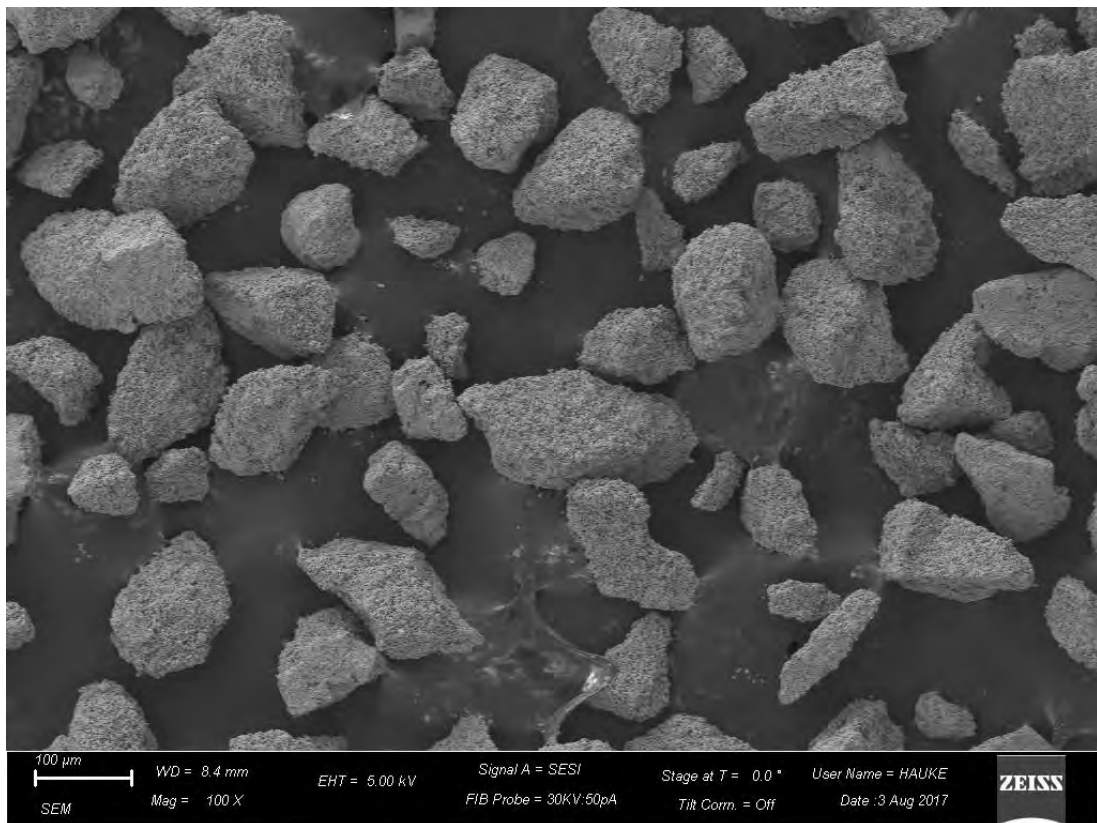
Figure 25: SEM micrographs of the HAp powders showing an angular morphology.

At lower magnification, **Figure 26**, the rough and porous surface can be seen. Furthermore, in **Figure 27**, the grain boundary and grain size, as well as the pore size (1.55 ± 0.44 μm) can be seen. Then, it is expected that agglomerates will not be completely crushed after pressing. In this situation, the densifying mechanisms during the sintering steps are not favored.
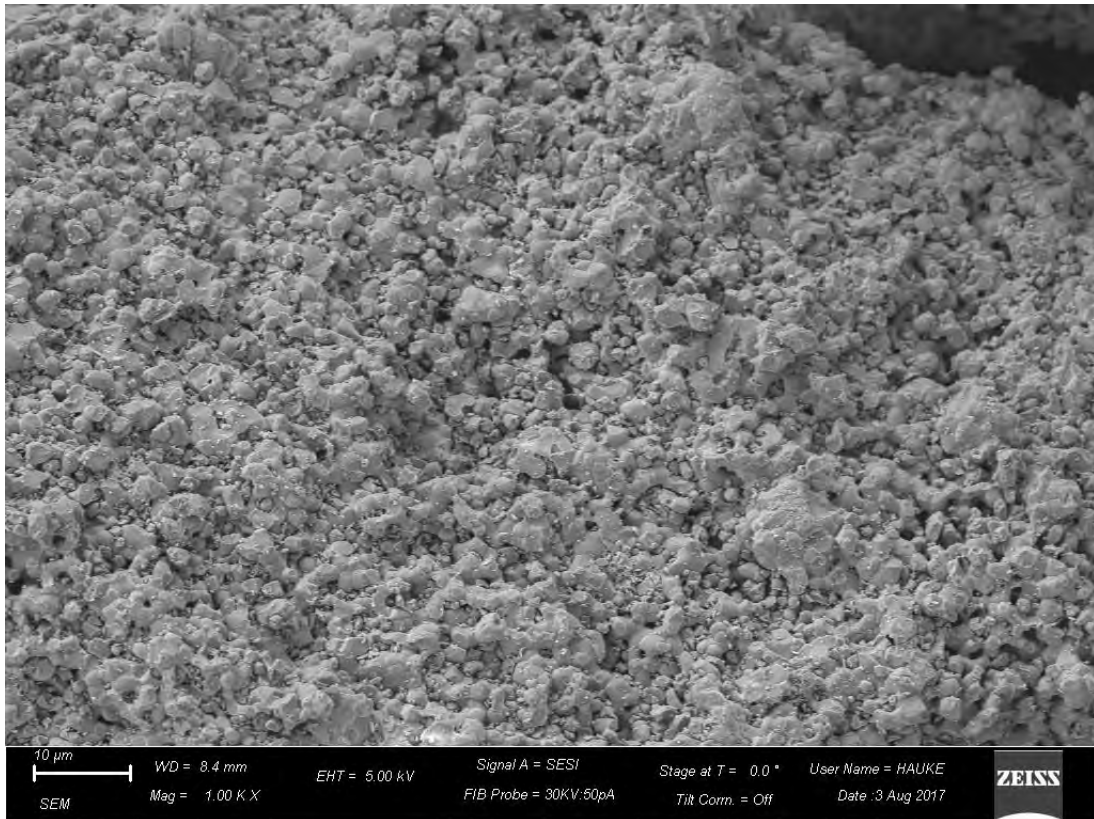
Figure 26: SEM micrographs of the HAp powders showing grainy porous surface.
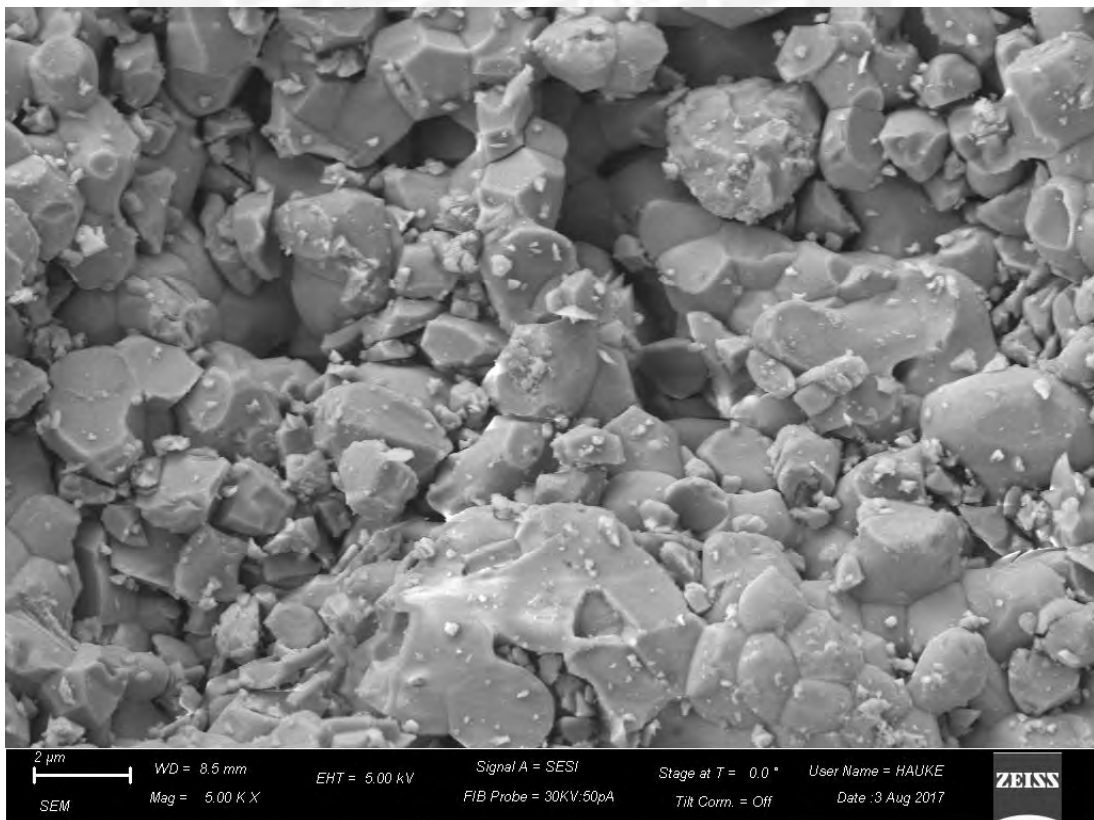
Figure 27: SEM micrographs of the HAp powders showing the grain limit and pores.

The chemical composition of the HAp powders obtained by EDX is shown in **Table 12**. The experimental ratios were calculated by dividing the at% in each case. In addition, the EDX spectrum is shown in **Figure 28**.

Table 12: Chemical composition of HAp powders and ratios.

Element	Wt%	At%	Error (%)
C	2.99	6.15	1.13
O	32.35	50.05	0.29
Mg	0.28	0.28	5.16
P	20.73	16.56	0.26
Ca	43.65	26.96	0.26

Ratios	Theoretical	Powder	
Ca/P	1.667	1.628	0.368
O/Ca	2.600	1.856	0.389
O/P	4.333	3.022	0.389
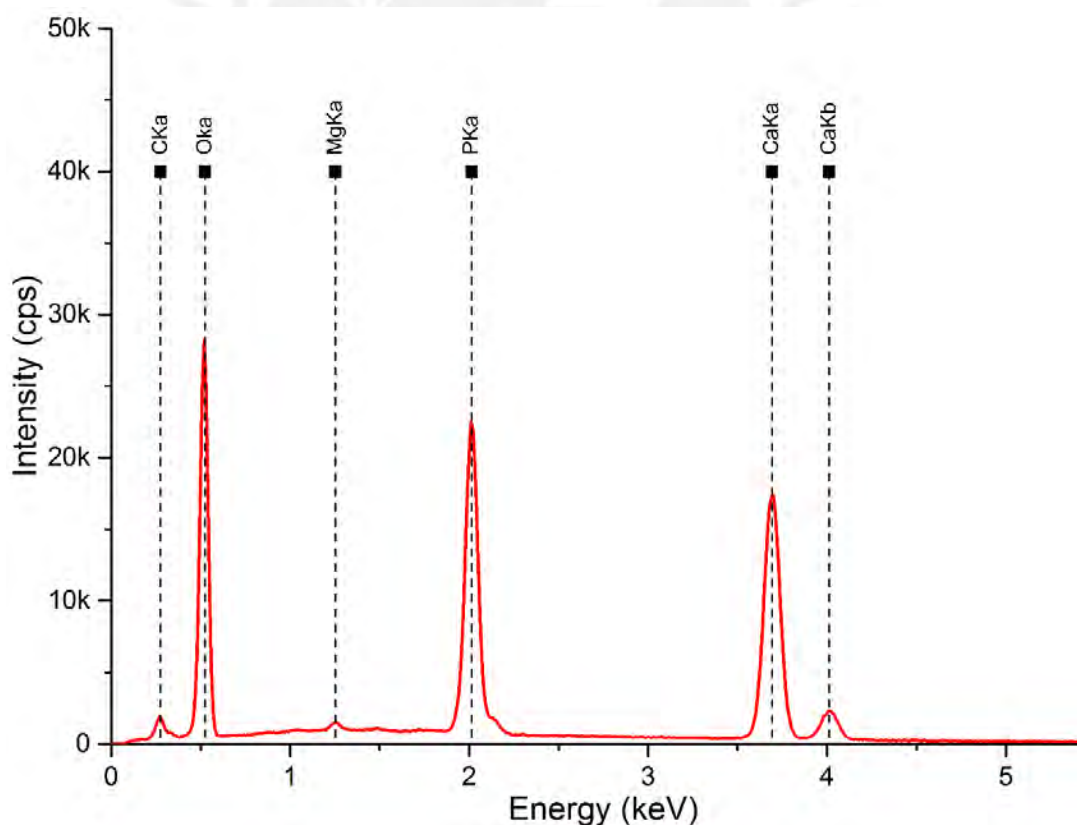
Figure 28: EDX spectrum of the HAp powders composed by C, O, Mg, P and Ca.

It can be seen that the ratios are lower in all the cases, this results suggest that the powders correspond to a sub-stoichiometric hydroxyapatite or other amorphous impurities.

In the first case, as stated by Landi, E. et al. [4], the presence of calcium-deficient hydroxyapatite (CDHA), usually expressed as $Ca_{10-x}(PO_4)_{6-x}(HPO_4)_x(OH)_{2-x}$, can be inferred as responsible of the reduction of the Ca/P ratio (1.50–1.67). On the other hand, Wang, H. et al. [141] suggest the presence of tricalcium phosphate (TCP) and summarized the variation in Ca/P ratios as a function of the volume percentage of TCP or CaO, as shown in **Figure 29**.
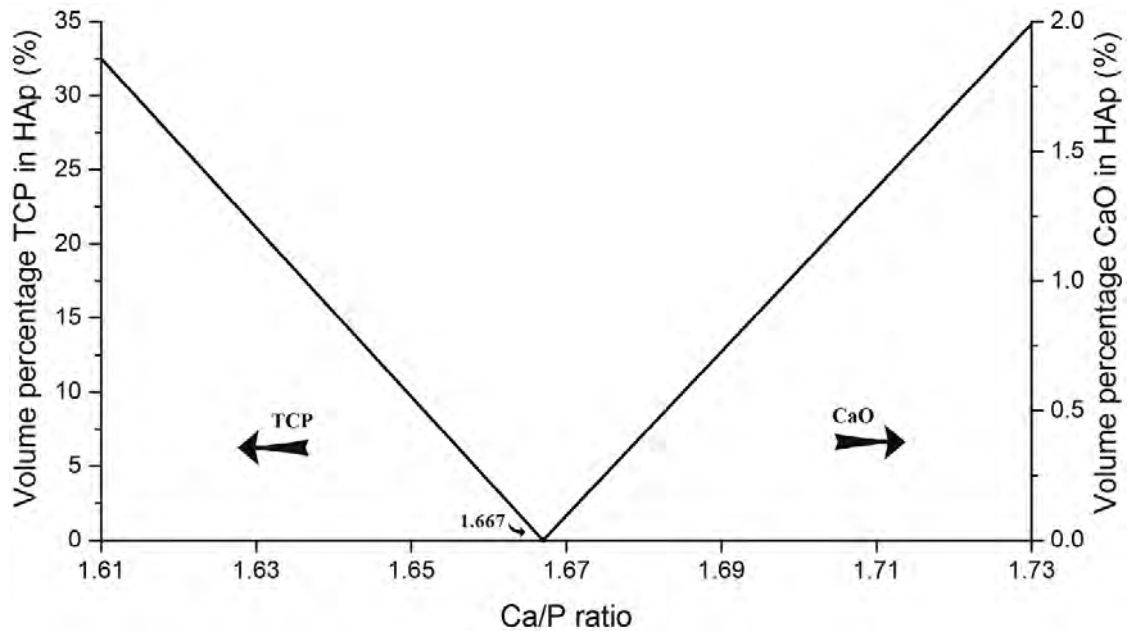
Figure 29: Volumetric percentage of TCP and CaO in HAp vs. Ca/P ratios (adapted from [141]).

Traces of other elements such as Mg and C can also be observed. If TCP exists in the powders, the presence of Mg can be attributed to the wide solid solution it has. The ideal β-TCP structure contains calcium ion vacancies that are too small to accommodate calcium ions, but allow the inclusion of magnesium ions, which thereby stabilize the structures [142]. Incorporation of a limited amount of Mg (0.4 wt%) was reported in synthetic apatites from aqueous systems [143]. Mg was shown to inhibit the crystal growth of synthetic apatite, even promoting the formation of amorphous calcium phosphate (ACP) at high concentration [143].

SEM was applied to evaluate the surface topography of the cross section of the targets. The SEM investigation of HAp targets sintered with 72 MPa and 1200 °C (2h, 4h / PEG+PVA, H_2O) after laser cut is shown in **Figure 30**.
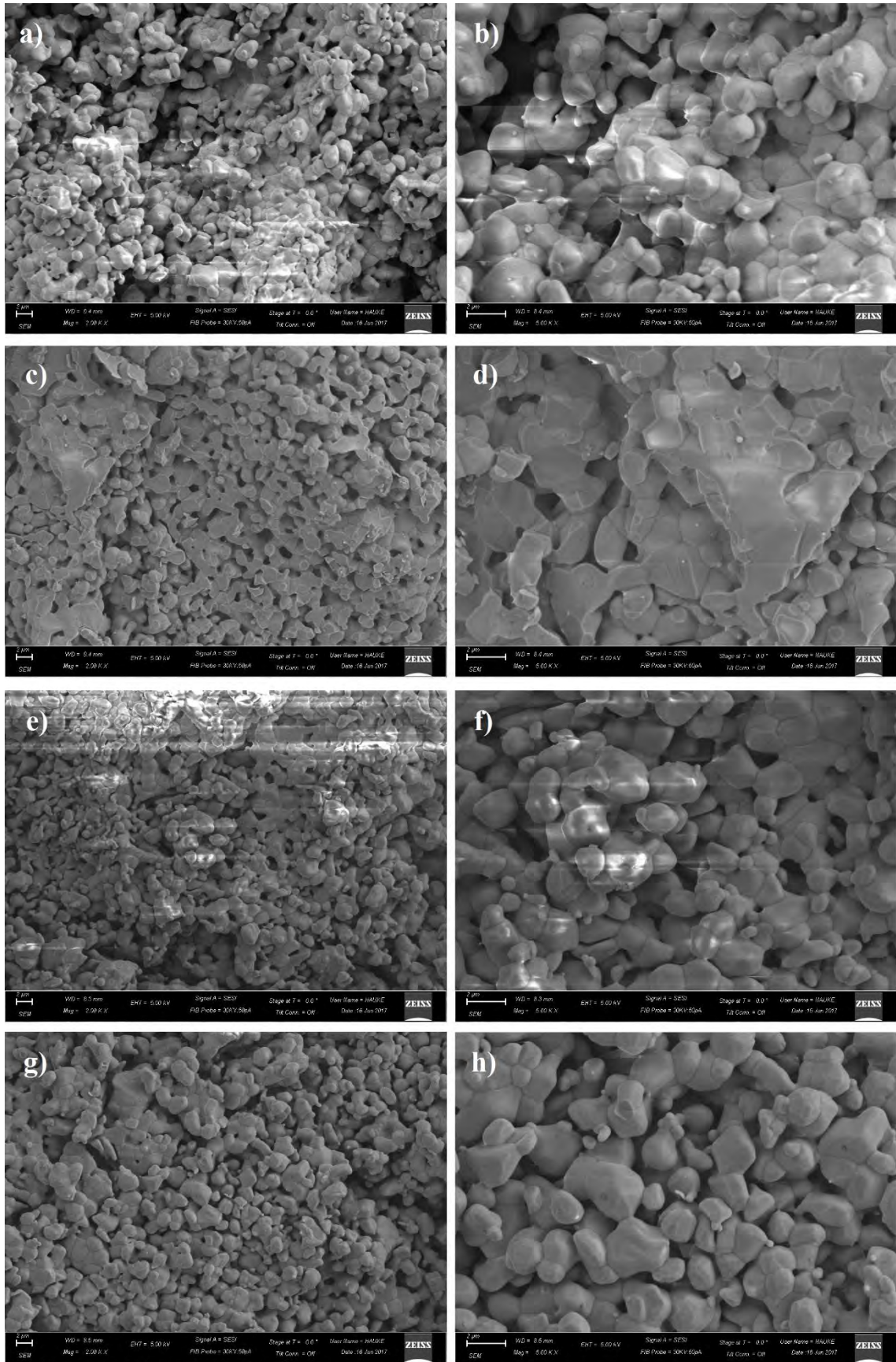
Figure 30: SEM micrographs for HAp targets sintered with 72 MPa and 1200 °C: a) & b) 2h, PEG+PVA; c) & d) 4h, PEG+PVA; e) & f) 2h, H_2O; g) & h) 4h, H_2O. Magnification: left images at 2.00 kX and right images at 5.00 kX. SEM images were taken after laser cutting.

The SEM evaluation reveals a grainy morphology at the surface. The grains boundaries are surrounded by several pores in the vicinity, as shown in the low magnification images. Furthermore, it can be seen in the targets fabricated with PEG+PVA that the grains look bigger and expanded. Smaller grains absorb thermal energy and fuse together to form bigger grains; therefore, the grain boundaries tend to disappear, making the targets denser. This confirm the results obtained for densification and linear shrinkage.

After increasing the magnification of the SEM images, the near-spherical agglomerates could clearly be seen. These irregular agglomerates were mainly composed by Ca, P and O as confirmed by the EDX analysis, as shown in **Figure 31**.
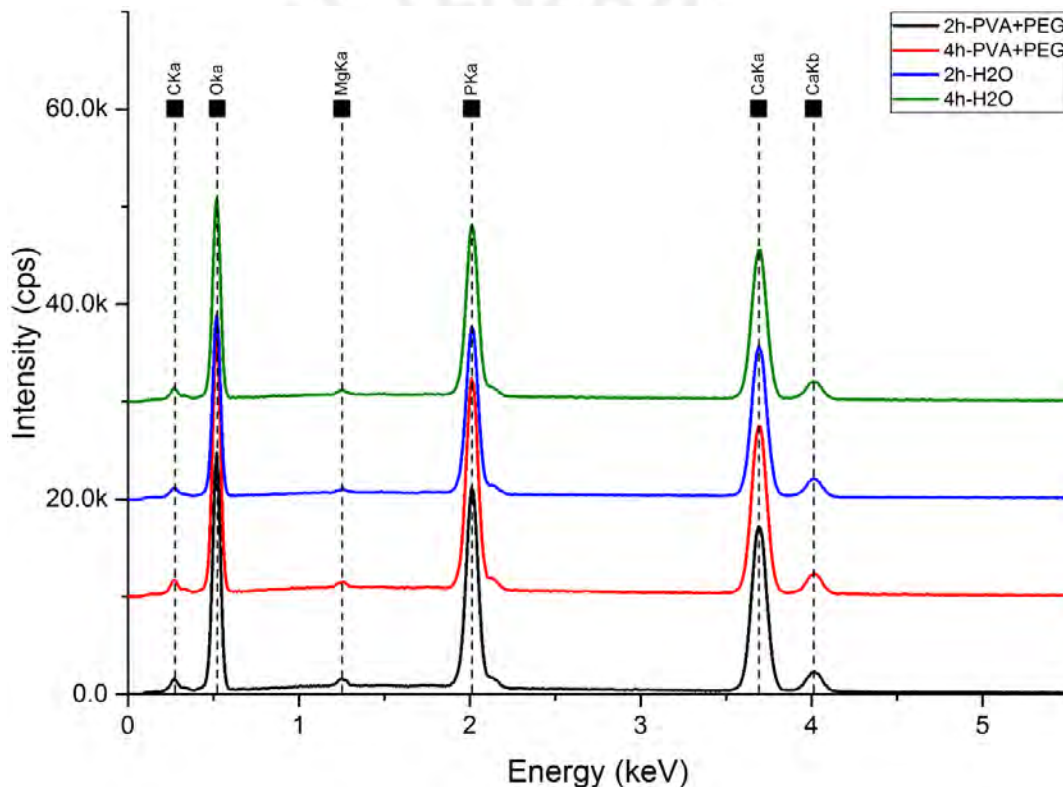
Figure 31: EDX spectrum for HAp sintered targets with 72 MPa at 1200 °C (2h, 4h / H_2O, PEG+PVA).

The **Table 13** and **Table 14** show the chemical composition and ratios of the targets fabricated with PEG+PVA and H_2O, respectively. It can be seen that the Ca/P ratio is lower than the theoretical for the target sintered at 1200 °C for 4h with additives (PVA+PEG) and higher in the other cases. In all the cases, the Ca/P ratio is higher than the HAp powders.

Table 13: Composition of HAp sintered targets with 72 MPa at 1200 °C (2h, 4h / PEG+PVA).

Element (At%)	2h, PEG+PVA	Error (%)	4h, PEG+PVA	Error (%)
C	5.36	1.27	5.55	1.20
O	48.47	0.31	50.05	0.29
Mg	0.35	4.54	0.30	4.94
P	16.92	0.27	16.71	0.26
Ca	28.90	0.26	27.39	0.26
Ratio				
Ca/P	1.708	0.375	1.639	0.368
O/Ca	1.677	0.405	1.827	0.389
O/P	2.865	0.411	2.995	0.389

Table 14: Composition of HAp sintered targets with 72 MPa at 1200 °C (2h, 4h / H_2O).

Element (At%)	2h, H_2O	Error (%)	4h, H_2O	Error (%)
C	4.82	1.49	5.23	1.39
O	46.83	0.36	48.3	0.34
Mg	0.00	0.00	0.04	45.63
P	16.86	0.30	16.58	0.29
Ca	31.49	0.28	29.86	0.28
Ratio				
Ca/P	1.868	0.410	1.801	0.403
O/Ca	1.487	0.456	1.618	0.440
O/P	2.778	0.469	2.913	0.447

As suggested by Pattanayak, D.K. et al. [144], this results indicated that at higher sintering temperature, the Ca/P ratios increases possibly due to a loss of phosphorous, which react simultaneously with oxygen.

At higher temperatures (1100 – 1400 °C) further decomposition may occur according to the reaction presented in **Equation 9** [145]. The extent of the reaction is very much dependent on the initial stoichiometry of the HAp [146]. Calcium-deficient hydroxyapatite (CDHA) shows high degradation tendency, while in case of stoichiometric HAp some loss of OH⁻ groups takes place [146]. Phosphorus pentoxide (P_2O_5), is the responsible for losing P and also O, as shown in **Equation 10** [145].

$$Ca_{10}(PO_4)_6(OH)_2 \longrightarrow 3\beta\text{-TCP} + Ca_4(PO_4)_2O + H_2O \qquad \textbf{Equation 9}$$

$$Ca_4(PO_4)_2O \longrightarrow 4CaO + P_2O_5 \uparrow \qquad \textbf{Equation 10}$$
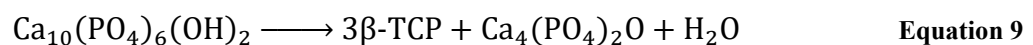
In addition, the Ca/P ratio is reduced when increasing the time from 2h to 4h at 1200 °C in both cases, as shown in **Figure 32**, which means that more phosphorous is diffusing out of the sintered target as the time increases.
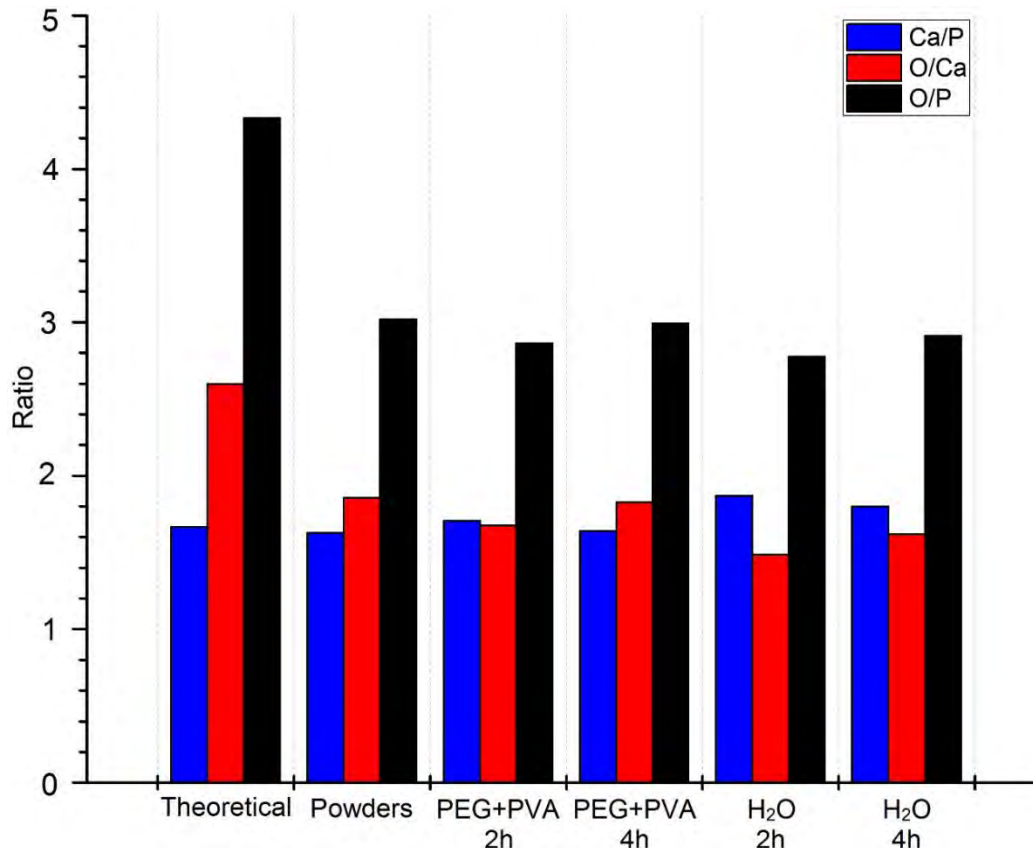
Figure 32: Comparison in ratios of the HAp targets with 72 MPa at 1200 °C (2h, 4h / H_2O, PEG+PVA). Theoretical and powder ratios were added for a better view.

From these results, the target with 72 MPa at 1200 °C (4h / PEG+PVA) has been chosen to fabricate the films with the ion beam sputter process, because:

- According to XRD results, its structure is the most similar to that for HAp.
- It is the target with the highest sintered density.
- The ratios are very similar to the starting powders.

4.2 HAp thin films deposited by RF-magnetron sputtering

After the deposition, the samples were annealed in order to increase de crystallinity. The annealed was carried out in air atmosphere for 2h using a Carbolite CWF 11/13 laboratory chamber furnace with 4 °C/min at 400, 600 and 800°C.

4.2.1 X-ray diffraction

XRD pattern of the films as-deposited and annealed are shown in **Figure 33**. It can be seen that at annealing temperatures lower than 600 °C the patterns only show the substrate. The peaks are in accordance to the hexagonal titanium given by the standard ICDD PDF #89-4405, with lattice dimensions of $a_0 = 0.295$ nm and $c_0 = 0.468$ nm.

The titanium peaks are shifted because to the substrate is Ti–6Al–4V, and the inclusion of these elements tends to deform the structure. At 800 °C the formation of tetragonal rutile (TiO_2) is observed, with lattice dimensions of $a_0 = 0.459$ nm and $c_0 = 0.296$ nm in accordance to the standard ICDD PDF #21-2176. No HAp peaks can be seen, which means an amorphous structure of the films or a possible reaction and loss of P and Ca.
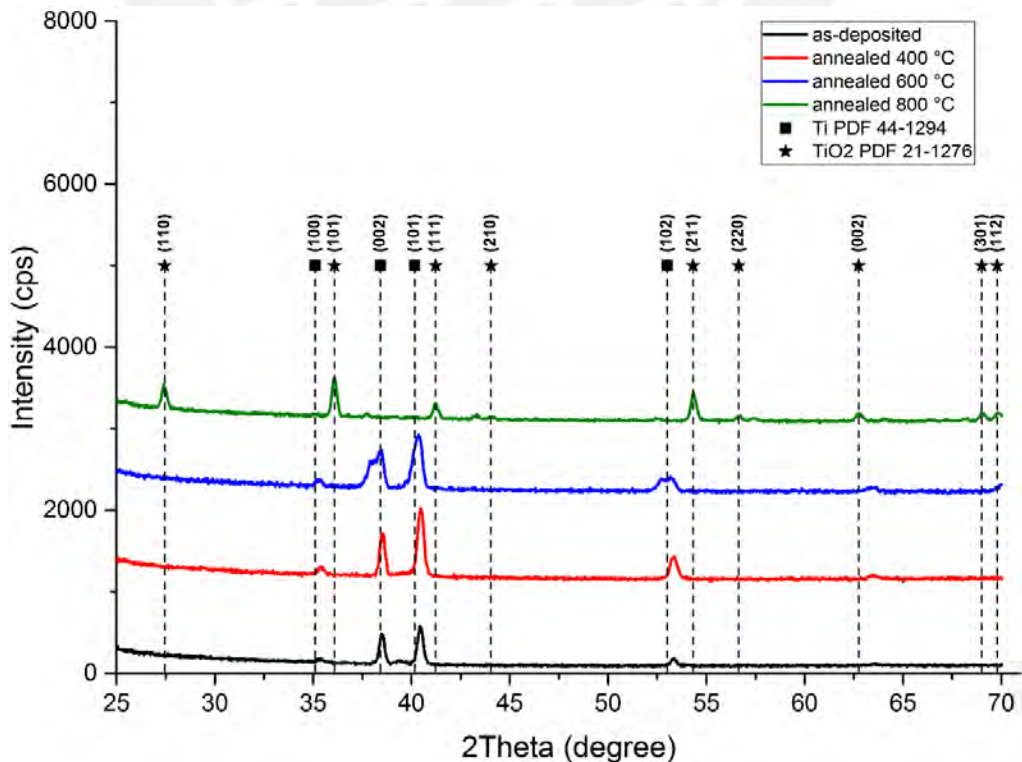
Figure 33: XRD of the films fabricated with the high purity HAp target using the RF-magnetron sputtering.

4.2.2 Scanning electron microscopy and energy dispersive X-ray spectroscopy

The **Figure 34a** and **Figure 34b** show the morphology of the as-deposited films. An irregular topography formed by a peculiar network of pits at the micro-scale level can be seen, possibly due to the previous acid pickling.

The **Figure 34c** and **Figure 34d** show the morphology of the films annealed at 800 °C for 2h in air atmosphere. It can be seen a more uniform topography formed by a dispersion of needle-like crystals, with length of 1.32 ± 0.24 μm.
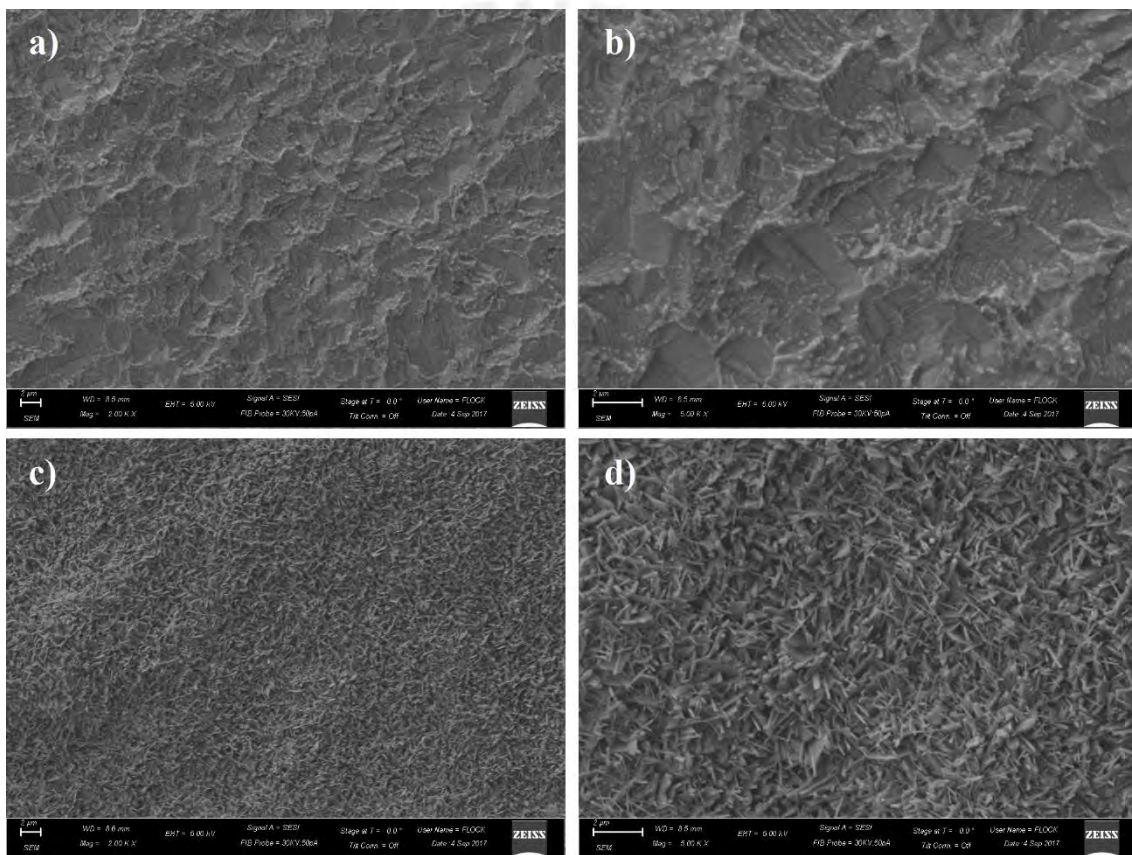
Figure 34: SEM micrographs of the films fabricated with the high purity HAp target using the RF-magnetron sputtering: a) & b) as-deposited; c) & d) annealed at 800 °C for 2h in air atmosphere. Magnification: left images at 2.00 kX and right images at 5.00 kX.

The chemical composition of both films is shown in **Table 15**. The high contents of Al and Ti is due to the acceleration voltage (ETH = 10 keV) used. High ETH results in most primary electrons traveling deeper within the sample, making it possible to detect the signal from the substrate.

Table 15: Composition of the films fabricated with the high purity HAp target using the RF-magnetron sputtering.

Element (At%)	As-deposited	Annealed 800 °C
C	9.30	2.85
O	32.66	55.10
Mg	0.28	0.33
Al	5.83	33.02
P	0.64	0.07
Ca	3.67	0.35
Ti	47.63	8.28
Ratio		
Ca/P	5.734	0.500
O/Ca	8..899	157.428
O/P	51.031	787.142

There is a high increase in the oxygen content, probably due to the oxygen of the environment was taken during the annealing process. As summarized by Kofstad, P. [147], at and below 1200°C, in air or oxygen at atmospheric pressure, the oxidation of titanium involves a simultaneous dissolution of oxygen in the metal and oxide scale formation (generally TiO_2).

In addition, the Ca/P ratio decrease with increasing the temperature. As stated by Berezhnaya, A.Yu. et al. [148], the Ca/P ratio increase with the annealing temperature (T), due to the loss of P by chemical reaction:

$$Ca_{10}(PO_4)_6(OH)_2 + Ti \xrightarrow{T} Ca_k P_l O_m H_n + TiO_2 \qquad \textbf{Equation 11}$$

$$Ca_k P_l O_m H_n \xrightarrow{T} P_2O_5 \uparrow + H_2O \uparrow \qquad \textbf{Equation 12}$$

$$CaO + TiO_2 \xrightarrow{T} CaTiO_3 \qquad \textbf{Equation 13}$$
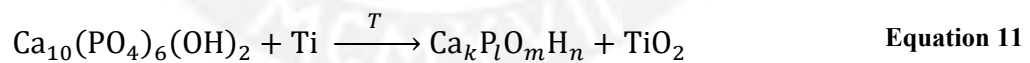
Where $Ca_k P_l O_m H_n$ stands for various compounds of Ca and P [148]. As referred by Ooi, C.Y. et al. [149], it is unclear the decline in the Ca/P ratio between 400 and 1000 °C. It can be suggested that possibly that Ca diffusion is activated in the titanium substrate at this temperature range. Further investigations of diffusion of Ca on Ti must be conducted.

4.2.3 Hardness

The **Figure 35** shows the variation of hardness with the annealing temperature. The pure Ti–6Al–4V substrates have a hardness of ~1750 N/mm^2. The as-deposited films are composed of amorphous calcium phosphate phase and have a hardness ~2400 N/mm^2, which is lower than the hardness obtained of amorphous HAp (~4400 N/mm^2) and a single HAp crystal (~7060 N/mm^2) [150].

The increment in hardness with the annealing temperature is correlated to the morphology shown in **Figure 34**. The annealed films exhibits a hardness of ~2500 N/mm^2 at 400 °C, ~2900 N/mm^2 at 600 °C and ~3500 N/mm^2 at 800 °C, which is still lower compared to amorphous HAp or single HAp crystal.

The hardness increases with the annealing temperature. The sintering conditions selected (temperature range between 400 °C and 800 °C and air atmosphere) allowed the formation of TiO$_2$, which is thermodynamically more stable. In addition, this oxide layer is confirmed to be crystalline by XRD analysis, therefore it is understandable the higher value of hardness at 800 °C.
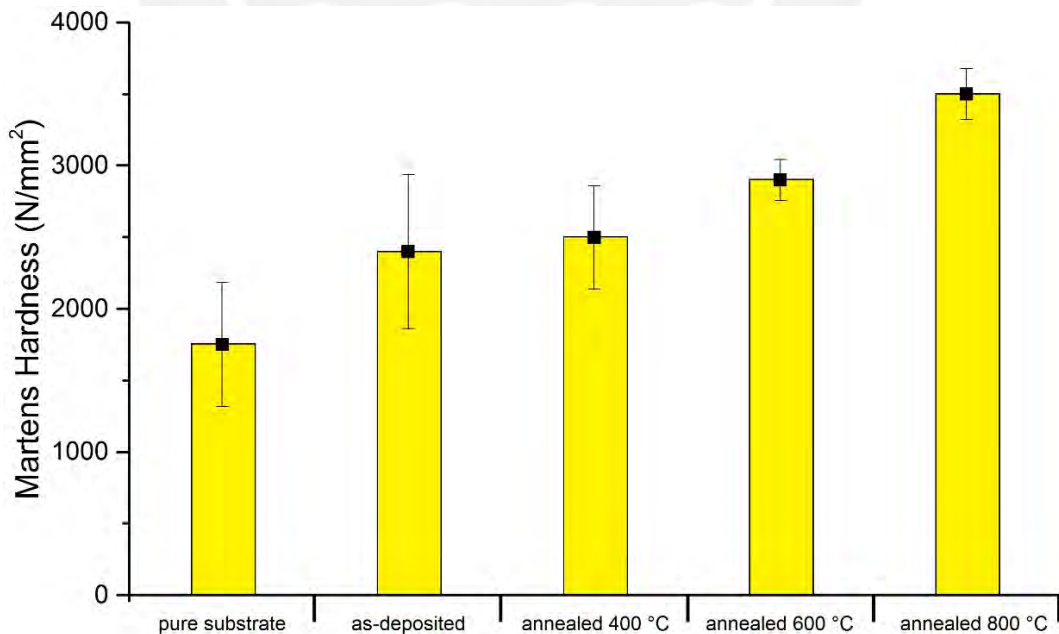
Figure 35: Hardness results of the films fabricated with the high purity HAp target using the RF-magnetron sputtering.

4.2.4 Roughness

The **Figure 36** shows the variation of surface roughness (R_a) with the annealing temperature. The pure Ti–6Al–4V substrates have a roughness of ~1.117 μm. The as-deposited thin film have a roughness ~1.153 μm. At temperatures of 400 ºC and 600 ºC the roughness was increased (~1.300 μm and ~1.537 μm respectively) and decreased to ~0.783 μm at 800 ºC. It is known that the variation of surface roughness in a thermal treatment is associated to the grain growth and the phase transformation [151].

The grain growth describes the increase in the average grain size, in this case, of the film [89]. At high temperatures, the grain boundaries move faster by diffusion of atoms (or ions) from one side of the boundary to the other, causing the growth of one grain at the expense of its neighbor and reducing the roughness [89].

As summarized by Surmeneva, M.A. et al. [152], the surface topography for HAp thin films in the range of $R_a = 0.32$–0.80 μm are suitable for the adhesion and proliferation of osteoblasts.
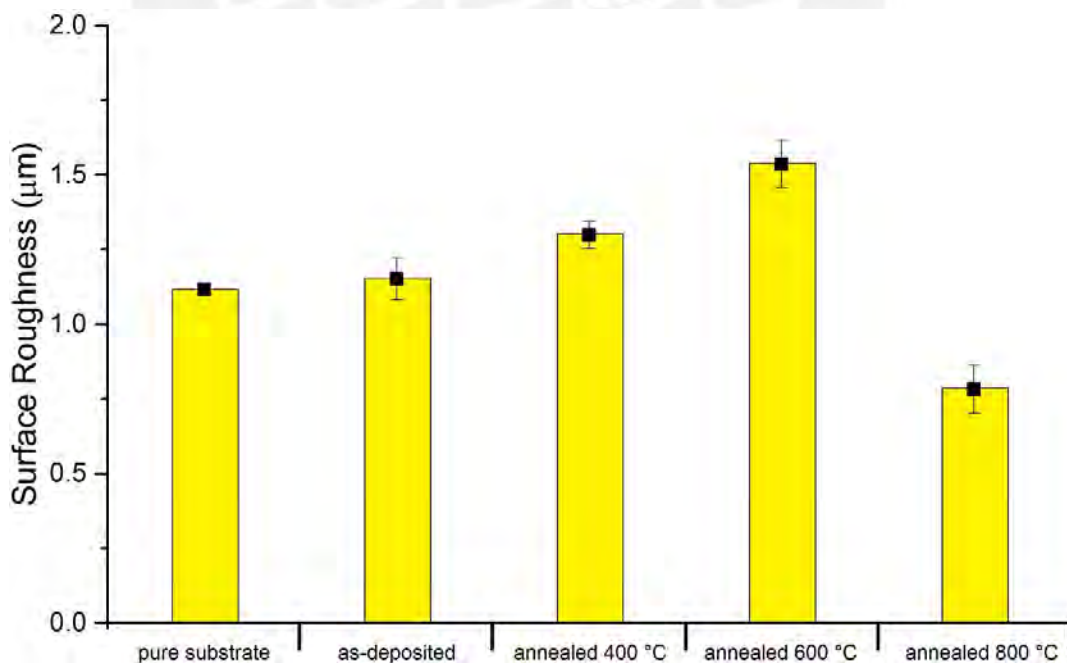
Figure 36: Surface roughness vs. annealing temperature of the films fabricated with the high purity HAp target using the RF-magnetron sputtering.

4.3 HAp thin films deposited by ion beam sputtering

After the deposition, the samples were annealed in order to increase de crystallinity. The annealed was carried out in air atmosphere for 2h using a Carbolite CWF 11/13 laboratory chamber furnace with 4 °C/min at 600 and 800°C.

4.3.1 X-ray diffraction

XRD pattern of the films as-deposited and annealed are shown in **Figure 37**. The XRD measurement of the as-deposited film shows only the peaks of the hexagonal titanium given by the standard ICDD PDF #44-1294 of the substrate, with lattice dimensions of $a_0 = 0.295$ nm and $c_0 = 0.468$ nm, which means that the film is amorphous. At 600 °C a transition from titanium to rutile can be observed. At 800 °C can be observed: Small peaks of monoclinic hydroxyapatite, with lattice dimensions of $a_0 = 0.943$ nm, $b_0 = 1.886$ nm, $c_0 = 0.687$ nm (standard ICDD PDF #89-4405); tetragonal rutile (TiO$_2$), with lattice dimensions of $a_0 = 0.459$ nm and $c_0 = 0.296$ nm (standard ICDD PDF #21-2176) and small peaks of orthorhombic CaTiO$_3$, with lattice dimensions of $a_0 = 0.5442$ nm, $b_0 = 0.764$ nm, $c_0 = 0.538$ nm (standard ICDD PDF #42-0423).
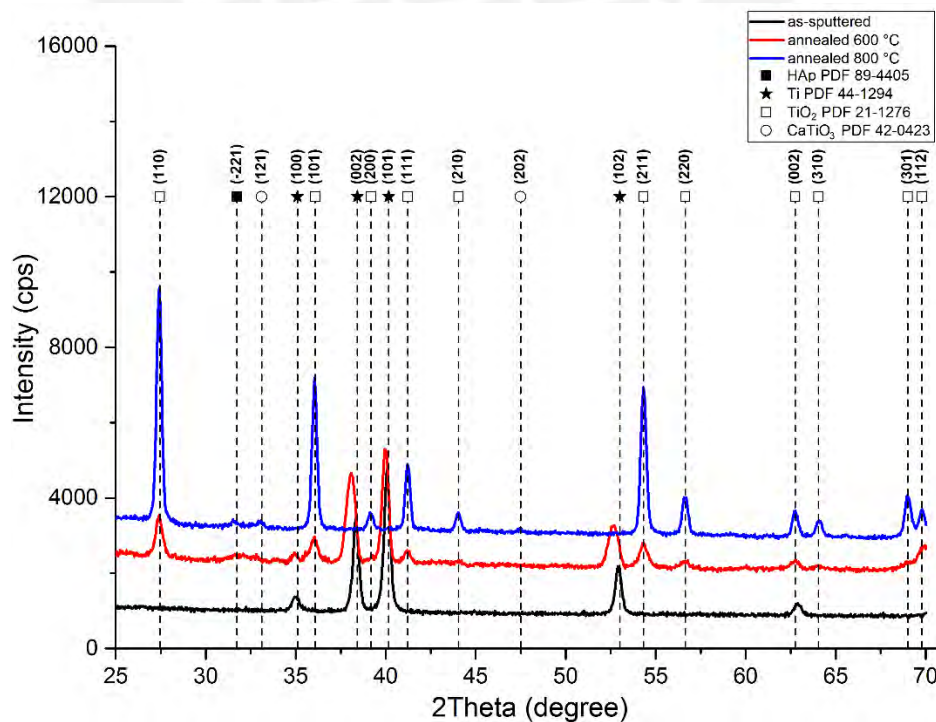
Figure 37: XRD of the films fabricated with the HAp target with 72 MPa at 1200 °C (4h / PEG+PVA) using the PECS.

4.3.2 Scanning electron microscopy

The **Figure 38a** and **Figure 38b** show the morphology of the as-deposited films. It can be seen a rough and porous topography. If these shapes can be appreciated, it means that the thickness of the film is not thick enough.

The **Figure 38c** and **Figure 38d** show the morphology of the films annealed at 600 °C for 2h in air atmosphere. The rough and porous topography is still observed, but there is an important difference, the formation of nanocrystals with length of 0.75 ± 0.16 µm.
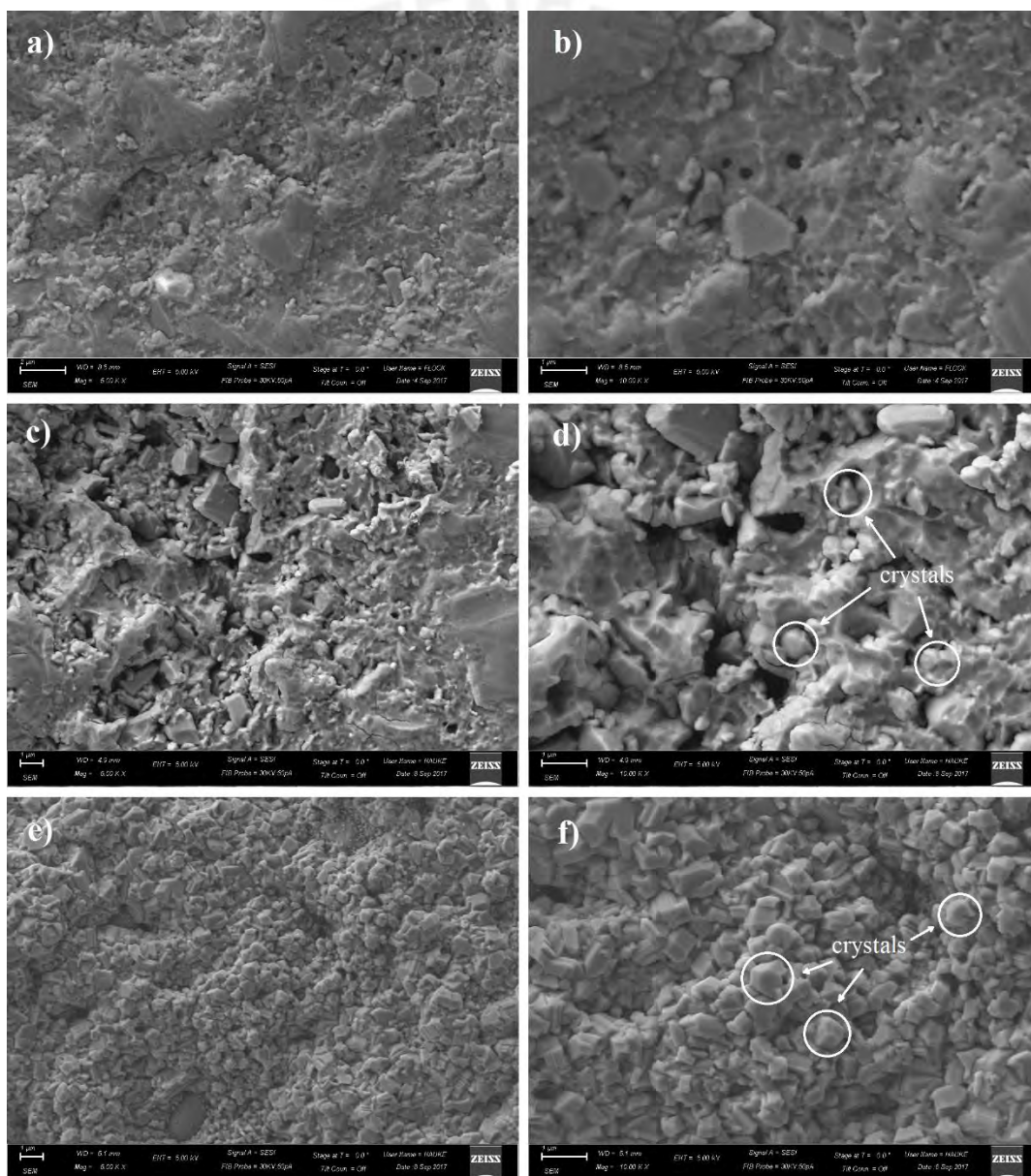
Figure 38: SEM micrographs of the films fabricated with the HAp target with 72 MPa at 1200 °C (4h / PEG+PVA) using the PECS: a) & b) as-deposited; c) & d) annealed at 600 °C; e) & f) annealed at 800 °C for 2h in air atmosphere. Magnification: left images at 5.00 kX and right images at 10.00 kX.

The **Figure 38e** and **Figure 38f** show the morphology of the films annealed at 800 °C for 2h in air atmosphere. The topography is more uniform and it can be observed several nanocrystals with length of 0.82 ± 0.14 μm.

The chemical composition of both films is shown in **Table 16**. There is an important amount of different elements detected with the EDX, due to contamination of the samples inside the chamber during the sputter process. The PECS equipment is used for etching silicon samples, and probably the steel target holder was sputtered during the process, which can explain the contamination. In addition, an increase in the oxygen content was detected, probably due to the oxygen of the environment was taken during the annealing process.

It can be observed that the Ca/P ratio decreases with increasing the temperature. As mentioned before, this can suggest the loss of a little amount of P by chemical reaction and a loss of Ca probably due to diffusion on Ti substrate. In addition, at 800 °C, the presence of HAp and $CaTiO_3$ is observed from **Figure 37**, which suggests that the Ca is shared by both species. The amount of Ti is higher than the same obtained for the samples fabricated with RF-magnetron sputtering. This means that more Ti is reacting with the O from the environment due to its high activity at elevated temperatures [147].

Table 16: Composition of the films fabricated with the HAp target with 72 MPa at 1200 °C (4h / PEG+PVA) using the PECS.

Element (at%)	As-deposited	Annealed 600 °C	Annealed 800 °C
C	5.98	3.24	2.51
O	52.22	58.77	63.55
Fe	2.46	2.09	0.58
Ni	0.44	0.39	0.09
Mg	0.00	0.19	0.13
Al	0.57	0.73	0.38
Si	3.35	4.04	0.28
P	4.15	4.49	0.74
Ca	12.80	13.16	1.36
Ti	17.07	11.82	30.21
Cr	0.95	1.08	0.17
Ratio			
Ca/P	3.084	2.931	1.838
O/Ca	4.079	4.466	46.728
O/P	12.583	13.089	85.878

4.3.3 Hardness

In this case, the evolution of films hardness is more noticeable. The **Figure 39** shows the variation of hardness with the annealing temperature. The increment in hardness with the temperature is correlated with the morphology of the films, shown in **Figure 38**. The Martens hardness of the substrates was ~3300 N/mm^2.

It can be seen that at 800 °C there is a considerable increase in hardness (~12500 N/mm^2) probably due to the formation of TiO$_2$ nanocrystals. This hardness value is close to the theoretical hardness value of TiO$_2$ (~15000 N/mm^2) [153]. In addition, this oxide layer is confirmed to be crystalline by XRD analysis, therefore it is understandable the higher value of hardness at 800 °C.
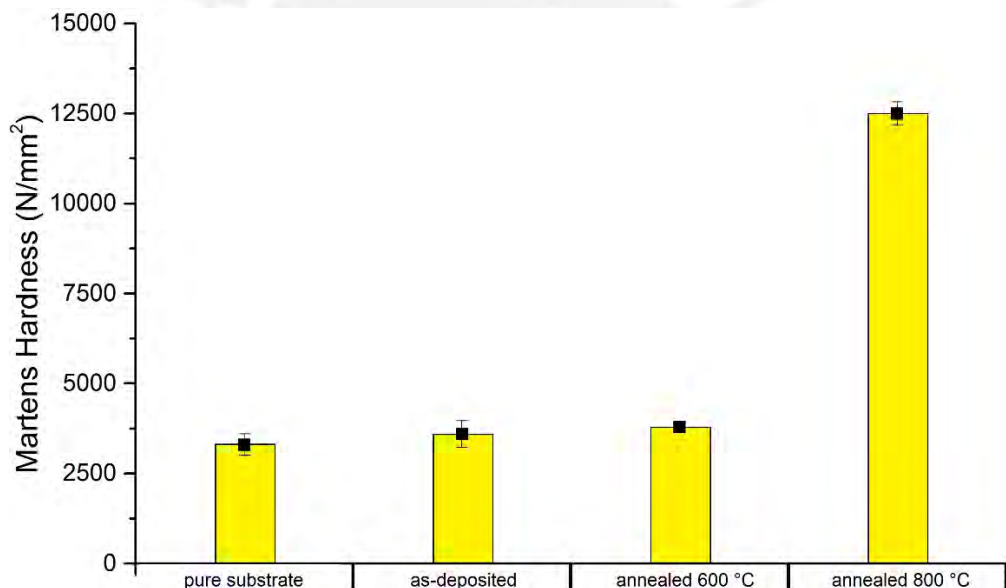
Figure 39: Hardness results of the films fabricated with the HAp target with 72 MPa at 1200 °C (4h / PEG+PVA) using the PECS.

4.3.3 Roughness

The **Figure 40** shows the variation of surface roughness (R$_a$) with the annealing temperature. The pure titanium substrates exhibit a roughness of ~0.630 μm. The as-deposited thin film has a roughness ~1.123 μm. At temperatures of 600 ºC and 800 ºC the roughness decreases to ~1.033 μm and ~0.800 μm respectively. As stated before, this is due to the grain growth and the phase transformation during heat treatment.
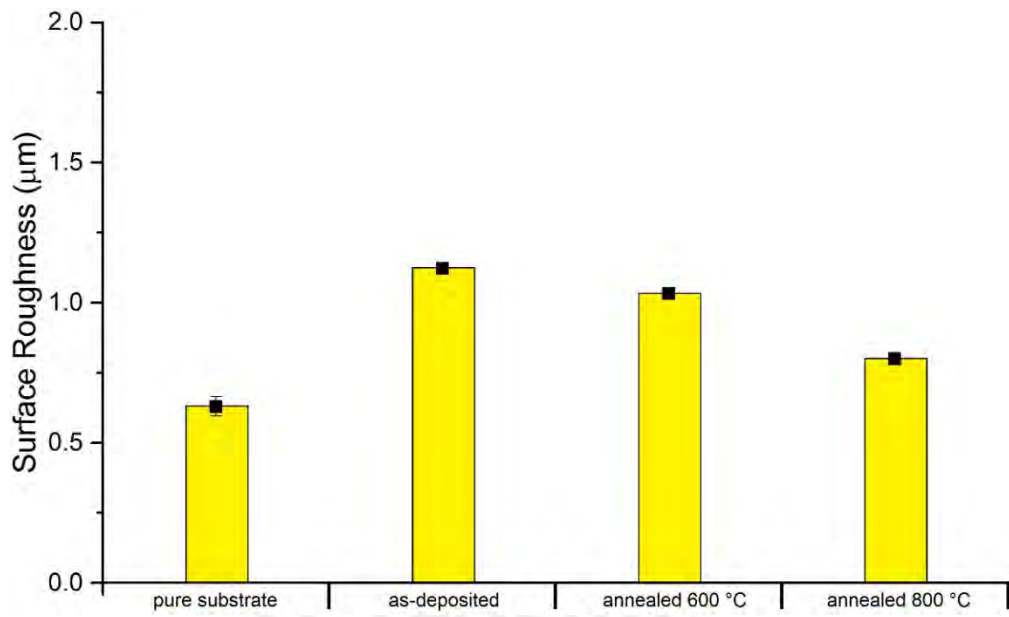
Figure 40: Surface roughness vs. annealing temperature of the films fabricated with the HAp target with 72 MPa at 1200 °C (4h / PEG+PVA) using the PECS.
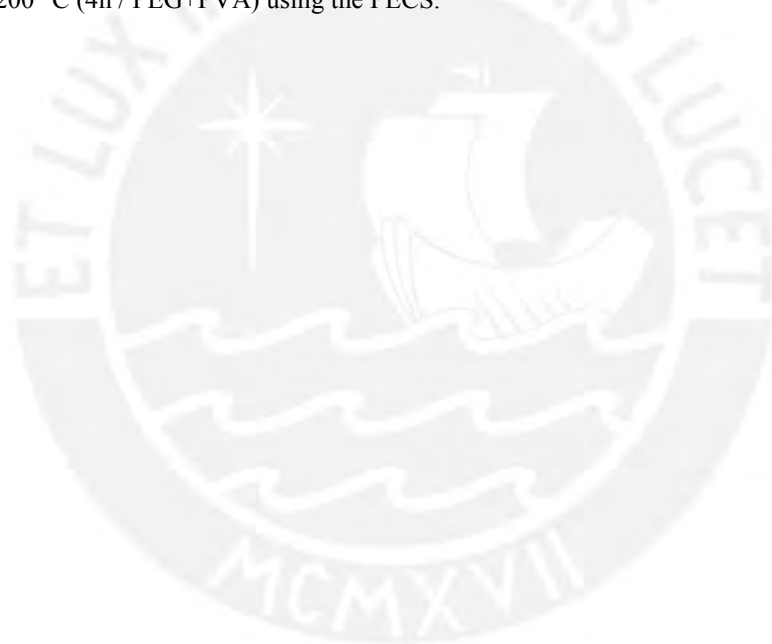
5. Conclusions

Hydroxyapatite (HAp) is considered as biomaterial of importance in the field of biology and medicine due to their abundance in the living organism. In this work, HAp thin films were fabricated using two different sputter techniques: Radio frequency (RF) magnetron sputtering and ion beam sputtering (IBS). The films were grown on Ti–6Al–4V and pure titanium substrates respectively. Only the target used in TU-Ilmenau was fabricated with HAp powders in air atmosphere at different conditions: 3.5g, 5g and 15g and 24 MPa at 1200 °C (4h / H_2O); 72 MPa at 1200 °C (2h, 4h / PEG+PVA, H_2O); 72 MPa at 1200 °C (2h, 4h / PEG+PVA, H_2O). The pressures were applied before sintering. The target used in PUCP-Lima was a commercially bought one.

The results for the sintered HAp discs shows that the fabricated target for the IBS process using 72 MPa before sintering, at 1200 °C for 4h using a mixing of PEG and PVA in aqueous solution presents structural and chemical characteristics very similar to the powders, with a sintered density of 1.78 g/cm^3, which represent the 56% of the theoretical density (3.156 g/cm^3) of HAp. Therefore, the addition of PEG and PVA promotes the densification mechanisms.

The as-deposited thin films obtained with both techniques were amorphous. In the case of the films fabricated with RF-magnetron sputtering, the crystallinity of HAp was not improved using annealing at 400, 600 and 800 °C. In the case of the films fabricated with IBS, the XRD results shows the formation of crystalline HAp and $CaTiO_3$. In both cases, the evolution in crystallinity of the titanium oxide formed due to the high-temperature oxidation is appreciated.

The SEM analysis shows a rough topography in the as-deposited, annealed at 400 and 600 °C (RF-magnetron sputtering) and 600 °C (IBS). For the samples annealed at 800 °C, an uniform topography formed by a dispersion of needle-like crystals in the case of RF-magnetron sputtering samples and nanocrystals in the case of IBS samples can be seen.

In both cases the EDX measurements show a decrease in Ca/P ratio with increasing the temperature, probably due the loss of a little amount of P by chemical reaction and a loss

of Ca probably due to diffusion on Ti substrate. For the samples fabricated with IBS and annealed at 800 °C, the Ca/P ratio was 1.838 and the presence of HAp and $CaTiO_3$ was confirmed by XRD. It can be suggested that the Ca is shared by both species, in which case the Ca/P ratio of the HAp formed can be more close to the theoretical.

In addition, the presence of Ti and O is observed, which means that this heat treatment was not properly controlled. The high content of oxygen can suggest a chemical reaction of substrates with the environment obtaining TiO_2 as oxidation product. Therefore, annealing treatment in inert atmospheres as N_2 or Ar must be recommended.

Hardness results shows that the hardness increases with the annealing temperature in both cases, due to the formation of titanium oxide crystals.

The roughness for the fabricated films with RF-magnetron sputtering increases at 600 °C, then its decrease at 800 °C. The roughness for the fabricated films with IBS decreases with increasing the annealing temperature. In both cases, due to the formation of crystals.

Future work should focus on performing the annealing treatment in an inert atmosphere such as N_2 or Ar in order to improve the crystallinity of the films. A proper heat treatment study through the control of annealing temperature must be performed in order to produce crystalline HAp films. In addition, the relation between thickness and crystal growth must be determinate. Thus, the major goal in HAp coating research must be the improvement of the crystallinity

In order to fulfill the biological requirements, culture bone cell test must be performed. Roughness has an important influence in the bone-implant interface shear strength. Therefore, mechanical shear test could be suggested for a better correlation with the obtained properties.

References

[1] Raynaud, S.; Champion, E.; Bernache-Assollant, D.; Thomas, P. *Calcium phosphate apatites with variable Ca/P atomic ratio I. Synthesis, characterisation and thermal stability of powders*. Biomaterials 2002; **23**: 1065 – 1072.

[2] Maté-Sánchez de Val, J.E.; Mazón, P.; Calvo Guirado, J.L.; Delgado Ruiz, R.A.; Ramírez Fernández, M.P.; Negri, B.; Abboud, M.; De Aza, P.N. *Comparison of three hydroxyapatite/b-tricalcium phosphate/collagen ceramic scaffolds: An in vivo study*. Journal of Biomedical Materials Research A 2014; **102**(4): 1037 – 1046.

[3] Sadat-Shojai, M.; Khorasani, M.-T.; Dinpanah-Khoshdargi, E.; Jamshidi, A. *Synthesis methods for nanosized hydroxyapatite in diverse structures*. Acta Biomatererialia 2013, http://dx.doi.org/10.1016/j.actbio.2013.04.012.

[4] Wang, L. & and Nancollas, G.H. *Calcium Orthophosphates: Crystallization and Dissolution*. Chemical Reviews 2008; **108**(11), 4628 – 4669.

[5] Vallet-Regí, M. & González-Calbet, J.M. *Calcium phosphates as substitution of bone tissues*. Progress in Solid State Chemistry 2004; **32**: 1 – 31.

[6] Dorozhkin, S.V. *Calcium orthophosphates*. Biomatter 2014; **1**(2): 121 – 164.

[7] Ma, G. & Liu, X.Y. *Hydroxyapatite: moal or Monoclinic?*. Crystal Growth & Design 2009; **9**(7): 2991 – 2994.

[8] Reyes-Gasga, J.; Martínez-Piñeiro, E.L.; Brès, E.F. *Crystallographic structure of human tooth enamel by electron microscopy and x-ray diffraction: hexagonal or monoclinic?*. Journal of Microscopy 2012; **248**(1): 102 – 109.

[9] Mucalo, M. (2015). *Hydroxyapatite (HAp) for Biomedical Applications*. Woodhead Publishing Series in Biomaterials: Number 95.

[10] Hench, L.L. *Bioceramics: From Concept to Clinic*. Journal of the American Ceramic Society 1991; **74**(7): 1487 – 1510.

[11] McPhersont, R.; Gane, N.; Bastow, T.J. *Structural characterization of plasma-sprayed Hydroxylapatite coatings*. Journal of Materials Science: Materials in Medicine 1995; **6**: 327 – 334.

[12] Binner, J.G.P.; Reichert, J. *Processing of hydroxyapatite ceramic foams*. Journal of Materials Science 1996; **31**: 5717 – 5723.

[13] Bernache-Assollanta, D.; Ababoua, A.; Championa, E.; Heughebaert, M. *Sintering of calcium phosphate hydroxyapatite $Ca_{10}(PO_4)_6(OH)_2$ I. Calcination and particle growth*. Journal of the European Ceramic Society 2003; **23**: 229 – 241.

[14] Pontiera, C.; Viana, M.; Champion, E.; Bernache-Assollantb, D.; Chulia, D. *About the use of stoichiometric hydroxyapatite in compression incidence of manufacturing process on compressibility*. European Journal of Pharmaceutics and Biopharmaceutics 2001; **51**: 249 – 257.

[15] Lo, W.J.; Grant, D.M.; Ball, M.D.; Welsh, B.S.; Howdle, S.M.; Antonov, E.N.; Bagratashvili, V.N.; Popov, V.K. *Physical, chemical, and biological characterization of pulsed laser deposited and plasma sputtered hydroxyapatite thin films on titanium alloy*. Journal of Biomedical Materials Research Part A 2000; **50**(4): 536 – 545.

[16] Kannan, S.; Vieira, S.I.; Olhero, S.M.; Torres, P.M.C.; Pina, S.; da Cruz e Silva, O.A.B.; Ferreira, J.M.F. *Synthesis, mechanical and biological characterization of ionic doped carbonated hydroxyapatite/β-tricalcium phosphate mixtures*. Acta Biomaterialia 2011; **7**: 1835 – 1843.

[17] Olszta, M.J.; Cheng, X.; Jee, S.S.; Kumar, R.; Kim, Y.-Y.; Kaufman, M.J.; Douglas, E.P.; Gower, L.B. *Bone structure and formation: A new perspective*. Materials Science and Engineering R 2007; **58**: 77 – 116.

[18] Xue, W.; Tao, S.; Liu, X.; Zheng, X.B.; Ding, C. *In vivo evaluation of plasma sprayed hydroxyapatite coatings having different crystallinity*. Biomaterials 2004; **25**: 415 – 421.

[19] Filiaggi, M.J.; Coombs, N.A.; Pilliar, R.M. *Characterization of the interface in the plasma-sprayed HA coating/Ti-GAl-4V implant system*. Journal of Biomedical Materials Research 1991; **25**: 1211 – 1229.

[20] Pálka, V.; Poštrková, E.; Koerten, H.K. Some characteristics of hydroxylapatite powder particles after plasma spraying. Biomaterials 1998; **19**: 1763 – 1772.

[21] Ellies, L.G.; Nelson, D.G.A.; Featherstone, J.D.B. *Crystallographic changes in calcium phosphates during plasma-spraying*. Biomaterials 1992; **13**(5): 313 – 316.

[22] Gross, K.A.; Berndt, C.C.; Herman, H. *Amorphous phase formation in plasma-sprayed hydroxyapatite coatings*. Journal of Biomedical Materials Research 1998; **39**(3): 407 – 714.

[23] Zyman, Z.; Weng, J.; Liu, X.; Zhang, X.; Ma, Z. *Amorphous phase and morphological structure of hydroxyapatite plasma coatings*. Biomaterials 1993; **14**(3): 225 – 228.

[24] Chen, J.; Wolke, J.G.C.; de Groat, K. *Microstructure and crystallinity in hydroxyapatite coatings*. Biomaterials 1994; **15**(5): 396 – 399.

[25] Ding, S.-J.; Ju, C.-P.; Chern Lin, J.-H. *Characterization of hydroxyapatite and titanium coatings sputtered on Ti-6Al-4V substrate*. Journal of Biomedical Materials Research 1999; **44**(3):266 – 279.

[26] van Dijk, K.; Maree, C.H.M.; Habraken, F.H.P.M.; Verhoeven, J.; Jansen, J.A. *Study of the influence of oxygen on the composition of thin films obtained by r.f. sputtering from a $Ca_5(PO_4)_3OH$ target*. Thin Solid Films 1997; **304**: 191 – 195.

[27] Jansen, J.A.; Wolke, J.G.; Swann, S.; Van der Waerden, J.P.; de Groot, K. *Application of magnetron sputtering for producing ceramic coatings on implant materials*. Clinical Oral Implants Research 1993; **4**(1): 28 – 34.

[28] Van Dijk, K.; Schaeken, H.G.; Maree, CH.M.; Verhoeven, J.; Wolke, J.C.G.; Habraken, F.H.P.M.; Jansen, J.A. *Influence of Ar pressure on r.f. magnetron-sputtered $Ca_5(PO_4)_3OH$ layers*. Surface and Coatings Technology 1995; **76-77**: 206 – 210.

[29] Van Dijk, K.; Schaeken, I.H.G.; Wolke, J.C.G.; Maree, C.H.M.; Habraken, F.H.P.M.; Verhoeven, J.; Jansen, J.A. *Influence of discharge power level on the properties of hydroxyapatite films deposited on Ti6Al4V with RF magnetron sputtering*. Journal of Biomedical Materials Research 1995; **29**: 269 – 276.

[30] Clèries, L.; Martínez, E.; Fernández-Pradas, J.M.; Sardin, G.; Esteve, J.; Morenza, J.L. *Mechanical properties of calcium phosphate coatings deposited by laser ablation*. Biomaterials 2000; **21**: 967 – 971.

[31] Fernández-Pradas, J.M.; Clèries, L.; Sardin, G.; Morenza, J.L. *Characterization of calcium phosphate coatings deposited by Nd:YAG laser ablation at 355 nm: influence of thickness*. Biomaterials 2002; **23**: 1989 – 1994.

[32] Manso, M.; Langlet, M.; Jiménez, C.; Martínez-Duart, J.M. *Microstructural study of aerosol-gel derived hydroxyapatite coatings*. Biomolecular Engineering 2002; **19**: 63 – 66.

[33] Liu, D.-M.; Troczynski, T.; Tseng, W.J. *Water-based sol-gel synthesis of hydroxyapatite: process development*. Biomaterials 2001; **22**: 1721 – 1730.

[34] Milella, E.; Cosentino, F.; Licciulli, A.; Massaro, C. *Preparation and characterisation of titania/hydroxyapatite composite coatings obtained by sol-gel process*. Biomaterials 2001; **22**: 1425 – 1431.

[35] Han, Y.; Xu, K.; Lu, J.; Wu, Z. *The structural characteristics and mechanical behaviors of nonstoichiometric apatite coatings sintered in air atmosphere*. Journal of Biomedical Materials Research Part A 1999; **45**(3): 198 – 203.

[36] Manso, M.; Jiménez, C.; Morant, C.; Herrero, P.; Martínez-Duart, J.M. *Electrodeposition of hydroxyapatite coatings in basic conditions*. Biomaterials 2000; **21**: 1755 – 1761.

[37] Stoch, A.; Brożek, A.; Kmita, G.; Stoch, J.; Jastrzębski, W.; Rakowska, A. *Electrophoretic coating of hydroxyapatite on titanium implants*. Journal of Molecular Structure 2001; **596**: 191 – 200.

[38] Zhang, J.M.; Lin, C.J.; Feng, Z.D.; Tian, Z.W. *Mechanistic studies of electrodeposition for bioceramic coatings of calcium phosphates by an in situ pH-microsensor technique*. Journal of Electroanalytical Chemistry 1998; **452**: 235 – 240.

[39] Kwok, C.T.; Wonga, P.K.; Cheng, F.T.; Man, H.C. *Characterization and corrosion behavior of hydroxyapatite coatings on Ti6Al4V fabricated by electrophoretic deposition*. Applied Surface Science 2009; **255**: 6736 – 6744.

[40] Massaro, C.; Baker, M.A.; Cosentino, F.; Ramires, P.A.; Klose, S.; Milella, E. *Surface and biological evaluation of hydroxyapatite-based coatings on titanium deposited by different techniques*. Journal of Biomedical Materials Research Part A 2001; **58**(6): 651 – 657.

[41] Dorozhkin, S.V. *Nanodimensional and nanocrystalline apatites and other calcium orthophosphates in biomedical engineering, biology and medicine*. Materials 2009; **2**: 1975 – 2045.

[42] Rey, C.; Combes, C.; Drouet, C.; Grossin, D. *Comprehensive Biomaterials*. In: Bioactive Ceramics: Physical Chemistry. Publisher Elsevier, pp.187 – 221.

[43] Bohner, M.; Theiss, F.; Apelt, D.; Hirsiger, W.; Houriet, R.; Rizzoli, G.; Gnose, E.; Frei, C.; Auer, J.A.; von Rechenberg, B. *Compositional changes of a dicalcium phosphate dihydrate cement after implantation in sheep*. Biomaterials 2003; **24**: 3463 – 3474.

[44] Prado da Silva, M.H.; Lima, J.H.C.; Soares, G.A.; Elias, C.N.; de Andrade, M.C.; Bestf, S.M.; Gibson, I.R. *Transformation of monetite to hydroxyapatite in bioactive coatings on titanium*. Surface and Coatings Technology 2001; **137**: 270 – 276.

[45] Theiss, F.; Apelt, D.; Branda, B.; Kutter, A.; Zlinszkya, K.; Bohner, M.; Matter, S.; Frei, C.; Auer, J.A.; von Rechenberg, B. *Biocompatibility and resorption of a brushite calcium phosphate cement*. Biomaterials 2005; **26**: 4383 – 4394.

[46] Hung, I.-M.; Shih, W.-J.; Hon, M.-H.; Wang, M.-C. *The Properties of Sintered Calcium Phosphate with [Ca]/[P] = 1.50*. International Journal of Molecular Sciences 2012; **13**: 13569 – 13586.

[47] Marchi, J.; Greil, P.; Bressiani, J.C.; Ana Bressiani, A.; Müller, F. *Influence of synthesis conditions on the characteristics of biphasic calcium phosphate powders*. International Journal of Applied Ceramic Technology 2009; **6**(1): 60 – 71.

[48] Yang, Y.; Kimc, K.-H.; Ong, J.O. *A review on calcium phosphate coatings produced using a sputtering process—an alternative to plasma spraying*. Biomaterials 2005; **26**: 327 – 337.

[49] Wang, H.; Lee, J.-K.; Moursi, A.; Lannutti, J.J. *Ca/P ratio effects on the degradation of hydroxyapatite in vitro*. Journal of Biomedical Materials Research Part A 2003; **67**(2): 599 – 608.

[50] Yamaguchi, T.; Tanaka, Y.; Ide-Ektessabi, A. *Fabrication of hydroxyapatite thin films for biomedical applications using RF magnetron sputtering*. Nuclear Instruments and Methods in Physics Research B 2006; **249**: 723 – 725.

[51] Kannan, S.; Rocha, J.H.G.; Ventura, J.M.G.; Lemos, A.F.; Ferreira, J.M.F. *Effect of Ca/P ratio of precursors on the formation of different calcium apatitic ceramics—An X-ray diffraction study*. Scripta Materialia 2005; **53**: 1259 – 1262.

[52] Tas, A.C. *Participation of calcium phosphate bone substitutes in the bone remodeling process: Influence of materials chemistry and porosity*. Key Engineering Materials 2004; **264-268**: 1969 – 1972.

[53] Markovic, M.; Fowler, B.O.; Tung, M.S. *Preparation and comprehensive characterization of a calcium hydroxyapatite reference material*. Journal of Research of the National Institute of Standards and Technology 2004; **109**(6): 553 – 568.

[54] Reyes-Gasga, J.; Martínez-Piñeiro, E.L.; Brès; É.F. *Crystallographic structure of human tooth enamel by electron microscopy and x-ray diffraction: hexagonal or monoclinic?*. Journal of Microscopy 2012; **248**(1): 102 – 109.

[55] Ikoma, T.; Yamazaki, A.; Nakamura, S.; Akao, M. *Phase transition of monoclinic hydroxyapatite*. Netsu Sokutei 1998; **25**(5): 141 – 149.

[56] Takahashi, H.; Yashima, M.; Kakihana, M.; Yoshimura, M. *A differential scanning calorimeter study of the monoclinic (P2₁/b) ↔ hexagonal (P6₃/m) reversible phase transition in hydroxyapatite*. Thermochimica Acta 2001; **371**: 53 – 56.

[57] Vallet-Regía, M.; González-Calbet, J.M. *Calcium phosphates as substitution of bone tissues*. Progress in Solid State Chemistry 2004; **32**: 1 – 31.

[58] Hu, S.; Jia, F.; Marinescu, C.; Cimpoesu, F.; Qi, Y.; Tao, Y.; Stroppa, A.; Ren, W. *Ferroelectric polarization of hydroxyapatite from density functional theory*. RSC Advances 2017; **7**: 21375 – 21379.

[59] Champion, E. Review: Sintering of CaP bioceramics. Acta Biomater 2012, http://dx.doi.org/10.1016/j.actbio.2012.11.029.

[60] Lin, K.; Chang, J.; Liu, X.; Chen, L.; Zhou, Y. *Synthesis of element-substituted hydroxyapatite with controllable morphology and chemical composition using calcium silicate as precursor*. CrystEngComm 2011; **13**: 4850 – 4855.

[61] Treboux, G.; Layrolle, P.; Kanzaki, N.; Onuma, K.; Ito, A. *Symmetry of Posner's Cluster*. Journal of the American Chemical Society 2000; **122**: 8323 – 8324.

[62] Kanzaki, N.; Treboux, G.; Onuma, K.; Tsutsumi, S.; Ito, A. *Calcium phosphate clusters*. Biomaterials 2001; **22**: 2921 – 2929.

[63] Combes, C.; Rey, C. *Amorphous calcium phosphates: Synthesis, properties and uses in biomaterials*. Acta Biomaterialia 2010; **6**: 3362 – 3378.

[64] Mullender, M. G. & Huisker, R. *Proposal for the Regulatory Mechanism of Wolff´s Law*. Journal of Orthopaedic Research 1995; **13**: 503 – 512.

[65] Ahn, A.C. & and Grodzinsky, A.J. *Relevance of collagen piezoelectricity to "Wolff's law": A critical review*. Medical Engineering & Physics 2009; **31**(7): 733 – 741.

[66] Park, J. & Lakes, R. S. *Biomaterials: An Introduction*. 3rd Edition, Springer 2007.

[67] Williams, D.F. *On the nature of biomaterials*. Biomaterials 2009; **30**: 5897 – 5909.

[68] Sykaras, N.; Iacopino, A.M.; Marker, V.A.; Triplett, R.G.; Woody, R.D. *Implant materials, designs, and surface topographies: Their effect on osseointegration. A literature review*. The International Journal of Oral & Maxillofacial Implants 2000; **15**: 675 – 690.

[69] Rack, H. J. & Long, M. *Titanium alloys in total joint replacement – a materials science perspective*. Biomaterials 1997; **19**: 1621 – 1639.

[70] Feng, B.; Chen, J.Y.; Qi, S.K.; He, L.; Zhao, J.Z.; Zhang, X.D. *Characterization of surface oxide films on titanium and bioactivity*. Journal of materials science: Materials in Medicine 2002; **13**: 457 – 464.

[71] Schwitalla, A.; Abou-Emara, M.; Spintig, T.; Lackmann, J.; Müller, W. *Biomechanical effects of elastic-modulus-graded PEEK implants*. Clinical Oral Implants Research 2015; 148987.

[72] Otani, T., Whiteside, L.A.; White, S.E.; McCarthy, D.S. *Effects of femoral component material properties on cementless fixation in total hip arthroplasty*. The Journal of Arthroplasty 1993; **8**(1): 67 – 74.

[73] Seal, S. *Functional Nanostructures: Processing, Characterization, and Applications*. Springer 2008

[74] ASTM Designation: F67 – 13. *Standard Specification for Unalloyed Titanium, for Surgical Implant Applications (UNS R50250, UNS R50400, UNS R50550, UNS R50700)*. 2013.

[75] Family R.; Solati-Hashjin, M.; Nik, S.N.; Nematid, A. *Protection of titanium metal by nanohydroxyapatite coating with zirconia and alumina second phases*. Protection of Metals and Physical Chemistry of Surfaces 2012; **48** (6): 688 – 691.

[76] Xie, X.-H.; Yu, X.-W.; Zeng, S.-X; Du, R.-L.; Hu, Y.-H.; Lu, E.-Y.; Dai, K.-R.; Tang, T.-T. *Enhanced osteointegration of orthopaedic implant gradient coating composed of bioactive glass and nanohydroxyapatite*. Journal of Materials Science: Materials in Medicine 2010; **21**: 2165 – 2173.

[77] Barkamo, S.; Andersson, M.; Currie, F.; Kjellin, P.; R Jimbo, R.; Johansson, C.B.; Stenport, V. *Enhanced bone healing around nanohydroxyapatite-coated polyetheretherketone implants: An experimental study in rabbit bone*. Journal of Biomaterials Applications 2014; **29**(5): 737 – 747.

[78] Engh, C.A.; Bobyn, J.D.; Glassman, A.H. Porous-coated hip replacement. *The factors governing bone ingrowth, stress shielding, and clinical results*. The Journal of Bone and Joint Surgery. British Volume 1987; **69**(1): 45 – 55.

[79] Oonishi, H.; Yamamoto, M.; Ishimaru, H.; Tsuji, E.; Kushitani, S.; Aono, M.; Ukon, Y. *The effect of hydroxyapatite coating on bone growth into porous titanium alloy implants*. The Journal of Bone and Joint Surgery. British Volume 1989; **71B**: 213 – 216.

[80] Deligianni, D.D.; Katsala, N.D.; Koutsoukos, P.G.; Missirlis, Y.F. *Effect of surface roughness of hydroxyapatite on human bone marrow cell adhesion, proliferation, di!erentiation and detachment strength*. Biomaterials 2001; **22**: 87 – 96.

[81] Webster, T.J.; Ergun, C.; Doremus, R.H.; Siegel, R.W.; Bizios, R. *Enhanced functions of osteoblasts on nanophase ceramics*. Biomaterials 2000; **21**:1803 – 1810.

[82] Bose, S.; Dasgupta, S.; Tarafder, S.; Bandyopadhyay, A. *Microwaveprocessed nanocrystalline hydroxyapatite: Simultaneous enhancement of mechanical and biological properties*. Acta Biomaterialia 2010; **6**: 3782 – 3790.

[83] Balasundaram, G.; Storey, D.M.; Webster, T.J. *Molecular plasma deposition: biologically inspired nanohydroxyapatite coatings on anodized nanotubular titanium for improving osteoblast density*. International Journal of Nanomedicine 2015; **10**: 527 – 535.

[84] Roy, M.; Bandyopadhyay ,A.; Bose, S. *Induction plasma sprayed Sr and Mg doped nano hydroxyapatite coatings on Ti for bone implant*. Journal of biomedical materials research B: Applied Biomaterials 2011; **99B**(2): 258 – 265.

[85] Rahaman, M.N. *Sintering of ceramics*. Boca Raton: CRC Press; 2008.

[86] Tolouei, R.; Ramesh, S.; Tan, C.Y.; Amiriyan, M.; Teng, W.D. *Sintering effects on the densification of nanocrystalline hydroxyapatite*. International Journal of Automotive and Mechanical Engineering 2011; **3**: 249 – 255.

[87] Cho, J.S.; Rhee, S.-H. *The densification mechanism of hydroxyapatite particles during spray pyrolysis with variable carrier gas rates of flow*. Journal of Biomedical Materials Research Part B Applied Biomaterials 2012; **100**(2): 493 – 500.

[88] Safronova, T.V.; Putlyaev, V.I.; Shekhirev, M.A.; Tretyakov, Y.D.; Kuznetsov, A.V.; Belyakov, A.V. *Densification additives for hydroxyapatite ceramics*. Journal of the European Ceramic Society 2009; **29**: 1925 – 1932.

[89] Sōmiya, S.; Aldinger, F.; Claussen, N.; Spriggs, R.M.; Uchino, K.; Koumoto, K.; Kaneno, M. *Handbook of Advanced Ceramics*. In: Sintering of Ceramics by De Jonghe, L.C. & Rahaman, M.N. Publisher Elsevier, pp.187 – 264.

[90] Maca, K. *Microstructure evolution during pressureless sintering of bulk oxide ceramics*. Processing and Application of Ceramics 2009; **3**(1-2): 13 – 17.

[91] Sofronia, A.M.; Baies, R.; Anghel, E.M.; Marinescu, C.A.; Tanasescu, S. *Thermal and structural characterization of synthetic and natural nanocrystalline hydroxyapatite*. Materials Science and Engineering: C 2014; **43**: 153 – 163.

[92] Ashok, M.; Meenakshi Sundaram, N.; Narayana Kalkura, S. *Crystallization of hydroxyapatite at physiological temperature*. Materials Letters 2003; **57**: 2066 –2070.

[93] Monmaturapoj, N.; Yatongchai, C. *Effect of sintering on microstructure and properties of hydroxyapatite produced by different synthesizing methods*. Journal of Metals, Materials and Minerals 2010; **20**(2): 53 – 61.

[94] Wang, P.E. & Chaki, T.K. *Sintering behaviour and mechanical properties of hydroxyapatite and dicalcium phosphate*. Journal of Materials Science Materials in Medicine 1993; **4**: 150 – 158.

[95] Rootare, H.M. & Craig, R.G. *Characterization of hydroxyapatite powders and compacts at room temperature and after sintering at 1200 °C*. Journal of Oral Rehabilitation 1978; **5**: 293 – 307.

[96] Lafon, J.P.; Championa, E.; Bernache-Assollant; D. *Processing of AB-type carbonated hydroxyapatite $Ca_{10-x}(PO_4)_{6-x}(CO_3)_x(OH)_{2-x-2y}(CO3)_y$ ceramics with controlled composition*. Journal of the European Ceramic Society 2008; 28: 139 – 147.

[97] Heimann, R.B. *Plasma Spray Coating: Principles and Applications*. Ed. Wiley EU, 2008.

[98] Ružić, J.; Vilotijević, M.; Božić, D.; Raić, K. *Understanding plasma spraying process and characteristics of dc-arc plasma gun (PJ-100)*. Metallurgical and Materials Engineering 2012; **18**(4): 273 – 282.

[99] Fauchais, P.L.; Heberlein, J.V.R.; Boulos, M. (2014). Thermal Spray Fundamentals From Powder to Part. Springer

[100] Flame Spary Technologies. Plasma Spray. *Consultation date: 27/04/2017*.

https://www.fst.nl/systems/aps-plasma-thermal-spray-coating-system/

[101] Liu, D.-M.; Yang, Q.; Troczynski, T. *Sol–gel hydroxyapatite coatings on stainless steel substrates*. Biomaterials 2002; **23**: 691 – 698.

[102] Jillavenkatesa, A. & Condrate SR, R.A. *Sol–gel processing of hydroxyapatite*. Journal of Materials Science 1998; **33**: 4111 – 4119.

[103] Liu, D.-M.; Troczynski, T, Tseng, W.J. *Water-based sol–gel synthesis of hydroxyapatite: process development*. Biomaterials 2001; **22**: 1721 – 1730.

[104] Walsh, F.C.; & C. Ponce de Leon, C. *A review of the electrodeposition of metal matrix composite coatings by inclusion of particles in a metal layer: an established and diversifying technology*. The International Journal of Surface Engineering and Coatings 2014; **92**(2): 83 – 98.

[105] Zhitomirsky, I. *Electrophoretic and electrolytic deposition of ceramic coatings on carbon fibers*. Journal of the European Ceramic Society 1998; **18**: 849 – 856.

[106] Manso, M.; Jiménez, C.; Morant, C.; Herrero, P.; Martínez-Duart, J.M. *Electrodeposition of hydroxyapatite coatings in basic conditions*. Biomaterials 2000; **21**: 1755 – 1761.

[107] Zhitomirsky, I. *Ceramic Films Using Cathodic Electrodeposition*. JOM-e 2000; **52**(1). Available from:

http://www.tms.org/pubs/journals/JOM/0001/Zhitomirsky/Zhitomirsky-0001.html

[108] Zhang, Y.-Y.; Tao, J.; Pang, Y.-C.; Wang, W.; Wang, T. *Electrochemical deposition of hydroxyapatite coatings on titanium*. Transactions of Nonferrous Metals Society of China 2016; **6**: 633 – 637.

[109] Lobo, A.O.; Marciano, F.R.; Regiani, I.; Matsushima, J.T.; Ramos, S.C.; Corat, E.J. *Influence of temperature and time for direct hydroxyapatite electrodeposition on superhydrophilic vertically aligned carbon nanotube films*. Journal of Nanomedicine & Nanotechnology 2011; **6:227**.

[110] Narayanan, R.; Kim, S.-Y.; Kwon, T.-T.; Kim, K.-H. *Nanocrystalline hydroxyapatite coatings from ultrasonated electrolyte: Preparation, characterization, and osteoblast responses*. Journal of Biomedical Materials Research Part A 2008; 87A(415): 1053 – 1060.

[111] Mediaswanti, K.; Wen, C.; Ivanova, E.P.; Berndt, C.C.; Wang, J. (2013). *Sputtered hydroxyapatite nanocoatings on novel titanium alloys for biomedical applications*. InTech, DOI: 10.5772/54263. Available from:

https://www.intechopen.com/books/titanium-alloys-advances-in-properties-control/sputtered-hydroxyapatite-nanocoatings-on-novel-titanium-alloys-for-biomedical-applications.

[112] Ong, J.L.; Harris, L.A.; Lucas, L.C.; Lacefield, W.R.; Rigney, D. *X-ray photoelectron spectroscopycharacteri zation of ion beam sputter deposited calcium phosphate coatings*. Journal of the American Ceramic Society 1991; **74**: 2301 – 2304.

[113] León, B. & l Jansen, J.A. *Thin Calcium Phosphate Coatings for Medical Implants*. Springer 2009

[114] Hulshoff, J.E.G.; Van Dijk, K.; de Ruijter, J.E.; Rietveld, F.J.R.; Ginsel, L.A.; Jansen, J.A. *Interfacial phenomena: an in vitro studyof the effect of calcium phosphate (Ca-P) ceramic on bone formation*. Journal of Biomedical Materials Research Part A 1998; **40**: 464 – 474.

[115] Surmenev, R.A. *A review of plasma-assisted methods for calcium phosphate-based coatings fabrication*. Surface & Coatings Technology 2012; **206**: 2035 – 2056.

[116] Kelly P. J. & Arnell R. D. *Magnetron sputtering: a review of recent developments and applications*. Vacuum 2000; **56**: 159 – 172.

[117] Ellmer, K.; Kudella, F.; Mientus, R.; Schieck R.; Fiechter, S. *Influence of discharge parameters on the layer properties of reactive magnetron sputtered ZnO:A1 films*. Thin Solid Films 1994: **247**: 15 – 23.

[118] Samuelson, M. (2011). *High power impulse magnetron sputtering under industrial conditions*. Licentiate Thesis. Linköping, Sweden. Linköping University, Plasma & Coatings Physics Division.

[119] Abdul Azis, S.A.; Kennedy, J.; Murmu, P.P.; Fang, F.; Cao, P. *Structural and compositional characterization of ion beam sputtered hydroxyapatite thin films on Ti-6Al-4V*. Asian Journal of Applied Sciences 2014; **7**(8): 745 – 752.

[120] Ion Beam Sputtering: Practical Applications to Electron Microscopy. *Consultation date: 27/08/2017*.

   http://www.southbaytech.com/

[121] Ong, J.L.; Lucas, L.C.; Lacefield, W.R.; Rigney, E.D. *Structure, solubility and bond strength of thin calcium phosphate coatings produced by ion beam sputter deposition*. Biomaterials 1992; **13**(4): 249 – 254.

[122] Ong, J.L. & Lucas, L.C. *Post-deposition heat treatments for ion beam sputter deposited calcium phosphate coatings*. Biomaterials 1994; **15**(5): 337 – 341.

[123] Johnson, S.; Haluska, M.; Narayan, R.J.; Snyder, R.L. *In situ annealing of hydroxyapatite thin films*. Materials Science and Engineering C 2006; **26**: 1312 – 1316.

[124] Rydén, L.; Omar, O.; Johansson, A.; Jimbo, R.; Palmquist, A.; Thomsen, P. *Inflammatory cell response to ultra-thin amorphous and crystalline hydroxyapatite surfaces*. Journal of Materials Science: Materials in Medicine 2017; 28:9.

[125] Ong, J.L. & Lucas, L.C. *Post-deposition heat treatment for ion beam sputter deposited calcium phosphate coatings*. Biomaterials 1994; **15**: 337 – 341.

[126] Van Dijk, K.; Schaeken, H.G.; Wolke, J.G.C.; Jansen, J.A. *Influence of annealing temperature on RF magnetron sputtered calcium phosphate coatings*. Biomaterials 1996; **17**: 405 – 410.

[127] Ciobanu, C.S.; Andronescu, E.; Stoicu, A.; Florea, O.; Le Coustumer, P.; Galaup, S.; Djouadi, A.; Mevellec, J.Y.; Musa, I.; Massuyeaue, F.; prodan, A.M.; Lafdih, K.; Trusca, R.; Pasuk, I.; Predoi, D. *Influence of annealing treatment of nano-hydroxyapatite bioceramics on the vibrational properties*. Digest Journal of Nanomaterials and Biostructures 2011; **6**(2): 609 – 624.

[128] Mello, A.; Hong, Z.; Rossi, A.M.; Luan, L.; Farina, M.; Querido, W.; Eon, J.; Terra, J.; Balasundaram, G.; Webster, T.; Feinerman, A.; Ellis, D.E.; Ketterson, J.B.; Ferreira, C.L. *Osteoblast proliferation on hydroxyapatite thin coatings produced by right angle magnetron sputtering*. Biomedical Materials 2007; **2**: 67 – 77.

[129] Dinu, M.; Kiss, A.E.; Parau, A.C.; Braic, V.; Vitelaru, C.; Braic, M.; Pana, I.; Balaceanu, M.; Vladescu, A. *Influence of thermal treatment on the roughness, corrosion resistance and*

wettability of hydroxyapatite films deposited by RF magnetron sputtering. Key Engineering Materials 2014; **587**: 297 – 302.

[130] Langford, J.I. & Wilson, A.J.C. *Seherrer after Sixty Years: A Survey and Some New Results in the Determination of Crystallite Size*. Journal of Applied Crystallography 1978; **11**: 102 – 113.

[131] Nasiri-Tabrizi, B. & Abbas Fahami, A. *Structural characterization of nanocrystalline $Ni_{(50-X)}Ti_{50}Cu_X$ (X = 5, 9 wt%) alloys produced by mechanical alloying*. Advances in Nanoparticles 2013; **2**: 71 – 77.

[132] Ilinsky, A.G.; Maslov, V.V.; Nozenko, V.K.; Brovko, A.P. *On determination of volume fraction of crystalline phase in partially crystallized amorphous and nanocrystalline materials*. Journal of Materials Science 2000; **35**: 4495 – 4500.

[133] Landi, E.; Tampieri, A., Celotti, G.; Sprio, S. *Densification behaviour and mechanisms of synthetic hydroxyapatites*. Journal of the European Ceramic Society 2000; **20**: 2377 – 2387.

[134] International Standar ISO 14577-1. *Metallic materials — Instrumented indentation test for hardness and materials parameters — Part 1: Test method*. 1st Edition 2002.

[135] Wei, Q.-P.; Zhang, X.-W.; Liu, D.-Y.; Li, J.; Zhou, K.-C.; Dou Zhang, D.; Yu, Z.-M. *Effects of sputtering pressure on nanostructure and nanomechanical properties of AlN films prepared by RF reactive sputtering*. Transactions of Nonferrous Metals Society of China 2014; **24**(9); 2845 – 2855.

[136] Oliver, C. & Pharr, M. *An improved technique for determining hardness and elastic modulus using load and displacement sensing indentation experiments*. Journal of Materials Research 1992; **7**(11): 1564 – 1583.

[137] Jung, S. *Oberflächenbeurteilung -Rauheitsmessung-* Rauheitsmessung Theorie und Praxis, Raimund Volk. Spezialisierungsfachversuch und Hauptfachversuch Universität Stuttgart, 2005. *Consultation date: 10/09/2017.*
  http://www.ima.uni-stuttgart.de/

[138] International Standar DIN EN ISO 4287:2010-07. *Geometrical Product Specifications (GPS) - Surface texture: Profile method - Terms, definitions and surface texture parameters*.

[139] Erasmus, E.P.; Johnson, O.T.; Sigalas, I.; Massera, J. *Effects of sintering temperature on crystallization and fabrication of porous bioactive glass scaffolds for bone regeneration*. Scientific Reports 2017; **7**: 6046.

[140] Davis, J.R. *Handbook of Thermal Spray Technology*. ASM Thermal Spray Society 2004.

[141] Wang, H.; Lee, J.-K.; Moursi, A.; Lannutti, J.J. *Ca/P ratio effects on the degradation of hydroxyapatite in vitro*. Journal of Biomedical Materials Research Part A 2003; **67**(2): 599 – 608.

[142] Dorozhkin, S.V. *Calcium orthophosphates in nature, biology and medicine*. Materials 2009; **2**, 399 – 498.

[143] LeGeros, R.Z.; Kijkowska, E.; Bautista, C.; LeGero, J.P. *Synergistic effects of magnesium and carbonate on properties of biological and synthetic apatites*. Connective lissue Research 1995; 33(1-3): 203 – 209 [525 – 531].

[144] Pattanayak, D.K.; Dash, R.; Prasad, R.C.; Rao, B.T.; Rama Mohan, T.R. *Synthesis and sintered properties evaluation of calcium phosphate ceramics*. Materials Science and Engineering: C 2007; **27**(4): 684 – 690.

[145] Azevedo, A.G. de S.; Strecker, K.; Gorgulho, H.F. *Efeito da temperatura em processos de sinterização de pós de hidroxiapatita*. Cerâmica 2015; **61**: 52 – 59.

[146] Lazić, S.; Zec, S.; Miljević, N., Milonjić, S. *The effect of temperature on the properties of hydroxyapatite precipited from calcium hydroxide and phosphoric acid*. Thermochimica acta 2001; **374**: 13 – 22.

[147] P. Kofstad. *High-temperature oxidation of titanium*. Journal ofthe Less-Common Metals 1967; **12**: 449 – 464.

[148] Berezhnaya, A.Yu.; Mittova, V.O.; Kukueva, E.V.; Mittova, I.Ya. *Effect of High_Temperature Annealing on Solid_State Reactions in Hydroxyapatite/TiO$_2$ Films on Titanium Substrates*. Inorganic Materials 2010; **46**(9): 971 – 977.

[149] Ooi; C.Y.; Hamdi, M.; Ramesh, S. *Properties of hydroxyapatite produced by annealing of bovine bone*. Ceramics International 2007; **33**: 1171 – 1177.

[150] Saber-Samandari, S. & Gross, K.A. *The use of thermal printing to control the properties of calcium phosphate deposits*. Biomaterials 2010; **31**: 6386 – 6393.

[151] Behera, A.; Aich, S.; Behera, A.; Ashutosh Sahu, A. *Processing and characterization of magnetron sputtered Ni/Ti thin film and their annealing behaviour to induce shape memory effect*. Materials Today: Proceedings 2015, **2**: 1183 – 1192.

[152] Surmeneva, M.A.; Surmenev, R.A.; Pichugin, V.F.; Koval, N.N.; Teresov, A.D.; Ivanova, A.A.; Grubova, I.Yu.; Ignatov, V.P.; Primak, O.; Epple, M. *Adhesion properties of a silicon-containing calcium phosphate coating deposited by RF magnetron sputtering on a heated substrate*. Journal of surface investigation. X-ray, synchrotron and neutron techniques 2013; **7**(5): 944 – 951.

[153] Sarin, V.K. (2014). *Comprehensive hard materials*. Volume 3: Super Hard Materials. In: Theory of superhard materials by Oganov, A.R.; Lyakhov, O.; Zhu, Q. Publisher Elsevier, pp. 59 – 80.

List of Symbols

Shortcut words

et al.	and other
e.g.	for example
g	grams

Calcium phosphate family

CPC	calcium phosphate based ceramics
HAp	hydroxyapatite
MCPM	monocalcium phosphate monohydrate
MCPA	monocalcium phosphate anhydrous
DCPD	dicalcium phosphate dihydrate
DCPA	dicalcium phosphate anhydrous
OCP	octacalcium phosphate
α-TCP	α-tricalcium phosphate
β-TCP	β-tricalcium phosphate
ACP	amorphous calcium phosphates
CDHA	calcium-deficient hydroxyapatite
FAp	fluorapatite
OAp	oxyapatite
TTCP	tetracalcium phosphate

Materials, analyze equipment and parameters

PVA	polyvinyl alcohol
PEG	polyethylene glycol
ELD	electrolytic deposition
HR	heating regime
EPD	electrophoretic deposition
TGA	thermo-gravimetric analysis
FWHM	full width at half maximum
EHT	acceleration voltage
ISO	International Organization for Standardization
HM	Martens hardness
ICDD	International Centre for Diffraction Data
PDF	Powder Diffraction File

RF	radio frequency
IBS	ion beam sputtering
XRD	X-ray diffractometry
FIB	Focus ion beam
SEM	scanning electron microscopy
EDX	energy dispersive X-ray spectroscopy

Symbols in formula

G	total Gibbs free energy
A_{sg}	solid–gas surface area
γ_{sg}	solid–gas surface energy
A_{ss}	solid–solid surface area
γ_{ss}	solid–solid surface energy
τ	crystal size
K	Scherrer constant
λ	X-ray wavelength
β_{hkl}	full width at half maximum
X_C	crystallinity
ρ	relative density
P	porosity
L_0	original length
L	length at a given time or temperature

List of Figures

List of Tables